

# Ultrafast Acoustoelectric Effects in Semiconductor Devices

Sarah Louise Heywood, MPhys

Thesis submitted to the University of Nottingham  
for the degree of Doctor of Philosophy

July 2016

# Abstract

This thesis discusses experiments that have been performed to investigate ultrafast acoustoelectric effects in semiconductor devices. Current commonly employed techniques to generate ultrafast acoustic pulses and detect them with spectral resolution require a powerful pulsed laser system that is bulky, expensive and complicated. If the acoustic pulses could instead be generated and detected by electrical methods, picosecond acoustic techniques could become more readily available as a tool for other users.

This thesis focusses on the electrical detection of acoustic pulses with spectral resolution. In many of the key experiments described in this thesis a picosecond strain pulse was generated optically on the opposite face of the sample to the semiconductor device of interest. The strain was generated either in a thin Al film thermally deposited on the sample surface, or directly in the GaAs substrate. Acoustic phonons generated by this method propagated across the substrate to the device. Transient voltages across the semiconductor device caused by the incident phonons were detected using a high frequency real-time oscilloscope.

The first evidence of heterodyne mixing of coherent acoustic phonons with microwaves was obtained, for frequencies up to about 100 GHz. First, it was confirmed that Schottky diodes can produce a fast transient voltage in response to an incident acoustic wavepacket. The detection process occurs at the semiconductor-metal interface, and is due to the deformation potential. Bow-tie antenna fabricated directly onto the GaAs substrate proved to be ineffective at coupling microwaves from free space to the Schottky diode. A waveguide-coupled beam-lead Schottky diode provided by e2v had a sufficient response to the incident microwaves to proceed with the mixing experiments.

The microwave local oscillator signal was mixed with a tunable narrow frequency band acoustic signal that was produced using a Fabry-Perot etalon external to the laser cavity. The intermediate frequency components were in the range of 1-12 GHz, which could be detected on the oscilloscope. Mixing was performed using both the fundamental frequency acoustic wave and the second harmonic generated in the sample.

Semiconductor superlattices were also investigated as electrical detectors for ultrafast acoustic pulses. In this case, the transient voltage measured across the device contained an unexpected contribution in the form of a peak with a width of approximately 2 ns. This signal is too slow to be caused by a strain pulse and too fast for a heat pulse. It is proposed that this peak is caused by long-lived phonon modes from the centre of the mini-Brillouin zone being confined in the superlattice due to Bragg reflections.

The peak caused by confined phonons and the two peaks caused by heat pulses also present in the detected signal were investigated for a range of experimental conditions. This allowed comparisons to be made to previous works. A similar superlattice structure had a very different response to the incident acoustic wavepacket. The polarity of the transient voltage detected was inverted and there was no evidence of an electronic response to the confined phonon modes, which would have been present in both samples. It is proposed that the barriers of the NU1727 superlattice sample are thicker than expected, and this strongly affects the electron transport through the structure.

This thesis shows that semiconductor devices can be suitable for the electrical detection of ultrafast strain pulses. For this technique to reach its full potential, it is also necessary to be able to generate these strain pulses electrically. A step recovery diode has been considered for this purpose as part of the suggested future work.

# Acknowledgements

First and foremost I must thank my supervisor Tony Kent for his guidance throughout the whole process, and Andrey Akimov for vital assistance in the lab. These thanks extend to Richard Campion and Mohamed Henini for growing most of the structures used in these experiments.

I am grateful for all the help I received from the technical staff in the physics department. Especially the help from Jas Chauhan and Dave Taylor in the clean room, and Chris Pallender and Dave Holt for the supply of liquid helium, often at short notice.

I must also thank the staff at e2v for all of their support, but especially Nigel Priestley and Mike Carr. From the initial loan of equipment for use in experiments and useful discussions on microwaves, to giving me a job before the end of my PhD, and finally for letting me take time out from that job to finish this thesis!

I would like to thank all of the THz Acoustics group members, both past and present. Particularly Ryan Beardsley and Eric Young for lots of help in the early days and Caroline Poyser for being there all the way through.

I would also like to thank all of my friends from both the physics department and elsewhere, for making my time in Nottingham more enjoyable and for providing me with distractions, cookies, sympathetic ears, dinners and evenings with bunny rabbits. Special thanks go to Elizabeth Pain, Richard Cousins, Sara-Louise Helm and William Kummer.

And last, but certainly not least, I couldn't have done this without my family. Especially my little brother Peter and my parents, who have always supported me in everything I have done.

Some aspects of the work presented in this thesis were performed by a number of different people, either as a collaborative effort or because this thesis builds upon previous work performed at the University of Nottingham. The contributions to this work made by different people will now be outlined below.

Mohammed Henini grew the NU1727 and NU1778 wafers by molecular beam epitaxy, and Richard Campion grew the Mn659, Mn744 and Mn775 wafers. These were all grown at the University of Nottingham.

The beam-lead Schottky diode was designed, produced, and mounted in the W-band waveguide circuit by employees of the e2v Microwave Technology Centre in Lincoln. They determined the basic parameters of the device, such as the capacitance, resistance and ideality factor.

Ryan Beardsley had previously done work on some of the structures and devices as part of his earlier research within the THz Acoustics group at the University of Nottingham. He designed the Mn659 wafer structure, the mask and the processing steps for those Schottky diodes and he made the NU1727 samples used in this thesis. He also wrote the computer program used to calculate the phonon dispersion curves.

Tony Kent, my PhD supervisor, and Boris Glavin, a collaborator, did some of the maths relating to the Schottky diode mixing experiments, and this is highlighted at the appropriate point in the text.

All of the experiments described in the experimental chapters and the further work were performed by myself, Sarah Heywood. I also analysed the data unless stated in the text. I spent a large proportion of my time in the university clean room fabricating devices and preparing samples for the experiments. I fabricated the Mn659 Schottky diodes, following Ryan Beardsley's advice. I designed the mask, wafer structure and processing steps for the Mn744 Schottky diodes. I deposited, and then removed, numerous Al films on the NU1727 samples previously made by Ryan Beardsley. I made the NU1778 samples by using the growth sheet provided by Mohammed Henini to plan the processing steps required and using an existing mask set. I designed the sample structure for the Mn775 wafer and the processing steps using an existing mask set, and then made the samples.

# Contents

<b>Abstract</b>	<b>i</b>
<b>Acknowledgements</b>	<b>iii</b>
<b>Contents</b>	<b>v</b>
<b>List of Figures</b>	<b>ix</b>
<b>List of Tables</b>	<b>xiii</b>
<b>List of Abbreviations</b>	<b>xiv</b>
<b>List of Symbols</b>	<b>xvi</b>
<b>1 Introduction</b>	<b>1</b>
1.1 Thesis outline . . . . .	5
<b>2 Background</b>	<b>8</b>
2.1 Generation, propagation and detection of acoustic waves . . .	9
2.1.1 Generation of strain pulses . . . . .	9
2.1.2 Generation of strain in superlattices . . . . .	12
2.1.3 Generation of heat pulses . . . . .	13
2.1.4 Propagation . . . . .	14
2.1.5 Detection . . . . .	18
2.2 Electron-phonon coupling mechanisms . . . . .	20
2.2.1 Deformation potential coupling . . . . .	21
2.2.2 The piezoelectric effect . . . . .	21
2.3 Preliminary work on high frequency acoustoelectric techniques . . . . .	22
2.3.1 Strain induced modulation of the photocurrent in quantum well devices . . . . .	23

2.3.2	Electrical detection of strain pulses using a Schottky diode . . . . .	26
2.3.3	Strain induced modulation of electron transport in resonant tunnelling diodes . . . . .	29
2.4	Conclusion . . . . .	31
<b>3</b>	<b>Experimental techniques</b>	<b>33</b>
3.1	Device fabrication . . . . .	33
3.1.1	Cleaving and cleaning samples . . . . .	34
3.1.2	Photolithography and etching . . . . .	34
3.1.3	Deposition of metals and insulating layers . . . . .	35
3.1.4	Wafer polishing . . . . .	36
3.1.5	Sample packaging . . . . .	37
3.2	Determining I-V characteristics of devices . . . . .	37
3.3	Generating acoustic signals optically . . . . .	38
3.3.1	Broad spectrum acoustic pulses . . . . .	38
3.3.2	Narrow spectrum acoustic pulses . . . . .	39
3.4	Fast electrical measurements . . . . .	46
3.5	Measuring the microwave response of devices . . . . .	46
<b>4</b>	<b>Heterodyne detection of optically-generated coherent acoustic waves using a Schottky diode</b>	<b>50</b>
4.1	Heterodyne mixing . . . . .	51
4.2	Schottky diodes . . . . .	53
4.2.1	General background . . . . .	53
4.2.2	Schottky diodes used as microwave mixers . . . . .	57
4.3	Preliminary work on Schottky diodes detecting acoustic and microwave signals . . . . .	58
4.3.1	Device structures . . . . .	58
4.3.2	Device characterisation . . . . .	62
4.3.3	Detecting acoustic signals . . . . .	64
4.3.4	Microwave response of devices . . . . .	68
4.4	Beam-lead Schottky diode . . . . .	70
4.4.1	Device structure and characterisation . . . . .	70
4.4.2	Detecting acoustic signals using a beam-lead Schottky diode . . . . .	72
4.4.3	Heterodyne mixing of optically-generated acoustic waves using a beam-lead Schottky diode . . . . .	82

4.4.4	Further analysis of mixing results . . . . .	87
4.5	Conclusion . . . . .	97
<b>5</b>	<b>Electrical detection of confinement of acoustic phonons in a superlattice</b>	<b>98</b>
5.1	Background of superlattices . . . . .	99
5.1.1	Electronic properties of superlattices . . . . .	100
5.1.2	Acoustic properties of superlattices . . . . .	103
5.1.3	Applications . . . . .	103
5.2	Device structures . . . . .	105
5.3	Electrical measurements of acoustic signals in 50 period superlattice samples . . . . .	107
5.3.1	Device characterisation . . . . .	107
5.3.2	Acoustic signal with a thin Al film transducer . . . . .	112
5.3.3	Comparison with other film thicknesses . . . . .	117
5.3.4	Position dependence . . . . .	121
5.3.5	Comparison with a superlattice with only 10 periods . . . . .	125
5.4	Properties of the peak caused by confined coherent modes . . . . .	125
5.4.1	Bias dependence . . . . .	126
5.4.2	Laser power dependence . . . . .	130
5.4.3	Comparison to previous work . . . . .	131
5.5	Measuring the transient voltage across the SL caused by incident heat pulses . . . . .	138
5.5.1	Bias dependence . . . . .	140
5.5.2	Comparison to previous work . . . . .	144
5.5.3	Laser power dependence . . . . .	146
5.6	Conclusion . . . . .	148
<b>6</b>	<b>Conclusions and future work</b>	<b>151</b>
6.1	Conclusions . . . . .	151
6.2	Future work . . . . .	154
6.2.1	Mixing acoustic phonons with microwaves . . . . .	155
6.2.2	Electrical detection of ultrafast acoustic pulses using a superlattice . . . . .	156
6.2.3	Electrical generation of ultrafast strain pulses . . . . .	157
6.3	Summary . . . . .	162
	<b>Bibliography</b>	<b>163</b>

<b>A</b>	<b>Processing instructions</b>	<b>176</b>
A.1	Common processing steps . . . . .	176
A.2	Mn659 Schottky diodes . . . . .	180
A.3	Mn744 Schottky diodes . . . . .	181
A.4	NU1778 superlattice devices . . . . .	183
A.5	Mn775 step recovery diodes . . . . .	184

# List of Figures

2.1	Illustration of the optical generation of a bipolar strain pulse	10
2.2	Phonon dispersion in the $\langle 100 \rangle$ direction in GaAs at room temperature . . . . .	17
2.3	Illustration of the superconducting transition of a typical bolometer . . . . .	20
2.4	Schematic diagram of the experimental set-up for Moss' photocurrent experiment . . . . .	24
2.5	Diagrammatic representation of how strain modulates the photocurrent in a quantum well . . . . .	25
2.6	Schematic diagram of the device and the strain pulses in Moss' Schottky diode experiment . . . . .	27
2.7	Illustration of Moss' results of the temporal response of the Schottky diode to an ultrafast strain pulse . . . . .	28
2.8	Schematic band diagram of a double-barrier resonant tunnelling diode . . . . .	30
3.1	Set-up for I-V characteristic measurements . . . . .	38
3.2	Illustration comparing a broad frequency spectrum with a quasi-monochromatic spectrum . . . . .	39
3.3	Illustration of the operation of the Fabry-Perot etalon . . . . .	41
3.4	Set-up for pump-probe measurements to test the Fabry-Perot etalon . . . . .	43
3.5	Optical pump-probe results of the Fabry-Perot cavity function at $f_0 = 40$ GHz . . . . .	45
3.6	Set-up for fast electrical measurements . . . . .	47
3.7	Experimental set-up to use a lock-in amplifier to measure the microwave response of a device . . . . .	48
4.1	Energy band diagrams of an $n$ -type Schottky diode . . . . .	54

4.2	Energy band diagrams of an $n$ -type Schottky diode under different biasing conditions . . . . .	55
4.3	Schematic diagram of a Schottky diode fabricated from the Mn659 wafer . . . . .	59
4.4	Microscope image of a Schottky diode fabricated from the Mn659 wafer . . . . .	60
4.5	Schematic diagram of a Schottky diode fabricated from the Mn744 wafer . . . . .	61
4.6	Microscope image of a Schottky diode fabricated from the Mn744 wafer . . . . .	61
4.7	I-V characteristics of Schottky diodes fabricated from wafers Mn659 and Mn744 . . . . .	63
4.8	Acoustic signal detected by a Schottky diode fabricated from the Mn744 wafer . . . . .	64
4.9	Bias dependence of the temporal response of the Mn744 Schottky diode . . . . .	66
4.10	Layers in the Mn744 structure that lead to reflections of the acoustic wavepacket . . . . .	67
4.11	Schematic diagram of the beam-lead Schottky diode provided by e2v . . . . .	71
4.12	Images of the beam-lead Schottky diode and the microwave circuit it was mounted in, provided by e2v . . . . .	72
4.13	I-V characteristics of the beam-lead Schottky diode with and without the effect of the microwave local oscillator . . . . .	73
4.14	Acoustic signal detected by the beam-lead Schottky diode . . . . .	75
4.15	Zoomed-in view of acoustic signal detected by the beam-lead Schottky diode . . . . .	76
4.16	Comparison of the acoustic signal detected by the beam-lead Schottky diode when exciting the substrate with 800 nm and 400 nm wavelength light . . . . .	78
4.17	Bias dependence of the acoustic signal detected by the beam-lead Schottky diode . . . . .	80
4.18	Results for heterodyne mixing of a microwave local oscillator signal with the 2nd harmonic acoustic signal using a beam-lead Schottky diode . . . . .	84

4.19	Results for heterodyne mixing of a microwave local oscillator signal with the fundamental frequency acoustic signal using a beam-lead Schottky diode . . . . .	86
4.20	Theoretical calculation of the IF spectrum for mixing of the microwave LO with the 2nd harmonic acoustic signal . . . . .	92
4.21	Simulation results for frequency components present in the modulated acoustic signal for two different values of the cavity spacing, $d$ . . . . .	94
4.22	Laser pump power dependence of peak IF power . . . . .	96
5.1	Schematic diagram of a superlattice structure . . . . .	100
5.2	Different electron transport regimes in a semiconductor superlattice . . . . .	101
5.3	Folded acoustic phonon dispersion for a semiconductor superlattice . . . . .	104
5.4	Schematic diagram of superlattice devices fabricated from the NU1727 and NU1778 wafers . . . . .	106
5.5	Microscope image of superlattice devices fabricated from the NU1727 wafer . . . . .	107
5.6	I-V characteristics of the 50 period superlattice sample NU1727	109
5.7	Calculated longitudinal acoustic phonon dispersion for the NU1727 superlattice . . . . .	111
5.8	Acoustic signal detected by the 50 period superlattice sample NU1727 . . . . .	113
5.9	Acoustic signal detected by the 50 period superlattice sample NU1727 for a range of applied bias . . . . .	114
5.10	Electrical circuit connecting the superlattice device to the oscilloscope via the bias tee . . . . .	116
5.11	Equivalent circuits for the ideal electrical set-up for the DC and high frequency cases . . . . .	116
5.12	Effect of Al film transducer thickness on the acoustic signal detected by the 50 period superlattice sample NU1727 with -0.2 V bias applied . . . . .	118
5.13	Effect of Al film transducer thickness on the acoustic signal detected by the 50 period superlattice sample NU1727 with 0.5 V bias applied . . . . .	119
5.14	Schematic diagram of the position dependence experiment . . . . .	122

5.15	Position dependence of the longitudinal acoustic peak in the NU1727 signal for the thin Al film . . . . .	123
5.16	Bias dependence of the 2 ns part of the NU1727 signal caused by confined coherent phonons using thin film number 2 . . .	127
5.17	Laser power dependence of the 2 ns part of the NU1727 signal using thin film number 2 . . . . .	130
5.18	Schematic energy diagrams of type I and type II superlattice structures . . . . .	134
5.19	Illustration of one-phonon assisted tunnelling processes between two quantum wells . . . . .	137
5.20	Comparing the superlattice response to an incident acoustic wavepacket generated in two different 30 nm Al transducer films . . . . .	139
5.21	Bias dependence of the LA heat pulse in the NU1727 signal .	141
5.22	Bias dependence of the TA heat pulse in the NU1727 signal	142
5.23	Calculated dispersion for transverse acoustic phonons in the NU1727 superlattice . . . . .	143
5.24	Laser power dependence of both the LA and TA heat pulses in the NU1727 signal . . . . .	147
6.1	Schematic diagram of a step recovery diode fabricated from the Mn775 wafer. . . . .	158
6.2	I-V characteristics of a 200 $\mu\text{m}$ diameter step recovery diode fabricated from wafer Mn775 . . . . .	159
6.3	Test for pulse sharpening using a 200 $\mu\text{m}$ diameter step recovery diode fabricated from wafer Mn775 . . . . .	161

# List of Tables

5.1	Layer parameters used to calculate the phonon dispersion for the NU1727 superlattice . . . . .	111
5.2	Results of calculations of the miniband width for different possible layer thicknesses for the NU1727 superlattice . . . .	135

# List of Abbreviations

<b>Al</b>	Aluminium
<b>AlAs</b>	Aluminium arsenide
<b>AlGaAs</b>	Aluminium gallium arsenide
<b>Ar</b>	Argon
<b>Au</b>	Gold
<b>DC</b>	Direct current
<b>DMM</b>	Digital multi-meter
<b>DVS</b>	Digital voltage source
<b>GaAs</b>	Gallium arsenide
<b>Ge</b>	Germanium
<b>H<sub>2</sub></b>	Hydrogen
<b>HCl</b>	Hydrochloric acid
<b>H<sub>2</sub>O</b>	Water
<b>H<sub>2</sub>O<sub>2</sub></b>	Hydrogen peroxide
<b>I-V</b>	Current-voltage
<b>IF</b>	Intermediate frequency
<b>In</b>	Indium
<b>LA</b>	Longitudinal acoustic
<b>LO</b>	Local oscillator
<b>Mg</b>	Magnesium

<b>MBE</b>	Molecular beam epitaxy
<b>NH<sub>3</sub></b>	Ammonia
<b>Ni</b>	Nickel
<b>QW</b>	Quantum well
<b>RF</b>	Radio frequency
<b>RTD</b>	Resonant tunnelling diode
<b>Si</b>	Silicon
<b>SASER</b>	Sound amplification due to stimulated emission of radiation
<b>SAW</b>	Surface acoustic wave
<b>SiO<sub>x</sub></b>	Silicon oxides
<b>SL</b>	Superlattice
<b>SRD</b>	Step recovery diode
<b>TA</b>	Transverse acoustic
<b>THz</b>	Terahertz
<b>Ti</b>	Titanium
<b>UV</b>	Ultraviolet
<b>1D</b>	One dimensional
<b>2D</b>	Two dimensional

# List of Symbols

$E, E_{i,i+1}$	Energy, J
$w$	Thickness, m
$\zeta$	Absorption length, m
$A$	Area, m <sup>2</sup>
$z$	Distance along the $z$ axis, m
$\Delta T$	Change in temperature, K
$r, r_{1,2}$	Reflectivity, dimensionless
$C_V$	Specific heat per unit volume, J K <sup>-1</sup> m <sup>-3</sup>
$\sigma$	Stress, Pa
$B$	Bulk modulus, Pa
$\beta$	Linear expansion coefficient, K <sup>-1</sup>
$\eta$	Strain, dimensionless
$D_L$	Linear dimensions of a laser spot, m
$\tau_l$	Time duration of a laser pulse, s
$v_s$	Speed of sound, ms <sup>-1</sup>
$D_T$	Thermal diffusivity, m <sup>2</sup> s <sup>-1</sup>
$K$	Thermal conductivity, W m <sup>-1</sup> K <sup>-1</sup>
$f$	Frequency, Hz
$h$	Planck constant, $6.626 \times 10^{-34}$ J s
$k_B$	Boltzmann constant, $1.381 \times 10^{-23}$ J K <sup>-1</sup>

$T$	Temperature, K
$a$	Lattice spacing, m
$\omega_q$	Angular frequency of a phonon with wave vector $q$ , $\text{rad s}^{-1}$
$q$	Phonon wave vector, $\text{rad m}^{-1}$
$\delta E_{edge}$	Change in the energy band edge, eV
$\Xi$	Deformation potential, eV
$I_P$	Photocurrent, A
$\hbar$	Reduced Planck constant, $1.055 \times 10^{-34}$ J s
$\omega, \omega_{1,2}$	Angular frequencies, $\text{rad s}^{-1}$
$E_0$	Exciton energy, eV
$\Delta$	Energy detuning, eV
$I_0$	Photocurrent when there is no strain present, A
$\Delta_0$	Energy detuning when there is no strain present, eV
$t$	Time, s
$t_0$	The time for an acoustic wavepacket to cross a sample, s
$W_d$	The width of the depletion region, m
$Q$	Charge, C
$E_{FE}$	Fermi energy of the emitter, eV
$V_{device}$	Voltage across a device, V
$I_{device}$	Current flowing through a device, A
$V_{DVS}$	Voltage applied by a digital voltage source, V
$V_{DMM}$	Voltage measured on a digital multi-meter, V
$R$	Resistance, $\Omega$
$d$	Fabry-Perot mirror separation, m
$f_0$	Frequency set by the Fabry-Perot etalon, Hz

$c$	Speed of light in a vacuum, $3.000 \times 10^8 \text{ ms}^{-1}$
$\tau_0$	Time interval between pulses from the Fabry-Perot etalon, s
$\lambda$	Wavelength, m
$I$	Current, A
$V, V_{1,2}$	Voltages, V
$a_{1,2}$	Constants, dimensionless
$e$	Elementary charge, $1.602 \times 10^{-19} \text{ C}$
$e\phi_m$	Work function of a metal, eV
$e\phi_s$	Work function of a semiconductor, eV
$E_{Fm}$	Fermi level of a metal, eV
$E_{Fs}$	Fermi level of a semiconductor, eV
$E_F$	Fermi level at equilibrium, eV
$E_C$	Conduction band energy, eV
$E_V$	Valence band energy, eV
$V_0$	The equilibrium contact potential in a Schottky diode, V
$e\phi_B$	Schottky barrier height, eV
$e\chi$	Electron affinity, eV
$\epsilon_r$	Relative permittivity, dimensionless
$\epsilon_0$	Permittivity of free space, $8.854 \times 10^{-12} \text{ Fm}^{-1}$
$N_D$	Donor concentration of an $n$ -doped semiconductor, $\text{cm}^{-3}$
$V_f$	Forward bias voltage, V
$V_r$	Reverse bias voltage, V
$I_S$	Reverse saturation current, A
$\alpha$	Ideality factor, dimensionless
$n$	$n$ -type dopant concentration, $\text{cm}^{-3}$

$v_{GaAs}$	The speed of sound in GaAs, $\text{ms}^{-1}$
$v_{Au}$	The speed of sound in Au, $\text{ms}^{-1}$
$f_{LO}$	The frequency of the local oscillator, Hz
$f_{IF}$	The intermediate frequency, Hz
$m, m_{1,2}$	Integers, dimensionless
$\mathcal{L}(f_{off})$	Phase noise measured at $f_{off}$ expressed as a ratio, dimensionless
$f_{off}$	Offset frequency, Hz
$f_{osc}$	Carrier frequency, Hz
$C_{osc}$	A constant linked to phase noise, dimensionless
$f_{FWHM}$	The full width at half maximum of an oscillator, Hz
$s_{zz}(t)$	Time dependent strain, dimensionless
$l_s$	Screening length, m
$v_{ac}(t)$	Time dependent voltage due to the acoustic signal, V
$\Xi_{eff}$	Effective deformation potential, eV
$V_{LO}$	Peak local oscillator voltage, V
$i(t)$	Time dependent current, A
$g(t)$	Time dependent conductivity, $\text{Sm}^{-1}$
$v_{LO}(t)$	Time dependent local oscillator voltage, V
$V_{ap}$	An applied DC bias, V
$\varphi$	Phase, rad
$s_{zz(0)}(t)$	Strain profile produced by the first optical pulse, dimensionless
$R_L$	Load resistance, $\Omega$
$S_{zz(0)}(\omega)$	Fourier transform of $s_{zz(0)}(t)$ , dimensionless
$V_{ac}(\omega)$	Strain induced voltage as a function of angular frequency, V
$G(\omega)$	Fourier transform of $g(t)$ , $\text{Sm}^{-1}$

$P$	Power spectral density, $\text{W Hz}^{-2}$
$U^{(1)}$	Voltage perturbation due to the strain pulse, V
$\tilde{U}^{(1)}$	Fourier spectrum of the voltage perturbation $U^{(1)}$ , V
$A_1, B_1$	Fourier coefficients, dimensionless
$\omega_0$	$= 2\pi f_0$ , angular frequency set by the Fabry-Perot etalon, $\text{rad s}^{-1}$
$\Delta\omega$	$= \omega - \omega_{LO}$ , $\text{rad s}^{-1}$
$\gamma$	$= \frac{\omega_0(1-r_1r_2)}{2\pi\sqrt{r_1r_2}}$ , $\text{rad s}^{-1}$
$y$	Variable denoting the $y$ axis, unspecified units
$x$	Variable denoting the $x$ axis, unspecified units
$d_{SL}$	Superlattice period, m
$L_{SL}$	Length of the superlattice, m
$\Delta_m$	Miniband width, V
$\Delta_S$	Stark splitting, eV
$\lambda_{WS}$	Wannier-Stark localisation length, m
$F$	Electric field strength, $\text{Vm}^{-1}$
$\lambda$	Wavelength, m
$\theta$	Angle of incidence measured from the normal, rad
$V_T$	Threshold voltage, V
$d_A, d_B$	Thicknesses of the two different superlattice layers, m
$v_A, v_B$	Speed of sound in the two different superlattice layers, $\text{ms}^{-1}$
$\delta$	$= \rho_A v_A / \rho_B v_B$ , ratio of acoustic impedances, dimensionless
$\rho_A, \rho_B$	Densities of the two different superlattice layers, $\text{kg m}^{-3}$
$X_L$	Inductor reactance, $\Omega$
$L$	Inductance, H
$X_C$	Capacitor reactance, $\Omega$

$C$	Capacitance, F
$i_{dev}$	Current through the device, A
$i_{scope}$	Current through the oscilloscope, A
$k$	Photon wave vector, $\text{rad m}^{-1}$
$p_{phonon}$	Phonon momentum, Ns
$p_{photon}$	Photon momentum, Ns
$\Upsilon$	Fraction of the bias dropped across a superlattice, dimensionless
$k_{SL}$	Wave vector in the superlattice, $\text{rad m}^{-1}$
$k_b$	Wave vector in the barriers, $\text{rad m}^{-1}$
$k_w$	Wave vector in the wells, $\text{rad m}^{-1}$
$d_b$	Barrier thickness, m
$d_w$	Well thickness, m
$E_{scat}$	Energy broadening due to scattering, J
$\tau_{scat}$	Scattering time, s
$v_F$	Fermi velocity, $\text{ms}^{-1}$
$\Delta I$	Change in current, A
$E_p$	Phonon energy, J
$T_e$	Electron temperature, K
$W(q)$	Transition rate, $\text{s}^{-1}$
$g_d(q)$	Phonon density of states, $\text{m}^{-2}$
$n_q^*$	$= a_1 n_q^*$ , effective phonon occupation number, dimensionless
$n_q$	Phonon occupation number, dimensionless
$W_{1,2,3,4}^{+,-}$	Rates of different transitions, $\text{s}^{-1}$
$\Delta_{\max}$	Stark splitting when tunnel current is at a maximum, eV
$T_h$	Heater temperature, K

$\rho$	Density, $\text{kg m}^{-1}$
$V_{ol}$	Volume, $\text{m}^3$
$C_m$	Specific heat capacity, $\text{J kg}^{-1}\text{K}^{-1}$
$N(f)$	The number of phonons at a given frequency, dimensionless
$p$	Acceptor concentration of a $p$ -doped semiconductor, $\text{cm}^{-3}$

# Chapter 1

## Introduction

With the introduction of optical methods of generating and detecting very short strain pulses, the field of picosecond acoustics was created. A short light pulse incident on an opaque material can be used to generate high frequency coherent phonons in semiconductors and metals [1]. Another short optical pulse can be used to detect the presence of these phonons by observing changes in the reflectivity of the surface of the sample. This technique is now commonly known as “optical pump-probe” and has become a widely used tool to study many aspects of fundamental properties of both acoustic pulses and the materials they propagate in.

Since the early work on the generation of very short strain pulses using picosecond light pulses [1], the generation of strain by this method has been studied in detail in both metals [2–5] and semiconductors [6–8]. The laser energy is absorbed by the material a short distance into the sample. The localised heating caused by the laser energy sets up a stress in the material and the relaxation of the stress launches an associated strain pulse, which can propagate away from the surface.

The detection process can either be in the same surface as the generation process, or on the opposite face of the sample after the acoustic pulse has propagated through the material and any structure present. The detection mechanism relies on both the changes to the refractive index of the material and the surface displacement caused by the strain pulse. These can be measured either by detecting changes in the reflected probe laser beam [1,3],

or by an interferometric method [9, 10].

Picosecond ultrasonics has proven to be an extremely useful experimental tool, allowing the study of numerous properties of materials. These include, but are not restricted to: determining the thickness and sound velocity of thin films [11], studies of the bonding of thin films to the substrate material [12], the attenuation [13], dispersion [14, 15] and diffraction [16] of acoustic pulses propagating through, and the formation of solitons in crystalline material [17–19].

The technique is not just limited to crystalline solid materials. Picosecond acoustic measurements have also been performed on amorphous solids [20], liquid surfaces [21], and even living cells [22]. They have also been extremely useful in the observation and study of coherent vibrations in multilayer structures formed in a variety of material systems [23–25].

Some of the more recent research has been more application driven, with picosecond acoustic techniques being used to determine the presence of interesting and potentially useful effects in nanostructures. Quantised vibrational modes in thin polymer films have been detected [26] and the frequencies of these modes change by a measurable amount when the film is loaded, suggesting that they can be used for mass sensing [27]. The shift of a semiconductor band gap due to the presence of strain has been observed in heterostructures, which suggests that strain can be used to control the electronic states in nanostructures [28]. Phonon amplification has been observed in semiconductor superlattices, which is an important step towards the fabrication of a sound equivalent to the laser [29]. This type of device is often referred to as a SASER, which stands for sound amplification due to the stimulated emission of acoustic radiation.

It is clear from the literature that picosecond acoustics can be an extremely valuable experimental tool. The main attractive features of this technique are its non-destructive nature and the phonon frequencies involved, allowing the study of fast temporal effects and small spatial measurements. It is also very useful for the investigation of vibrational modes at these frequencies. However, the current technique has limited potential outside of the laboratory due to the size and expense of the high powered laser system and the external optics required, along with the expertise

necessary to operate such a system.

It would be beneficial to be able to generate and detect picosecond acoustic pulses by an alternative method that does not involve the femtosecond laser. It is proposed that one route would be to use electrical methods. This could lead to more lab-on-a-chip type set-ups that would make these techniques much more accessible to industry and other research groups. This is the main driving force behind the work in this thesis: to develop techniques that allow the electrical detection and generation of high frequency acoustic signals.

One potential application is the acoustic probing of structures on the nanometre scale, as a form of non-destructive testing. Much as ultrasound techniques have become extremely useful as an imaging tool on the millimetre scale, the higher frequencies and therefore smaller wavelengths of the acoustic signals used in picosecond acoustic techniques would allow the imaging of much smaller structures down to the nanometre scale. This technique would probably not become a mainstream diagnostic tool for mass produced items, but it would certainly find uses in small scale semiconductor device manufacture and several research areas that do not have access to powerful lasers. Another potential application is in the development of devices that could be used in THz communications systems and sensors. Existing methods of producing electromagnetic signals in the hundreds of gigahertz frequency range for use as the local oscillator signal in such systems tend to be both expensive and complicated, as it is not possible to generate the high frequency signal required with a single device. Instead, a microwave source such as a Gunn diode oscillator is used, followed by a chain of multipliers. Using an acoustic source for the local oscillator, such as a SASER device, could provide a method of generating a signal with a frequency of hundreds of gigahertz using a single device, which would significantly reduce the complexity of such systems.

The combination of acoustics and electronics is far from new. The term “acoustoelectric effect” was first used in the literature in the late 1950s to describe the generation of a DC voltage in the propagation direction of an acoustic wave travelling in a material that contained free carriers. Early experiments observing this effect were performed on *n*-type germanium [30, 31]. Prior to this, acoustics were already being employed in existing

electronics systems in the form of acoustic delay lines in early computer memory devices [32]. Tubes of mercury were used to store a train of acoustic pulses that were generated by a speaker at one end and detected by a microphone at the other.

Current devices that combine acoustics and electronics tend to use surface acoustic waves (SAWs). An electrical signal can be converted into a SAW, and vice versa, by an “interdigital transducer” formed of two interleaved comb shaped contacts and the piezoelectric effect [33]. SAW filters are commonly used in mobile telephones and other signal processing applications, but typically only at frequencies up to a few gigahertz [34, 35]. SAW devices are also used as sensors in a variety of applications including gas and chemical sensors, which typically involve the incorporation of the SAW device into an oscillator circuit [36, 37], and detectors for remote RF signals that can either be active, semi-active or passive [38, 39]. Acoustically driven electron transport has been observed using SAWs in a one-dimensional channel [40] and in a resonant tunnelling device [41], but again only at frequencies up to a few gigahertz. To be able to use electronic methods for picosecond acoustics, techniques and devices need to be developed that can be used at higher frequencies in the hundreds of gigahertz range.

It has recently been shown that the energy levels in semiconductor heterostructures can be modified on the ultrafast time scale by the presence of propagating strain pulses [28]. This provides a possible route into developing the devices required to detect picosecond acoustic pulses electrically. This was followed by further investigation of semiconductor devices that are capable of responding to an ultrafast strain pulse.

It was shown that a picosecond strain pulse could drive a current through both a thin semiconductor layer and a semiconductor heterostructure in the absence of an applied electric field via the acoustoelectric effect [42], but the speed of the detected response was strongly limited by the bandwidth of the detection electronics. Different routes were then considered for devices that could respond on a faster time scale.

Ultrafast acoustic wavepackets were detected by measuring the photocurrent generated in quantum wells embedded in *p-i-n* and undoped pla-

nar structures [43,44]. A laser was required to generate the carriers in the well that formed the photocurrent, and changes in the photocurrent were observed due to the strain induced modulation of the energy levels in the quantum well. As a laser was still involved in the detection process, this method is not a fully electrical detection mechanism. However, it provides good evidence that strain can modify the currents present in semiconductor heterostructures on a sufficiently short time scale.

In parallel, experiments were performed on  $p$ - $n$  junctions [45,46], Schottky diodes [47] and double-barrier resonant tunnelling diodes [48]. In these studies the transient current through the devices caused by incident strain pulses was detected by an electrical method that did not require use of a laser. The work by Moss *et al.* on Schottky diodes is of particular relevance to this thesis.

Semiconductor superlattices are another set of devices that have huge potential as ultrafast acoustoelectric devices. Research into superlattice structures is a large and ongoing field of research in itself, including studies into both the fundamental properties of superlattices and the development of devices for practical applications. Largely, the studies so far have involved optical techniques [23,49,50], but there are some previous examples of superlattices generating a transient electronic signal in response to an incident heat pulse [51,52]. A more recent study has been published of a semiconductor superlattice responding to a periodic train of strain pulses with a transient voltage signal [53].

## 1.1 Thesis outline

A brief outline of the chapters in this thesis will now be provided. This first chapter was intended to give a context for this thesis and to provide an overview of the relevant literature. As stated, the main motivation of this work is to extend the extremely useful technique of picosecond acoustics by finding an electrical method to generate and detect strain pulses so that these types of measurement can be performed without the need for femtosecond laser systems.

Chapter 2 covers useful background information relevant to ultrafast acoustoelectric effects. The existing methods of generation and detection of high frequency strain pulses and heat pulses in semiconductors and metal films are covered in more detail, followed by a discussion of some of the effects observed when these acoustic pulses propagate through gallium arsenide. The relevant electron-phonon coupling mechanisms are presented, and their relative contributions compared. The chapter is concluded by expanding on the discussion of previous work on semiconductor devices that produced an electronic signal in response to a picosecond strain pulse, as this is directly relevant to this thesis. Recent work includes devices containing quantum wells, Schottky diodes, and resonant tunnelling diodes.

In Chapter 3, the main experimental methods and sample processing techniques are presented. Semiconductor wafers grown by molecular beam epitaxy at the University of Nottingham were used in this work and had to be fabricated into working devices. Many of the techniques used were applicable to all devices. This is followed by some of the common set-ups for experiments performed in the laboratory to obtain the results presented in later chapters.

Chapters 4 and 5 contain experimental results and the discussions of those results. Necessary background information relating to a specific device or experiment are contained in the relevant chapters.

Chapter 4 explores the use of a Schottky diode as a detector of ultrafast strain pulses, directly expanding on the work of Moss *et al.* [47]. It is confirmed that the Schottky diode does indeed respond to picosecond strain pulses with a transient voltage. This work is then advanced, as the first evidence of heterodyne mixing of coherent acoustic phonons with W-band microwaves using a Schottky diode is demonstrated. This allows the frequencies present in a high frequency acoustic pulse to be determined electrically as they are down converted to frequencies that are more easily processed by currently available electronic instrumentation.

Chapter 5 investigates the electronic response of semiconductor superlattice devices to incident picosecond acoustic wavepackets. A transient voltage is generated across the superlattice in response to the acoustic pulse, and this detected signal shows possible evidence of confinement of

certain acoustic modes within the superlattice. This is investigated for a range of conditions and the results presented are compared to other works on similar structures that did not observe this effect.

Chapter 6 concludes this thesis and recalls key points made in the previous chapters. Suggestions for relevant further work are presented, including the use of a step recovery diode as a possible device for the electrical generation of strain pulses to compliment the electrical detection techniques.

# Chapter 2

## Background

This chapter introduces some of the background material that is relevant to the experiments performed in this thesis and the associated discussions. This includes the optical generation of coherent strain pulses in metals, bulk semiconductors and superlattice structures along with the generation of incoherent heat pulses. This is followed by the propagation of these phonons through a bulk semiconductor substrate, focussing on attenuation and dispersion. Two existing and complimentary techniques for the detection of phonons are then described: an optical method and the use of superconducting bolometers.

The presence of strain in a semiconductor device affects the energy levels of the electrons and holes within the structure. There are several different potential mechanisms for this, and these are briefly considered. The deformation potential dominates for longitudinal acoustic phonons, while for transverse acoustic phonons the main coupling mechanism is the piezoelectric effect.

The chapter is concluded by a more detailed description of the previous work on semiconductor devices that are capable of producing a fast electronic response to a picosecond strain pulse. This includes quantum wells embedded in both *p-i-n* diodes and undoped planar structures, Schottky diodes and double-barrier resonant tunnelling diodes.

## 2.1 Generation, propagation and detection of acoustic waves

### 2.1.1 Generation of strain pulses

The optical generation of very short, coherent strain pulses is a widely used technique in picosecond acoustics and has been well documented [1,3,7,8].

Consider the case in which a short duration light pulse of energy  $E$  is incident on the free surface of an opaque film of thickness  $w$ , as discussed by Thomsen *et al.* [1] and illustrated in figure 2.1. Assume that the absorption length of the light,  $\zeta$ , is short compared to the thickness of the film,  $w$ , where  $\zeta$  is the distance into the material over which the light intensity is reduced to  $1/e$  of the intensity just inside the material. It is also assumed that the linear dimensions of the area  $A$  illuminated by the light pulse are large compared to  $w$  and  $\zeta$ . The energy deposited into the film at a distance  $z$  from the surface leads to a temperature rise in the film given by Thomsen *et al.* as the following expression:

$$\Delta T(z) = (1 - r) \frac{E}{AC_V \zeta} \exp\left(\frac{-z}{\zeta}\right) \quad (2.1)$$

where  $r$  is the reflectivity and  $C_V$  is the specific heat per unit volume of the film [1]. The temperature rise in the sample causes an isotropic thermal stress given by

$$\sigma = -3B\beta\Delta T(z) \quad (2.2)$$

where  $B$  is the bulk modulus of the film and  $\beta$  is the linear expansion coefficient.

Since the stress depends only on  $z$ , the only motion is parallel to  $z$  and longitudinal acoustic waves are generated that propagate along the direction perpendicular to the surface of the film. A change in temperature at any given point sets up acoustic waves that travel in both the positive and negative  $z$  directions. The negative-going pulse is reflected from the free surface of the film with a phase change of  $\pi$ . The total strain pulse is the sum of the initial positive-going pulse and the inverted reflected pulse, leading to a bipolar shaped strain pulse. The width of the strain pulse is of the order of  $2\zeta$ .

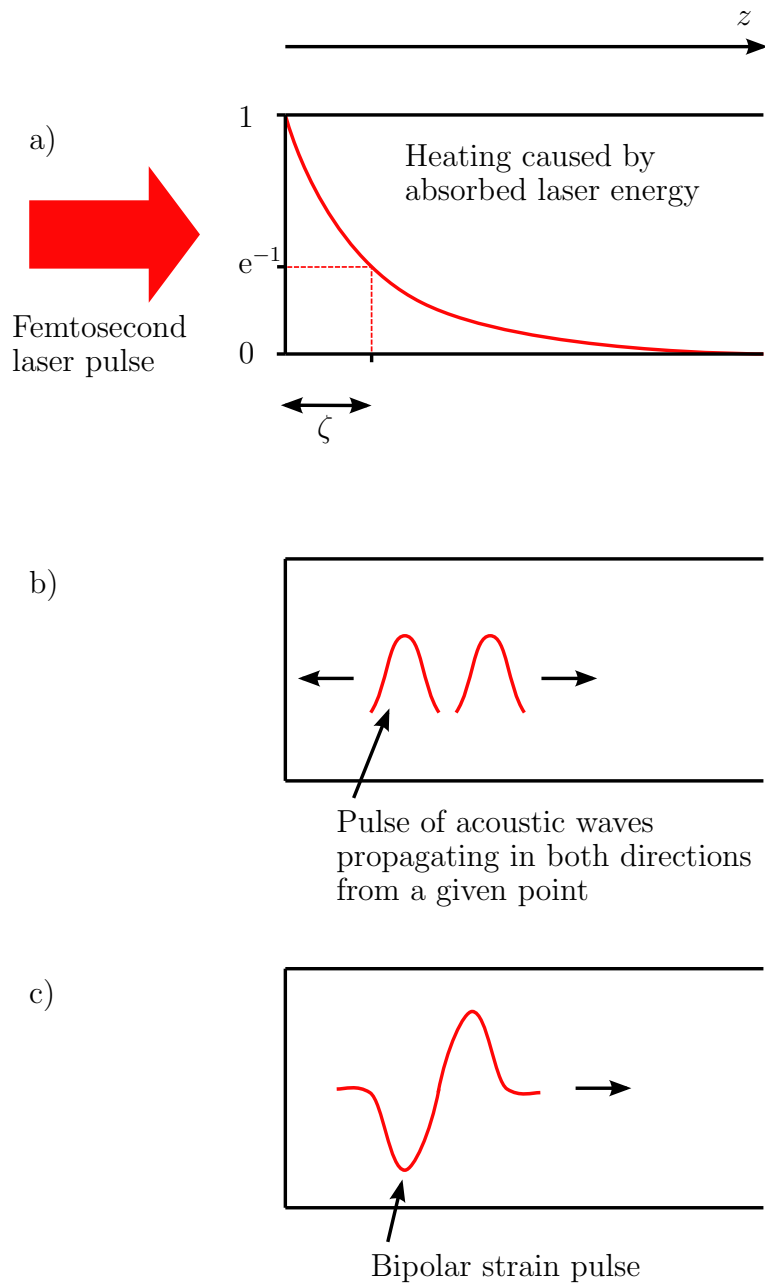


**Figure 2.1:** Illustration of the optical generation of a bipolar strain pulse. a) The heating of the sample as a function of the distance into the sample  $z$ , where  $\zeta$  is the absorption length of the laser light in the material. b) Acoustic waves generated at a given point propagate in both the positive and negative  $z$  directions. c) The negative-going pulse experiences a  $\pi$  phase shift upon reflection at the surface, forming a bipolar strain pulse.

This model describes a macroscopic view of the system and makes several assumptions. It has been assumed that the area heated by the light pulse is very large compared to the thickness of the film. This allows the assumption to be made that  $\Delta T$ ,  $\sigma$  and the strain,  $\eta$ , depend only on the distance from the surface,  $z$ . This is true for the “near-field” regime of a distance of  $z \sim \frac{D_L^2}{\zeta}$ , where  $D_L$  is of the order of the diameter of the laser focal spot size. Outside of the “near-field” regime the shape of the strain pulse will change due to dispersion and attenuation. It has also been assumed that the temperature rise in the film occurs instantaneously and that the temperature remains constant after the initial rise. These latter two assumptions will be discussed in more detail.

First, consider the assumption that the temperature rise in the film occurs instantaneously. In reality, the laser pulse will not transfer all its energy to the film instantaneously as it will have a finite time duration  $\tau_l$ . During this time the strain pulse will move a distance  $v_s\tau_l$ , where  $v_s$  is the speed of sound in the film. If  $v_s\tau_l$  is very small compared to the spatial length of the strain pulse, the finite duration of the laser pulse will not be important. For this assumption to be applicable, the following condition must be satisfied:

$$v_s\tau_l \ll \zeta \tag{2.3}$$

The shortest absorption lengths are those in metals, where  $\zeta$  can be as small as 10 nm. A typical sound velocity is 4000 ms<sup>-1</sup>. Under these circumstances the condition in equation 2.3 becomes  $\tau_l \ll 2.5$  ps. The laser pulses used in the experiments performed in this thesis typically had a time duration <0.1 ps, and it is valid to neglect the finite duration of the laser pulse.

It was also assumed that the temperature of the film remains constant after the initial rise, and this is related to heat flow in the film after the laser light is absorbed. This heat flow affects the shape of the bipolar strain pulse produced and depends heavily on the factor  $D_T/v_s\zeta$ , where the thermal diffusivity  $D_T = K/C_V$ , where  $K$  is the thermal conductivity. Values of  $D_T/v_s\zeta$  can vary over 3 orders of magnitude. The largest values are in metals at room temperature, where the value is typically between 0.2 and 2, and heat conduction has the effect of broadening the shape of the generated pulse. For dielectric glasses the value can be 0.01 or smaller and heat conduction makes very little difference to the shape of the strain

pulse.

By treating the process simply in terms of heating there are some effects that have not been accounted for. The light pulse changes the electron and phonon distribution functions and these changes also lead to a stress generated in the sample. Several other effects need to be considered to form a more accurate description, which will now be briefly outlined.

In metals, the energy of the light pulse is initially transferred to the electrons, and the electron system will not be in equilibrium with the lattice. The electrons can diffuse a significant distance into the metal film, up to approximately 100 nm [3], before the energy is transferred to the lattice by electron-phonon collisions. The energy from the light pulse is then distributed over a thickness larger than  $\zeta$  and this leads to a broadening of the strain pulse. This effect was investigated by Tas and Maris [3].

In semiconductors, the presence of the light pulse causes electron-hole pairs to be formed. The excited carriers can generate a stress due to the deformation potential [8]. Excited carriers relax to the band edge by producing phonons and the presence of these phonons provides another contribution to the stress in the material. In piezoelectric materials stress can be generated by the spatial separation of electrons and holes creating a transient electric field. These mechanisms for generating stress give rise to further strain generated in the sample.

The spectrum of the generated strain pulse will be broad with an approximately Gaussian shape. Thomsen *et al.* [1] state that the spectrum peaks at a frequency  $f$  of approximately  $\frac{v_s}{2\zeta}$ . To produce a broad spectrum with high frequency components it is therefore typical to use a laser wavelength that is strongly absorbed in the medium. In this way, the absorption length  $\zeta$  is as short as possible.

### 2.1.2 Generation of strain in superlattices

Semiconductor superlattices (SLs) are layered structures formed of alternating layers of two different materials. This new artificial periodicity is of great interest scientifically and is discussed in greater detail in Chapter 5.

Optical generation of high frequency, narrow bandwidth acoustic modes within these layered structures has been observed using pump-probe reflectivity measurements with the pump and probe beam focussed on the same surface of the superlattice structure [23, 54].

When using GaAs/AlAs semiconductor superlattices for this purpose, it is common to use a laser with a frequency that is tuned to the first electron-heavy hole transition in the GaAs wells [23, 29, 55, 56], and the generation process can be thought of in the following manner. Light absorption in the GaAs wells generates additional carriers in the quantum wells and this causes the layers of the structure to become strained. As the strained layers relax, an acoustic wave is formed with a wavelength that is comparable to the period of the superlattice. As the structure is periodic, waves generated from each GaAs layer add in constructive superposition; this leads to the generation of high frequency coherent phonons in a narrow frequency range.

It was first demonstrated that phonons generated in a SL could “leak” out of the SL and propagate through the semiconductor substrate by using an incoherent superconducting bolometer as a detector [56]. The coherence of these generated phonons was later confirmed by Huynh *et al.* using an optical pump-probe technique in which the two beams were focussed on opposite sides of the semiconductor substrate to isolate the generation and detection processes [49].

The generation of strain in a SL differs from the generation of strain pulses in bulk semiconductors or thin metal films as the SL produces a narrow frequency band of acoustic phonons instead of a broad spread of frequencies. This can be useful for experiments in which a single-frequency source is required. The disadvantage of this method is that the SL must be grown by molecular beam epitaxy, and as it is a fixed structure the generated frequency is not tunable.

### 2.1.3 Generation of heat pulses

Heat pulse experiments were performed long before picosecond strain pulse measurements, with the earliest example of these type of experiments in solids performed by von Gutfeld and Nethercot in 1964 [57]. This technique

was used extensively in the study of phonon focusing [58,59], but it has also been used to study other effects such as electron-phonon interactions [60].

The most common method of generating heat pulses in non-metallic crystals is by heating a thin metal film that has been thermally evaporated onto the sample. The metal film can be heated either electrically with a current pulse or optically with a pulsed laser [61]. Excited electrons in the metal film relax by phonon emission and a pulse of phonons is generated [62]. The heated metal film can be modelled as a Planck radiator, and as such the emitted pulse of phonons has a broad Planckian spectrum with a peak at a frequency  $f$  given approximately by the relationship  $hf = 3k_B T$ , where  $h$  and  $k_B$  are the Planck and Boltzmann constants, respectively, and  $T$  is the heater temperature [63]. This peak is at a much higher frequency than for coherent phonons generated in a metal film [1], and the heat pulse frequencies can extend up to a few terahertz [62]. Each point of the heater acts as an independent source of propagating acoustic waves, leading to incoherent phonons that are emitted isotropically from each point of the source.

As heat pulses are formed when a metal film is heated by a laser, they are also formed when generating picosecond strain pulses by the optical method described in section 2.1.1, due to the relatively slow thermal relaxation of the film after the strain pulse has been launched [42]. The heat pulses generated in this situation can often be ignored in experiments that require the propagation of the acoustic pulse across a thick substrate, as the heat pulses have a spread of propagating speeds due to dispersion and scattering of the phonons within the substrate. As such, the average arrival time for the heat pulse phonons is later than that of the strain pulse [64].

#### 2.1.4 Propagation

After an acoustic pulse is generated either optically or electrically, it propagates into the rest of the semiconductor sample. In most of the experiments described in this thesis the acoustic pulse then had to travel across some thickness of GaAs substrate before being detected on the other side.

During this propagation the magnitude and form of the acoustic pulse

can change due to attenuation and dispersion of the phonon wavepacket within the substrate. These effects are discussed in this section. At high enough strain values non-linear effects become apparent and the formation of acoustic solitons occurs. The key experiments described in this thesis were performed using strain amplitudes small enough to remain in the linear regime, and this effect is not discussed further.

There is a key difference between the propagation of the coherent strain pulse and the incoherent heat pulse generated by the methods discussed. The coherent strain pulse will propagate in a narrow collimated beam due to the large area over which the heat is absorbed in comparison to the absorption length [1]. In contrast, the incoherent heat pulse phonons are emitted isotropically from each point in the source [63].

## **Attenuation**

Attenuation of acoustic phonons as they propagate across a sample can be problematic in experiments where the phonons travel a substantial distance before detection, as the size of the detected signal can be severely reduced. Two different theoretical approaches to the attenuation of sound waves have been developed [65]. One treats the sound wave microscopically, and considers collisions of individual acoustic phonons with thermal phonons present in the substrate material. The other approach is macroscopic and treats the strain pulse as a whole, which can act as a driving force on the thermal phonon system.

In the latter case, the acoustic attenuation arises due to a relaxation process. The acoustic phonons can be considered collectively as a strain field, which shifts the frequencies of each thermal phonon. The thermal phonon system is then disturbed from its equilibrium. The system tends to return to equilibrium by collisions between the thermal phonons [13,65].

The temperature dependence of the attenuation of longitudinal phonons with a frequency of 56 GHz propagating in GaAs was investigated in detail by Chen *et al.* [13]. It was found that the attenuation had a significant effect at room temperature, but the attenuation decreased strongly with decreasing temperature. At temperatures of 70 K and below there was no

discernible attenuation observed. For this reason, picosecond ultrasonics experiments are generally performed at temperatures below 70 K to reduce the attenuation [14].

Processes other than relaxation were also considered in the Chen paper. One of these was the Herring process, which treats the attenuation in terms of individual phonon collisions. The most important phonon collisions to consider are three-phonon processes in which an acoustic phonon collides with a thermal phonon to produce another phonon. It was found that the Herring process led to an attenuation of the acoustic wave that was 2 orders of magnitude smaller than the measured effect, and so was not a significant contribution to the overall attenuation. This mechanism was expected to become important at high frequencies, in excess of 500 GHz [13].

Chen *et al.* concluded that it was most appropriate to use the more classical approach of treating the strain wave as a whole, when considering the attenuation of an acoustic wave with a frequency of 56 GHz propagating through GaAs. The dominant mechanism causing the attenuation of the acoustic wave is then the transfer of energy from the strain field to the thermal phonon bath.

For the experiments in this thesis, attenuation of the propagating acoustic wave did not have a big impact on the results. Experiments using samples with thick substrates on the order of 300  $\mu\text{m}$  were performed at a temperature of 4 K in a continuous flow cryostat, so attenuation of the phonon wavepacket in this case was negligible. Some experiments were performed at room temperature, but in these cases the substrate was thin, in the range of 11-17  $\mu\text{m}$ . There is a substantial attenuation present at room temperature, but the substrate was thin enough that a sufficient number of phonons made it across the substrate to still perform the experiments.

## Dispersion

Dispersion also affects acoustic wavepackets containing high frequency components as they travel through a crystalline substrate. This effect arises from different frequency components propagating through the material at different speeds. The effect can be significant if the acoustic waves travel

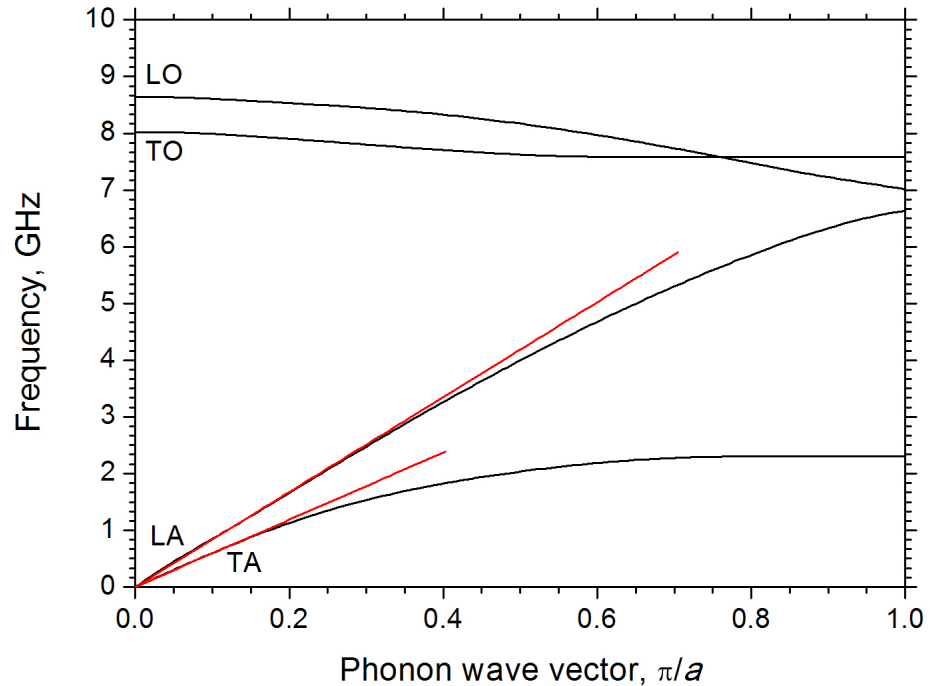


**Figure 2.2:** Phonon dispersion in the  $\langle 100 \rangle$  direction in GaAs at room temperature after Waugh and Dolling [66], where  $a$  is the lattice spacing of GaAs. The four branches of the phonon dispersion are shown; two are acoustic (A) and two are optical (O). These can be either longitudinal (L) or transverse (T) in polarisation. The linear fits are the speed of sound for the LA and TA phonons.

far enough through the substrate, with higher frequencies travelling slower than the lower frequencies. This leads to an acoustic pulse with a dispersive tail, with oscillations of increasing frequency towards the end of the tail.

This is evident when looking at the dispersion relation in GaAs measured by Waugh and Dolling using inelastic neutron scattering [66] and shown in figure 2.2. In the long wavelength limit the dispersion relationship is approximately linear for the acoustic phonon branches:

$$\omega_q = v_s q \quad (2.4)$$

where  $\omega_q$  is the angular frequency of a phonon of wave vector  $q$  and  $v_s$  is the phase velocity (speed of sound) for the appropriate acoustic phonons. This is emphasised in figure 2.2 with the inclusion of straight lines showing the appropriate speeds of sound for the different branches [67]. Low frequency

phonons in this linear regime will not have any dispersion as they all have the same group velocity, which is given by

$$v_q = \frac{d\omega_q}{dq} \quad (2.5)$$

Phonons with the same group velocity travel at the same speed, and no dispersion is observed for acoustic pulses that only contain low frequencies.

As the phonon wave number  $q$  increases, the dispersion relationships for the acoustic phonon branches cease to be linear and instead become increasingly sublinear. In this regime, phonons with larger frequencies have smaller group velocities and so they travel across the substrate slower. For large enough propagation distances this leads to a broadening of the detected acoustic pulse and eventually an oscillatory tail. This was confirmed experimentally by Hao and Maris in GaAs and other materials [15].

The frequency spectrum of heat pulses generated in a metal film extends to much higher frequencies than those present in the coherent strain pulses generated in the same film [1, 62]. The effects of dispersion are then more significant for the heat pulses. When comparing longitudinal acoustic and transverse acoustic phonon branches, the dispersion for LA phonons continues to be approximately linear up to higher phonon frequencies when compared to the TA phonons [66]. As such, dispersion will be more apparent for the TA heat pulse as the dispersion starts to occur at a lower frequency for TA phonons.

### 2.1.5 Detection

In existing optical pump-probe experiments, detection of the acoustic pulse typically involves measuring changes in the optical reflectivity of the sample. One commonly used method is the observation of changes in the probe beam reflected from the surface using a photodiode detector [1, 3, 13, 28]. Alternatively, an interferometric method can be used that allows the investigation of both the amplitude and the phase changes of the reflected beam caused by changes in the refractive index and the surface deflection [9, 10, 18, 19].

In both cases a laser beam is split into two parts to form the pump and

the probe. The pump beam generates the acoustic wavepacket in either a semiconductor or a metal film. The probe pulse is delayed in time relative to the pump pulse, to coincide with the presence of the strain pulse near the surface of the sample. One of the optical paths typically includes a variable length optical delay line, which allows the acoustic wavepacket to be probed at different times. For large strain propagation distances, the optical delay required can become long enough to be impractical. In this situation, techniques to use later laser pulses to introduce the time delay can be employed [15].

The main mechanism exploited in this detection method is the strain induced modulation of the refractive index of the material. This leads to a change in the reflectivity of the sample when the strain is near the sample surface. The strain at small distances from the surface, comparable to the optical absorption length  $\zeta$ , also has an effect on the reflectivity changes, so this method effectively integrates the strain over the absorption length. For this reason, the laser beam photon energy is typically larger than the band gap energy of the semiconductor material, so that the laser energy is absorbed in a thin layer of material near the surface. This reduces the broadening of the detected signal caused by detecting the strain pulse over a finite distance from the sample surface.

An alternative, incoherent method to detect phonon wavepackets after propagation across the sample uses a superconducting bolometer [56]. Superconducting bolometers are typically fabricated from a thin film of aluminium, which is cooled such that it is held at its superconducting transition. A slight change in the temperature of the bolometer caused by incoming phonons pushes the bolometer up its transition, which leads to a large change in the resistance of the device, as illustrated in figure 2.3. A change in the bolometer temperature of just 0.1 K can lead to a change in the resistance of the bolometer  $\sim 200 \Omega$ . The bolometer is then very sensitive to the phonon flux incident upon it.

This method is complimentary to the optical detection methods described previously in this section, due to its simplicity, its sensitivity to changes in phonon flux, and its ability to distinguish between different phonon modes due to their different propagation speeds [64]. The superconducting bolometer is a useful measurement device for time-of-flight

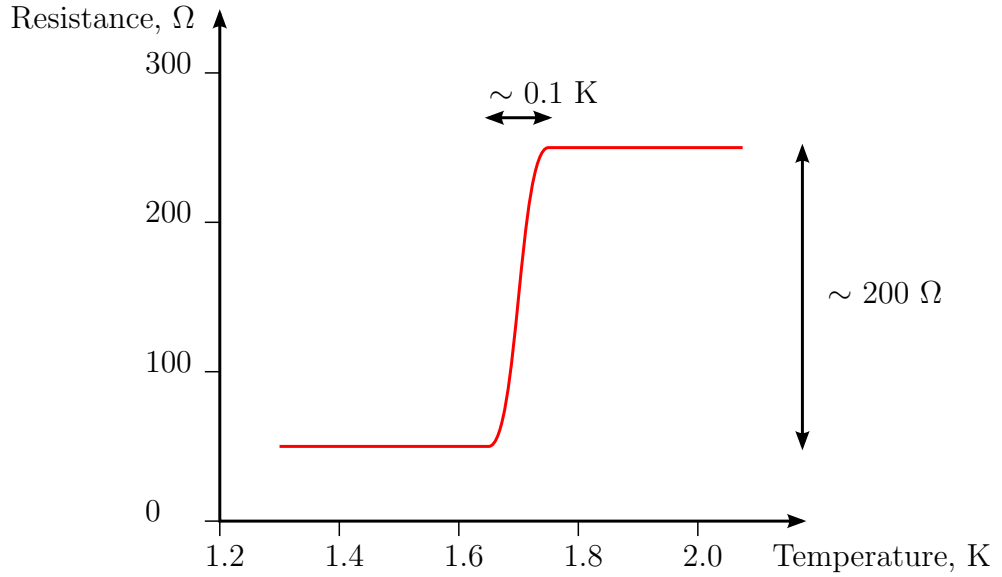


**Figure 2.3:** Illustration of the superconducting transition of a typical bolometer. A very small change in temperature of the bolometer  $\sim 0.1$  K leads to a large change in the resistance of the bolometer  $\sim 200$   $\Omega$ .

experiments [56, 68] and for comparing the power in a phonon pulse for different generation conditions [60, 69, 70].

## 2.2 Electron-phonon coupling mechanisms

This section will briefly address the different electron-phonon coupling mechanisms that are relevant when considering the effects of strain on the electronic properties of a semiconductor device. These include the deformation potential [71], the piezoelectric effect [72], the Pekar mechanism [73, 74] and the ripple effect [75].

The deformation potential and the piezoelectric effect are the two dominant effects in this work, and so this section will concentrate on these two. The deformation potential is the main coupling mechanism for longitudinal acoustic phonons, whereas in the case of transverse acoustic phonons it is the piezoelectric effect.

### 2.2.1 Deformation potential coupling

The term “deformation potential” was first introduced by Bardeen and Shockley in 1950 for an effect that they described as a variation in the position of the energy band boundary in the presence of an acoustic wave [71]. The presence of strain within a semiconductor material modulates the lattice spacing of the semiconductor, and the difference in the atomic spacing changes the band gap of the bulk material. The energy shift of the band edge  $\delta E_{edge}$  caused by the deformation potential is

$$\delta E_{edge} = \Xi \eta \quad (2.6)$$

where  $\Xi$  is the deformation potential in the material and  $\eta$  is the size of the strain present.

Several different methods have been used to determine the deformation potential of GaAs both theoretically and experimentally and these give a spread of results depending on the exact method used and the assumptions made in the fitting equation [76]. Typically for the conduction band in GaAs the value of the deformation potential  $\Xi \sim -10$  eV [76–78], where the negative sign represents the fact that the band gap increases when the crystal is compressed. A more recent review paper has considered the documented values and recommends the use of  $\Xi = -7.17$  eV for the conduction band of GaAs [79].

At the  $\Gamma$  point of GaAs, the deformation potential is an electron-phonon interaction that only applies to longitudinal acoustic phonons. For symmetry reasons the deformation potential constant for transverse waves is zero at or close to the  $\Gamma$  point, and coupling of TA phonons to electrons must occur by another mechanism [76].

### 2.2.2 The piezoelectric effect

The piezoelectric effect is the generation of an electric field due to the application of strain to a crystal that lacks an inversion symmetry [72]. In a material that possesses inversion symmetry, if one could change the position of each particle to its inverse position relative to a defined origin, the material would stay the same. The zincblende structure of GaAs does

not have an inversion symmetry due to the position of the arsenic sites relative to the gallium sites, and so GaAs is a piezoelectric material [80]. There are several reasons why piezoelectricity occurs: the displacement of the ions that form the lattice structure, the displacement of electrons within the material, and a change of ionicity of the material [81].

The cubic symmetry of the GaAs crystal only allows one value of the piezoelectric tensor to be non-zero. Shear strain is required to generate piezoelectric coupling in GaAs grown in the  $\langle 100 \rangle$  direction [72]. As such, the piezoelectric effect is an important electron-phonon coupling mechanism for transverse phonons, but it is not relevant for longitudinal phonons. The values of the relevant piezoelectric constants of GaAs are well defined as several groups found values that were in good agreement with one another, unlike the value of the deformation potential [81].

## 2.3 Preliminary work on high frequency acoustoelectric techniques

After the discovery that ultrafast strain could be used to shift the energy levels in semiconductor heterostructures on the picosecond time scale via the piezospectroscopic effect [28], the strain modulated electronic transport has been investigated for several semiconductor devices. These devices provide the first evidence that ultrafast strain pulses can be detected electrically and it is the work in these papers that this thesis is intended to build upon.

Experiments have been performed that investigated the probing of the photocurrent in quantum wells embedded in both  $p-i-n$  and undoped planar structures, and transient strain induced currents measured in epi-layers,  $p-n$  diodes, Schottky diodes and double-barrier resonant tunnelling diodes. Some of these works are reviewed in this section.

### 2.3.1 Strain induced modulation of the photocurrent in quantum well devices

It has been shown that ultrafast acoustic wavepackets can be detected by probing the photocurrent in semiconductor devices containing quantum wells. This was first demonstrated by Moss *et al.* using a *p-i-n* structure with a quantum well (QW) embedded in the intrinsic region [43] and was later extended to an undoped planar structure containing two QWs [44]. This technique relies on the change in the exciton energy in a quantum well in the presence of uniaxial strain, also known as the piezospectroscopic effect [28]. This method still requires a laser to generate the carriers that form the photocurrent, and so it is not a technique that is independent of the laser system. However, it is an important step forward in understanding how ultrafast strain can be exploited to modify the electronic transport in semiconductor devices.

A schematic diagram of the set-up used by Moss *et al.* is shown in figure 2.4, and the experiment was performed as follows. The sample was mounted in an optical access cryostat, and cooled to a temperature of 4.7 K. The output from a femtosecond pulsed laser was split along two paths. One part formed the pump beam, which generated a strain pulse in an Al film that had been thermally evaporated onto the back face of the substrate. The strain pulse then propagated across the substrate to the device. The other part of the laser beam was delayed in time to probe the device at approximately the same time as the strain pulse arrived. The probe beam excited carriers in the quantum well, a significant proportion of which were able to escape the well to form the photocurrent. The presence of the strain pulse passing through the QW changed the exciton energy to bring it in and out of resonance with the energy of the laser. This led to a change in the number of carriers generated in the QW, and hence changed the size of the photocurrent.

To clarify how the presence of strain in the QW affects the generated photocurrent, the diagram in figure 2.5 can be considered. The photocurrent  $I_P$  depends on the difference between the laser photon energy  $\hbar\omega$  and the exciton energy  $E_0$ . This detuning  $\Delta$  changes with the presence of strain in the QW, as the strain modulates the exciton energy. In the ex-

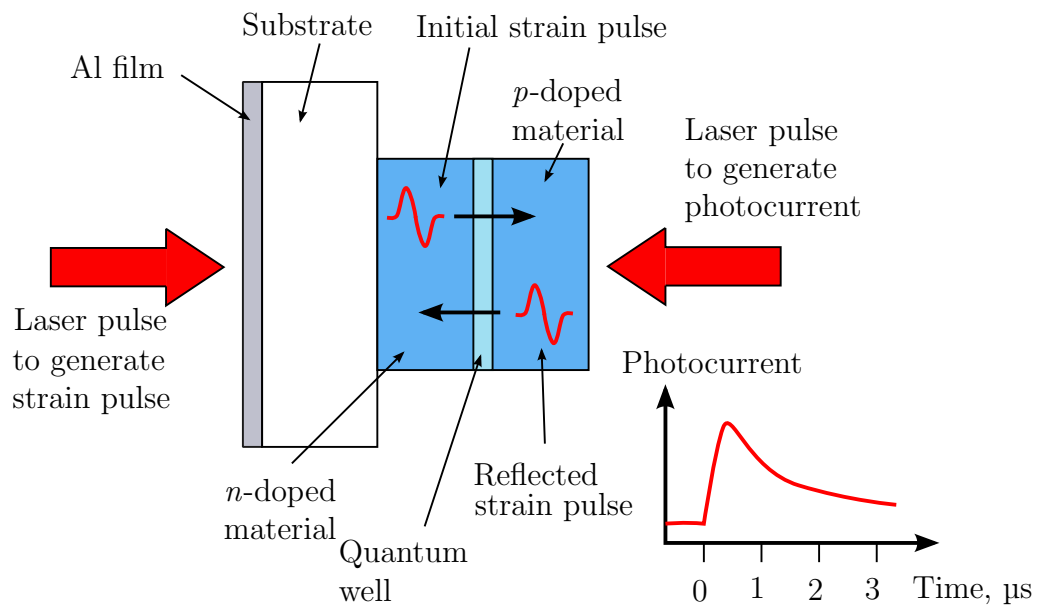


**Figure 2.4:** Schematic diagram of the experimental set-up for Moss' photocurrent experiment. The laser beam was split into two parts. One part excited a strain pulse in a thin Al film thermally evaporated onto the back of the substrate, and the other part excited a photocurrent in the quantum well (QW) embedded in the  $p-i-n$  device. A typical photocurrent signal in the absence of strain is shown. Strain pulses generated in the Al film crossed the QW once on the way to the surface of the sample, and then a second time after reflection from the top surface of the device with a  $\pi$  phase change.

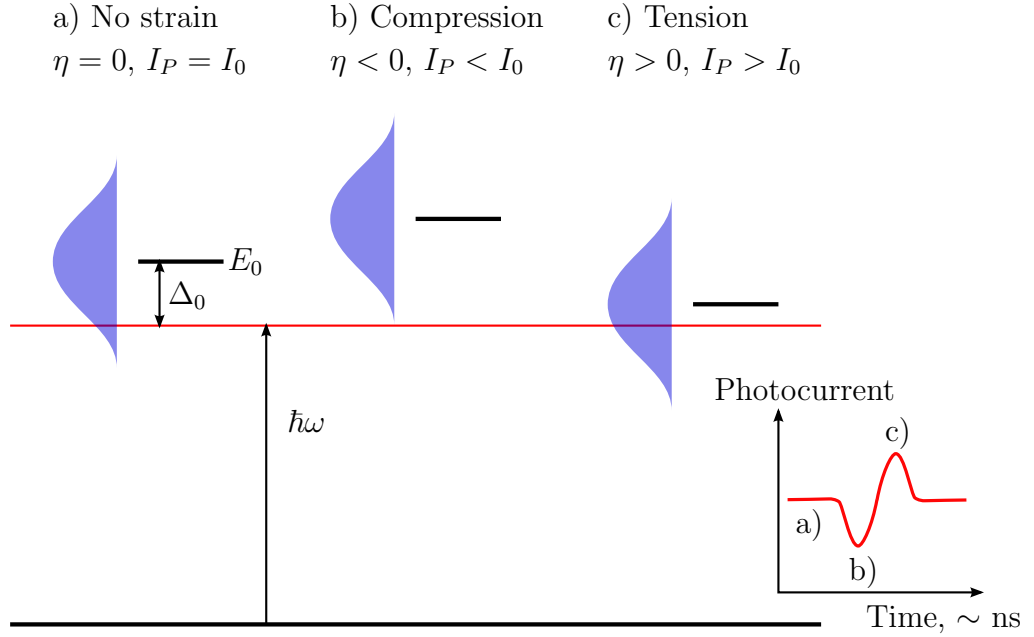


**Figure 2.5:** Diagrammatic representation of how strain modulates the photocurrent  $I_P$  in a quantum well for the case where the exciton energy  $E_0$  is larger than the laser photon energy  $\hbar\omega$ .  $I_0$  and  $\Delta_0$  are the photocurrent and detuning, respectively, when there is no strain present ( $\eta = 0$ ). The inset graph shows how the size of the photocurrent varies for the 3 different scenarios.

ample shown in figure 2.5  $E_0 > \hbar\omega$ . Let  $I_0$  and  $\Delta_0$  be the photocurrent and detuning, respectively, when there is no strain present ( $\eta = 0$ ). Under compressive strain ( $\eta < 0$ ), the exciton energy is increased, increasing the detuning. As the exciton resonance is moved further from the laser energy less carriers are generated in the QW and the photocurrent decreases. In contrast, for the tensile part of the strain pulse ( $\eta > 0$ ), the exciton energy is decreased. This leads to a decrease in the detuning and the exciton resonance becomes closer to the energy of the laser. This allows more carriers to be generated in the well and the photocurrent increases. Thus, the photocurrent follows the profile of the strain pulse propagating through the QW.

For the *p-i-n* device with a single QW in the intrinsic region, the detected photocurrent contained a bipolar pulse followed by an identical but inverted bipolar pulse [43]. The first observed pulse is the change in the photocurrent due to the strain pulse propagating through the QW on the way to the surface of the device. Upon reaching the top surface of the

device, the strain pulse experienced a  $\pi$  phase change and it was detected again in the QW on the second pass. The timing between the two pulses agrees closely with the expected time-of-flight for the strain pulse to travel from the QW to the surface and back again.

The undoped planar device studied later contained two QWs of different width [44]. The different widths led to a difference in exciton energy for the two QWs, with the wider well having a lower exciton energy. For low laser photon energy, where only the wider well exciton could be excited, the results were very similar to those seen in the single QW experiment with two bipolar pulses of opposite polarity present in the photocurrent. For higher probe laser energies there were extra pulses present in the photocurrent between these two pulses. These extra features were caused by the strain induced modulation of the exciton energy of the thinner QW, which was closer to the surface of the device. This provided further evidence that the probing mechanism was due to the piezospectroscopic effect.

### 2.3.2 Electrical detection of strain pulses using a Schottky diode

It has been demonstrated by Moss *et al.* that Schottky diodes can be used to detect ultrafast strain pulses without the need for a laser as part of the detection scheme [47]. This suggests that Schottky diodes are a strong candidate as detection devices for all-electronic picosecond acoustics experiments.

A 200  $\mu\text{m}$  diameter Schottky contact was formed onto *n*-doped GaAs using thermally evaporated Ti and Au layers, and this sample was mounted in an optical access cryostat at a temperature of 5 K. An Al film had been deposited on the back of the substrate and this was excited with optical pulses from a femtosecond laser to generate strain pulses, which propagated across the substrate to the Schottky diode. The device set-up is shown schematically in figure 2.6. Changes in the current through a series resistor were measured as a function of time. Moss saw a sharp pulse in the current at a time  $t = t_0$  corresponding to the time it took the strain pulse to reach the Schottky diode. Subsequent peaks separated by a  $2t_0$  time interval

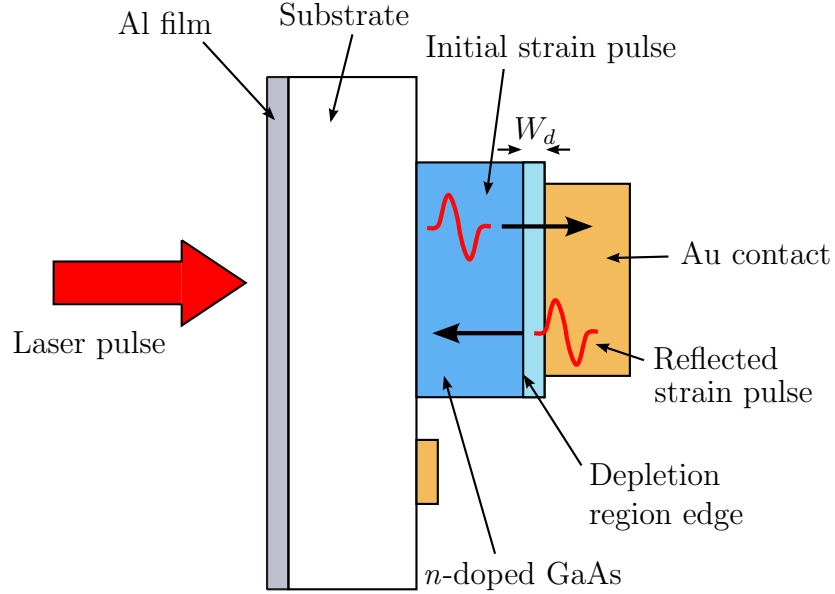


**Figure 2.6:** Schematic diagram of the device and the strain pulses in Moss' Schottky diode experiment. A pulsed laser was used to generate a strain pulse in an Al film that propagated across the sample to the Schottky diode. Upon reaching the free surface of the device the strain pulse underwent a  $\pi$  phase change as it was reflected back across the sample.  $W_d$  is the width of the Schottky diode depletion region.

were caused by reflections of the strain pulse after it propagated twice across the sample before reaching the Schottky diode again. Each detected pulse consisted of two positive peaks, separated in time on the order of 200 ps. As the negative bias across the Schottky diode was increased, the initial peak arrived at earlier times and the later peak arrived at later times as illustrated in figure 2.7.

The first peak was caused by the strain pulse passing through the Schottky diode on the way to the surface of the device, and the second peak was caused by the reflected strain pulse passing through the Schottky diode a second time. At large enough applied bias, it is easier to resolve two separate bipolar pulses in the transient current across the device, with the latter having undergone a  $\pi$  phase shift at the surface of the sample. This is very similar to the effect seen in the photocurrent in a QW in the presence of propagating strain [43]. The incident and reflected strain pulses are shown

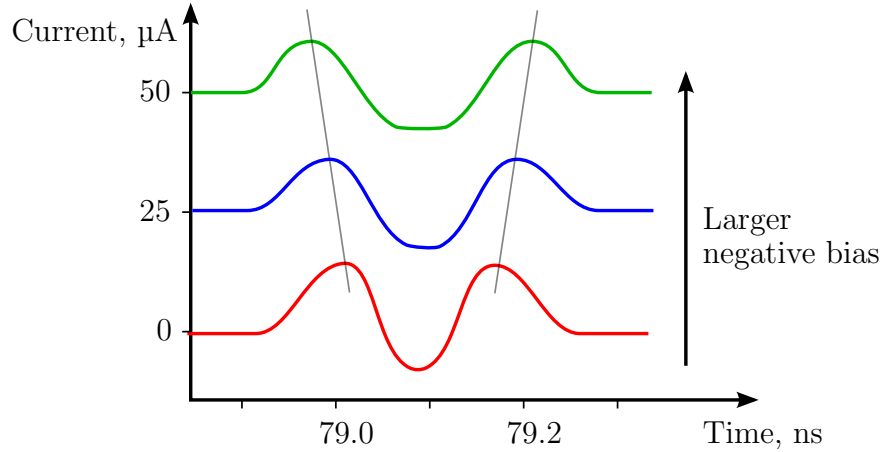


**Figure 2.7:** Illustration of Moss’ results of the temporal response of the Schottky diode to an ultrafast strain pulse [47]. For larger applied negative bias the earlier peak arrived at earlier times and the later peak arrived at later times.

in figure 2.6 for clarity.

The proposed detection mechanism in the case of the Schottky diode is the deformation potential. The presence of strain in the semiconductor causes a change to the band energies. This perturbation is partly screened by electrons in the semiconductor redistributing and generating a displacement current. When the strain passes through an electrically neutral region, the charge  $Q$  is constant and so no current is produced. However, in regions where  $Q$  is not constant, the presence of strain causes a current to flow.

The dominant detection region in the case of Moss’ work was the edge of the depletion region. The width of the depletion region,  $W_d$ , depends on the square root of the applied bias, as shown in equation 4.5. For larger negative bias the depletion region gets wider, which is consistent with the changes observed in the signal. The initial strain pulse reaches the edge of the depletion region earlier when  $W_d$  is larger. After reflecting from the surface of the sample it takes longer for the strain pulse to reach the edge of the depletion region on the second pass and the second peak appears at a later time. Another contribution to the signal is from the semiconductor-metal interface, but as the position of this interface is independent of applied bias this part of the signal did not shift in time.

### 2.3.3 Strain induced modulation of electron transport in resonant tunnelling diodes

Another semiconductor device that has recently been demonstrated as a sensitive detector of ultrafast strain pulses is the double-barrier resonant tunnelling diode [48]. As with the Schottky diode, this detection method does not require the use of a laser and so the resonant tunnelling diode provides another candidate for electrical detection of picosecond acoustic pulses.

The double-barrier resonant tunnelling device (RTD) used in the work of Young *et al.* consisted of a GaAs quantum well, formed between two undoped  $\text{Al}_{0.4}\text{Ga}_{0.6}\text{As}$  barriers, with GaAs emitter and collector layers present on the two sides of this structure. A schematic representation of the conduction band energy of the RTD under applied bias is shown in figure 2.8 for two different biasing conditions.

The current-voltage characteristics of the RTD in the absence of an applied strain are very non-linear. Under applied bias, an energy difference is formed between the emitter and collector regions of the RTD and electrons become confined in the GaAs emitter region. As the applied bias is increased it brings the ground state energy level of the quantum well (QW) in line with the Fermi energy of the emitter  $E_{FE}$ . This is the resonance threshold condition shown in part a) of figure 2.8. At this point, electron tunnelling begins to occur through the barriers in the device and a current is observed. As the bias is increased, the tunnel current increases until the resonant peak has been reached. For this to occur, the ground states of the emitter and quantum well become aligned, as shown in part b) of figure 2.8. This condition allows the maximum rate of electron tunnelling through the RTD. As the bias is increased further still, the energy level of the QW is brought out of resonance with the emitter again and the tunnel current reduces to approximately zero.

In experiments performed by Young *et al.* a strain pulse was generated optically in an Al film on the opposite side of the substrate, and this propagated to the RTD where it was detected electrically. The sample was mounted in an optical access cryostat, and cooled to a temperature of

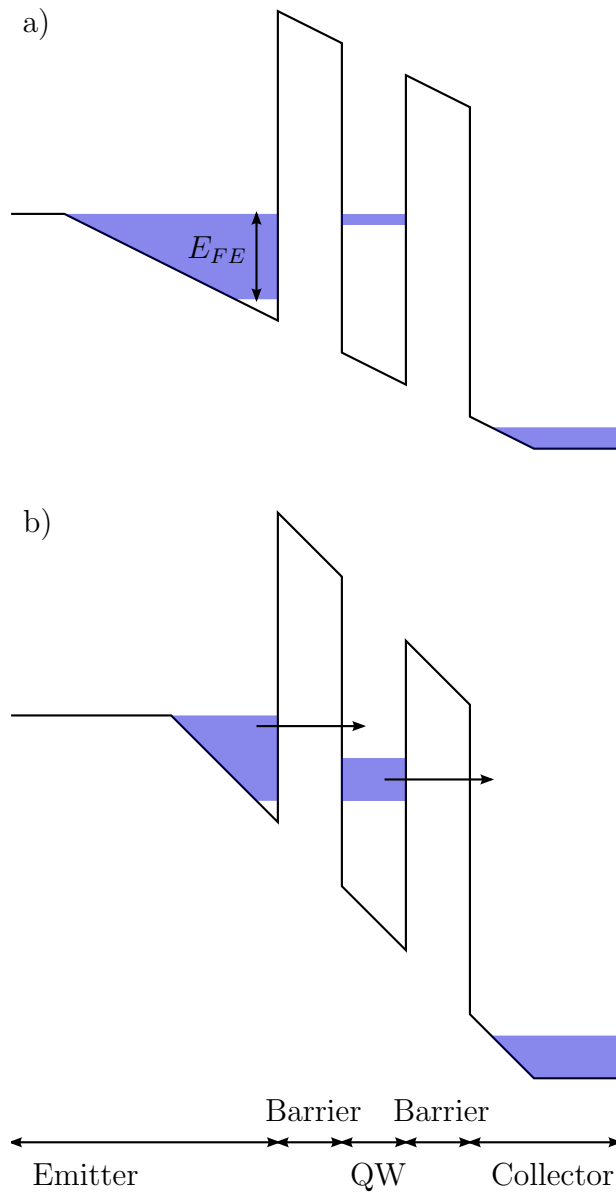


**Figure 2.8:** Schematic band diagram of a double-barrier resonant tunneling diode biased a) near the threshold for resonance and b) at the resonant peak. For certain applied biases the electrons confined in the emitter region can tunnel through the barriers to the collector to form a current through the RTD.

4.7 K. The transient current changes caused by the propagating strain were measured as a function of time for a range of applied bias. For applied biases above the resonance threshold bias a positive peak was observed in the transient current when the strain reached the QW. For applied biases close to the maximum tunnelling resonance, the peak in the current changed sign to become negative. For a larger applied bias such that the RTD was out of resonance the peak became positive again.

The presence of strain in the RTD shifts the energy levels in the emitter and QW due to the piezospectroscopic effect [28]. This can bring the well in and out of resonance with the emitter, changing the carrier tunnelling rate through the device. Thus, the presence of the strain pulse affects the charge transport through the device. As the strain pulse is of a similar spatial dimension to the RTD structure it is possible for the compressive part to be in the QW while the tensile part is in the emitter region. For a detailed analysis of how the bipolar strain pulse affects the energy levels in the RTD see reference [82].

## 2.4 Conclusion

This chapter has outlined some of the background material relevant to the experiments performed in this thesis on ultrafast acoustoelectric effects in semiconductor devices. Background material that relates only to a particular device or experiment is provided in the appropriate results chapter.

Existing methods of generating and detecting ultrafast acoustic pulses have been presented, along with features of the propagation of these acoustic pulses through GaAs. Some of the previous works on semiconductor heterostructures that produce a transient voltage in response to an incident acoustic pulse have been described. These studies have directly influenced the direction of this thesis.

The work on Schottky diodes has the potential to be expanded as part of a heterodyne detection method that mixes high frequency acoustic waves with microwaves. Another promising device for the electrical detection of picosecond strain pulses is the semiconductor superlattice, which has not

yet been studied specifically for this purpose. These themes are expanded upon in the main body of this thesis.

# Chapter 3

## Experimental techniques

This chapter describes the details of the experiments performed to obtain the data presented in the following chapters. First, the general sample processing methods, which are common for the fabrication of most of the devices, will be described. This will be followed by general details of the equipment and methods used in the experiments. Additional details specific to the fabrication of a particular device or for a certain experimental set-up are provided in the relevant chapters.

### 3.1 Device fabrication

Most of the samples used in the following experiments were processed from gallium arsenide (GaAs) and aluminium arsenide (AlAs) based semiconductor wafers grown at the University of Nottingham by molecular beam epitaxy (MBE). The samples were grown on 2 inch diameter [100]-orientated GaAs semi-insulating substrates by Dr R. P. Campion and Professor M. Henini. These were then processed in the University's clean room facility by the methods described in the following sections. The beam lead Schottky diode was fabricated by e2v at the Microwave Technology Centre based in Lincoln and provided by them for use in the experiments.

Many of the processing steps are common to the fabrication of all of the devices discussed in this thesis, and these common steps will be discussed

in this section. Fabrication details specific to a given device will then be described with the different device structures in the relevant chapter. For a step-by-step list of the processes required for the devices fabricated within the University clean room, see appendix A.

### **3.1.1 Cleaving and cleaning samples**

Initially the semiconductor wafer was cleaved into smaller chips, typically 5 mm × 5 mm in size, before devices were processed from the material. To cleave the semiconductor, the wafer was scored using a diamond scribe and snapped along the score line.

The samples were initially cleaned using a four solvent clean to remove organic and particle contaminants. The four solvents used were ethyl lactate, acetone, methanol and isopropyl alcohol. The ethyl lactate was used first as it is the best solvent of the four for degreasing the semiconductor wafer. The following solvent steps remove any residues left from the previous solvent clean. Typically the sample was soaked in each solvent at room temperature for 10 minutes, before being gently rinsed with the appropriate solvent and then dried with pressurised nitrogen gas. An exception was made after the acetone step, as a residue can be left on the surface after drying. The sample was transferred from the acetone to the methanol without performing the drying step.

The samples had to be cleaned frequently during the fabrication process, though only the latter three solvents were required for later processing steps. The samples were dehydrated after cleaning to ensure good adhesion of photoresists. To do so, the samples were placed on a hot plate with the temperature set higher than that required to bake the photoresist.

### **3.1.2 Photolithography and etching**

The samples were patterned using standard photolithography techniques. A positive photoresist, BPRS 150, was spin coated onto the samples and baked before a Karl Suss MJB3 mask aligner was used to expose the required areas to UV illumination. The exposed areas were then developed

using AZ400K developer diluted in water.

The exposed and developed regions of the pattern were wet etched to form mesas and to allow access to the bottom contact layer of the samples. The etch depth was checked periodically on a KLA Tencor D-120 AlphaStep height profiler to ensure that the required total etch depth was obtained. Several different etch solutions are available that can be used to etch GaAs and AlAs. Typically a solution of 1:1:100  $\text{NH}_3:\text{H}_2\text{O}_2:\text{H}_2\text{O}$  was used to etch the samples with an etch rate of approximately  $4 \text{ nm s}^{-1}$ .

### 3.1.3 Deposition of metals and insulating layers

Metal contacts and insulating oxide layers were deposited onto samples using an Edwards 306 coating system. The samples were patterned using the photolithography techniques described in section 3.1.2. The required material was deposited by thermal evaporation across the whole of the sample. To remove the excess material, lift-off was performed using acetone. The solvent removed the remaining resist and any material deposited on top of the resist, leaving material deposited only in the required areas.

For metal contacts, it is important to have good electrical conduction between the semiconductor and the metal. An oxide etch of 1:1 HCl and water was used prior to loading the samples into the coating system. This removes the native oxide that readily forms on the GaAs surface, ensuring good adhesion of the layers and good electrical contacts.

To form ohmic contacts to different semiconductor materials an appropriate metal must be chosen that will diffuse into the semiconductor upon annealing. Different metals are required to form good *p*-type and *n*-type contacts. For *n*-type ohmic contacts a 50:50 by mass alloy of In and Ge with a Au capping layer was used. When forming ohmic contacts on *p*-type material, a layer of Mg was deposited followed by a Au capping layer.

Ohmic contacts were annealed using an AS-One rapid thermal processor that allows precise control over the ramp and dwell times in addition to the temperature. The temperature was slowly ramped to the desired anneal temperature, held constant for a period of 30 s and then cooled back to

room temperature. A purge gas of 5% H<sub>2</sub> in Ar was used to reduce oxidation of the contacts at high temperatures.

Schottky contacts require an abrupt barrier between the semiconductor and metal and are not annealed. A thin Ti layer was first evaporated to give good adhesion between the semiconductor and the Au contact.

Insulating SiO<sub>x</sub> layers were deposited using a similar evaporation process. These layers were prone to peeling off the sample during later parts of the process, so extra care was required both in thoroughly cleaning the sample before loading it into the evaporator and in not agitating the sample too aggressively during lift-off.

### 3.1.4 Wafer polishing

The samples grown by Professor M. Henini were mounted in the MBE machine using indium on the back face of the sample. This form of sample mounting left the back surface of the wafer both rough and contaminated with indium, and this had to be removed to create a smooth, flat, contaminant free surface. If not, increased scattering of the incident laser light would prevent the effective generation of acoustic signals in the sample. A Multipol Metals Research lapping and polishing machine was typically used for this purpose, but small quantities of material could be removed quickly by polishing the sample by hand.

Initially, a mechanical lapping method, using a 14 μm diamond paste, was used to quickly remove tens of nanometres of material to remove the contamination and reduce the surface roughness. A sodium hypochlorite chemical polish (Chemlox) was then used to give the sample a very smooth surface, with a surface roughness on the order of a few nanometres. It was important for the experiments that the two faces of the sample were parallel after lapping, so optical methods were used to ensure that the sample was mounted parallel to the face of the lapping jig.

The samples grown by Dr R. Campion were mounted in such a way that the back surface remains of a high quality after the growth has been completed, and so polishing of these samples was not required.

### 3.1.5 Sample packaging

To perform electrical measurements on the devices, the samples were packaged in such a way as to be able to connect them to standard electrical cables. The samples were mounted onto copper plated printed circuit board holders using a small quantity of GE varnish. The copper pattern on the holder formed a ground plane and a  $50\ \Omega$  strip line that was connected to an SMA cable launcher.

The devices were electrically connected to the holder using a Kulicke and Soffa Industries wedge bonder with Al wire. In wedge bonding, the wire is held against the sample to be bonded by the wedge and a small amount of ultrasonic excitation is applied to adhere the wire to the sample. A loop of wire is fed out as the sample is moved and a second bond is made to the holder. The smallest device diameter that can be reliably bonded with this system is  $50\ \mu\text{m}$  using a  $17.5\ \mu\text{m}$  diameter wire. Devices of  $100\ \mu\text{m}$  diameter and upwards can be bonded using a more robust  $25\ \mu\text{m}$  diameter wire.

## 3.2 Determining I-V characteristics of devices

It is necessary to determine the current-voltage (I-V) characteristics of the device before using the device for experiments. This can be obtained by the simple set-up shown in figure 3.1. A voltage is applied to the device under test via a small-value series resistor (R) using a digital voltage source (DVS). The voltage across the resistor can then be measured by a digital multi-meter (DMM) and the current through the device can be obtained using Ohm's law. When the device has a large resistance, the voltage drop across the resistor is negligible. However, when the device resistance is comparable to that of the series resistor the voltage drop across the resistor must be accounted for when considering the voltage across the device.

The device voltage and current  $V_{device}$  and  $I_{device}$ , respectively, can be

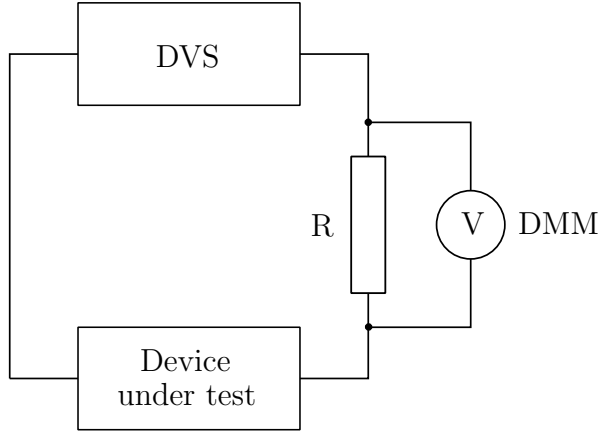


**Figure 3.1:** Set-up for I-V characteristic measurements. A bias is applied to the device under test via a series resistor ( $R$ ) using a digital voltage source (DVS). The voltage across the resistor is measured using a digital multi-meter (DMM) and can be used, along with the value of the resistor, to determine the current flowing through the device.

determined using the following equations

$$V_{device} = V_{DVS} - V_{DMM} \quad (3.1)$$

$$I_{device} = \frac{V_{DMM}}{R} \quad (3.2)$$

where  $V_{DVS}$  is the voltage applied by the digital voltage source,  $V_{DMM}$  is the voltage measured across the series resistor using the digital multi-meter and  $R$  is the resistance of the series resistor, typically  $10 \Omega$ .

### 3.3 Generating acoustic signals optically

#### 3.3.1 Broad spectrum acoustic pulses

To generate acoustic signals optically, a Spectra-Physics amplified titanium-sapphire laser system was used. A Tsunami Ti:sapphire laser generated optical pulses that were amplified by a Spitfire Pro chirped amplifier. The output of the Spitfire Pro consisted of optical pulses with a peak energy of 1 mJ, a wavelength of 800 nm, 60 fs duration and a repetition rate of 5 kHz.

The optical pulses generated by the laser were incident on the sam-

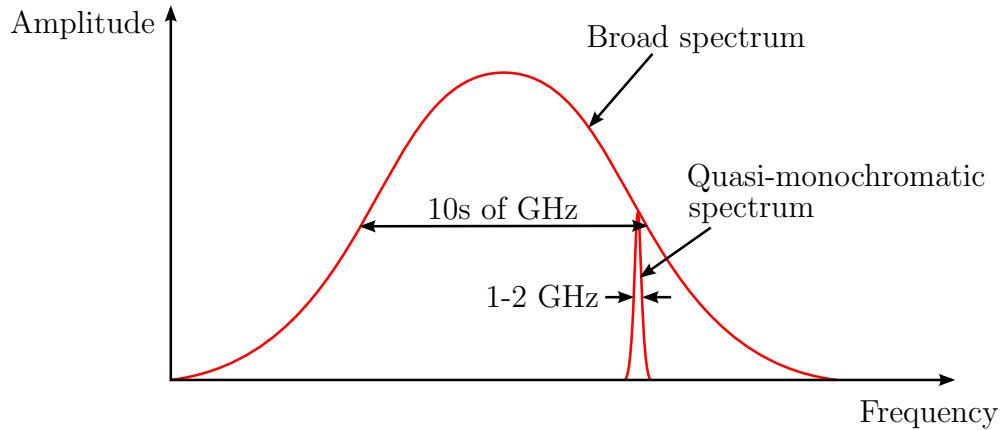


**Figure 3.2:** Illustration comparing a broad-frequency spectrum with a quasi-monochromatic spectrum. The broad spectrum has a width on the order of 10s of gigahertz, while the quasi-monochromatic signal has a width of only 1-2 GHz.

ple, via a focussing lens, to generate the required acoustic signals by the mechanisms discussed in section 2.1.1. The acoustic wavepacket could be generated either directly in the GaAs itself, or in a thin Al film deposited by thermal evaporation on the surface of the sample. A frequency doubler followed by a suitable colour filter could be used to generate optical pulses with a wavelength of 400 nm.

### 3.3.2 Narrow spectrum acoustic pulses

For frequency dependent experiments, such as the mixing experiments discussed in Chapter 4, the ability to generate an acoustic signal with a narrow frequency spectrum was required. A Fabry-Perot etalon, often referred to in this work as the “cavity”, was constructed to produce a quasi-monochromatic acoustic signal.

Figure 3.2 illustrates the difference between a broad-frequency spectrum and a quasi-monochromatic spectrum. The quasi-monochromatic spectrum contains significantly fewer frequency components than the broad-frequency spectrum. It can not be defined as a single-frequency source, as the width is on the order of 1-2 GHz, but it is still significantly narrower than the broad-frequency spectrum generated by a single laser pulse, which has a width in the 10s of gigahertz range.

## Fabry-Perot etalon design

As described in section 2.1.1, when a single laser pulse directly excites a semiconductor or a thin metal film an acoustic wavepacket is generated that contains a broad spectrum of frequency components. To generate quasi-monochromatic acoustic signals for the mixing experiments a Fabry-Perot etalon was constructed and a schematic diagram of its operation is shown in figure 3.3. The initial laser pulse is aligned perpendicular to the mirrors, however to illustrate the multiple pulses it is clearer to draw the diagram with the reflections separated spatially.

A 95% reflectivity mirror and a 90% reflectivity mirror were mounted parallel to each other, separated by a distance  $d$ . A single pulse from the laser incident on the first cavity mirror is partially reflected multiple times between the cavity mirrors to generate a train of optical pulses with reducing amplitude. As one mirror is mounted on an adjustable translation stage the distance between the cavity mirrors, and hence the frequency of the pulses, can be adjusted.

The frequency of optical pulses generated by the cavity,  $f_0$ , is related to the cavity spacing,  $d$ , by the simple equation

$$f_0 = \frac{c}{2d} \quad (3.3)$$

where  $c$  is the speed of light.

The resulting comb of optical pulses incident on the GaAs sample generates a series of broad spectrum acoustic pulses separated by a time interval of  $\tau_0 = \frac{1}{f_0}$ . This leads to an acoustic signal modulated at the frequency of the optical pulses generated by the cavity. The spectrum of this acoustic signal is narrower than that of the individual acoustic pulses and centred around the frequency  $f_0$ . If an infinite train of pulses was produced, the width of the spectrum would be negligible. However, as only a finite number of optical pulses ( $\sim 10$ ) have the power required to generate an acoustic signal in the sample, the spectrum of the modulated signal must also have a finite width.

Several methods of generating narrow spectrum acoustic sources have previously been used in this frequency range. Non-tunable sources exist

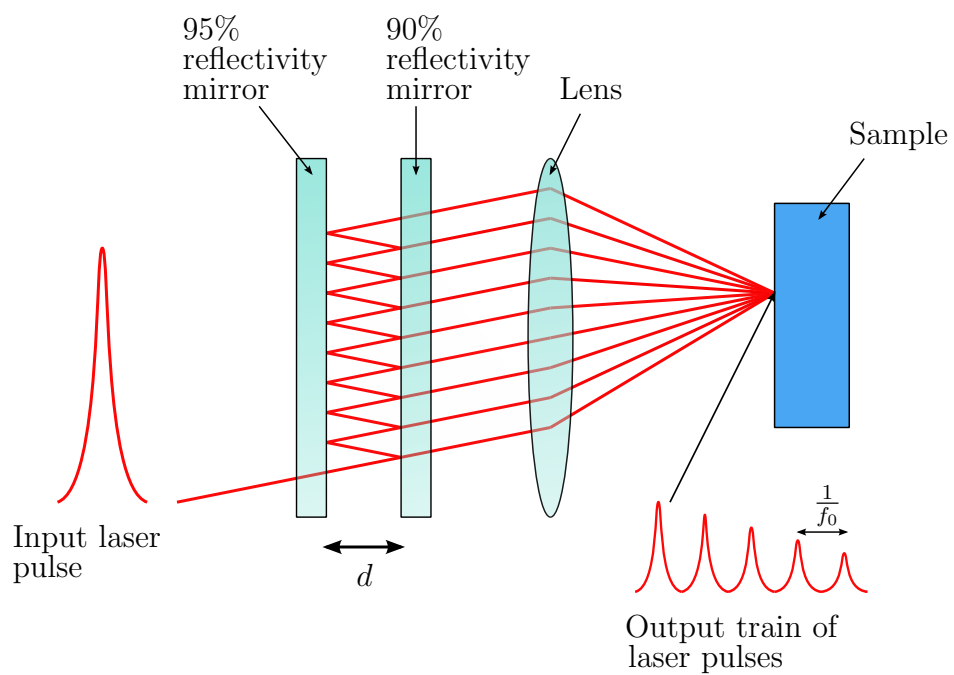


**Figure 3.3:** Illustration of the operation of the Fabry-Perot etalon. The Fabry-Perot etalon is constructed from two partially reflective mirrors. A single laser pulse incident on the cavity is partially reflected multiple times and partially transmitted, generating a series of pulses with decaying amplitude. The frequency of these pulses,  $f_0$ , is inversely proportional to the cavity spacing,  $d$ .

that are typically created by using fixed, layered structures. It has been demonstrated that semiconductor superlattices can be used for this purpose [49], as the high frequency folded modes in the dispersion relation allow the efficient coupling of light into high frequency coherent phonons. However, these structures must be grown onto the sample to be investigated, which is often not practical. Alternatively, external optical systems have been used, such as in the work by Herzog *et al.* [83] in which a series of glass layers alternated with spacers were used to generate multiple reflections of a single laser pulse. This can be reused for a range of samples, but the fixed frequency still limits the use of this system. A tunable, narrow frequency system in the gigahertz range has been demonstrated by Choi *et al.* [84]. This set-up used a retroreflecting system with a custom beam splitter of varying partial reflectivities to generate 7 optical pulses with a Gaussian intensity profile. This train of pulses could then be used to generate a quasi-monochromatic acoustic signal, tunable in the 2-2000 GHz range by the movement of a single translation stage. This type of system provides the most versatility, yet it is more complicated than this work requires so a simple two mirror set-up was sufficient.

### **Testing the Fabry-Perot etalon**

Optical pump-probe experiments were performed to test the function of the Fabry-Perot etalon, using the set-up shown schematically in figure 3.4. In pump-probe experiments the laser beam is split along two paths using a beam splitter. In this case, the “pump” beam incident on one face of the sample was used to generate an acoustic wavepacket in the sample. The “probe” beam path length was designed such that the probe pulse was incident on the far side of the sample at the same time as the acoustic signal reached it after propagation across the sample. Changes in the reflectivity of the surface, caused by the presence of the acoustic signal, were detected using a BPX65 photodiode in a home made differential photodiode circuit built by the electronics workshop in the School of Physics. By adjusting the length of the pump path, the acoustic signal at different times could be detected.

The laser system consisted of four different units, as shown in figure 3.4, and these were all made by Spectra-Physics. The Tsunami is a Ti:Sapphire

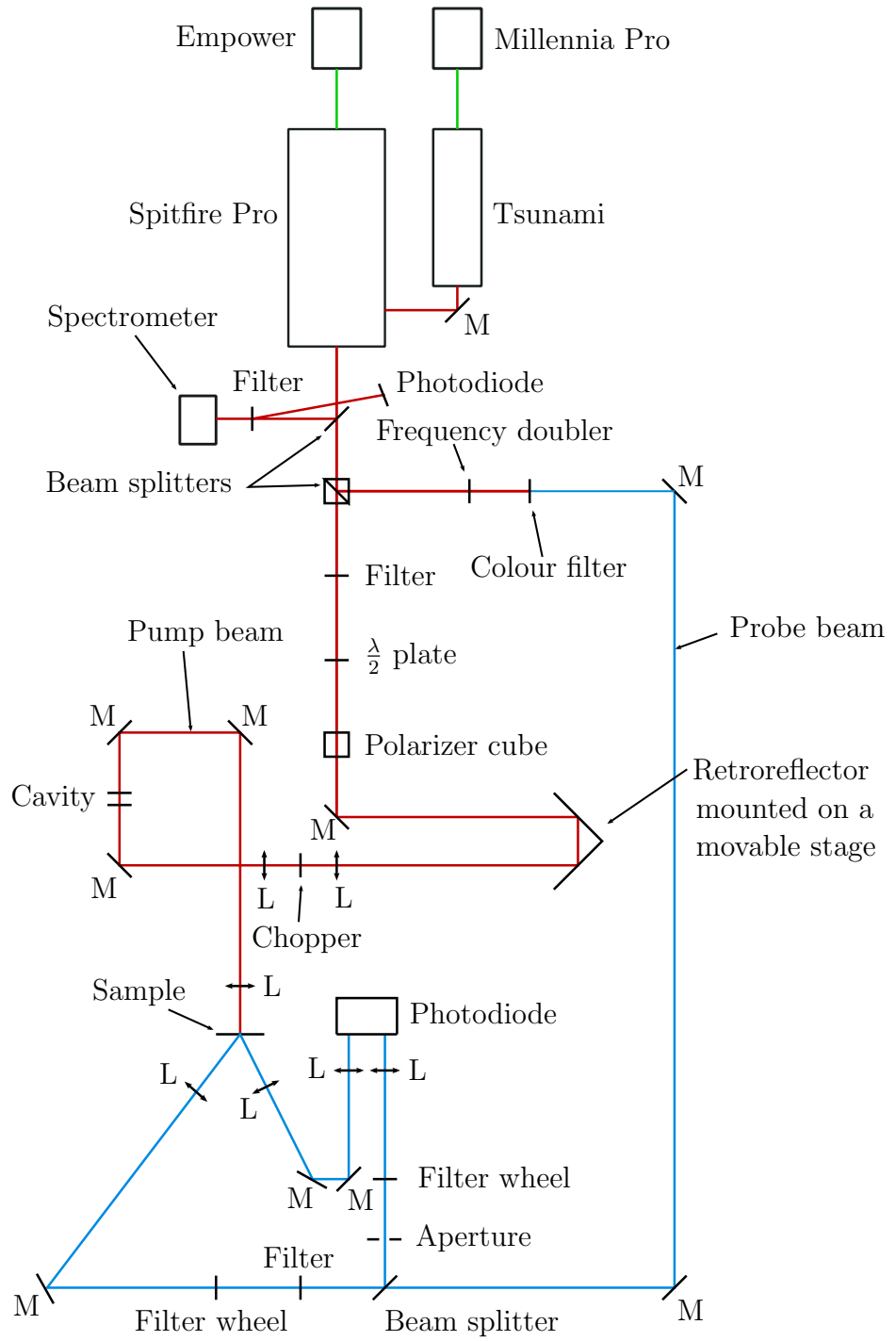


**Figure 3.4:** Set-up for pump-probe measurements to test the Fabry-Perot etalon. The laser beam is split into two to form the “pump” and “probe” beams. The pump beam passes through the Fabry-Perot etalon (cavity) to generate modulated acoustic signals in the sample. The pump path has variable length due to the movement of the retroreflector. The probe beam passes through a frequency doubler and is reflected from the far side of the sample onto a photodiode detector for reflectivity measurements. M denotes a mirror and L represents a lens.

laser that was used to produce the laser pulses. This was pumped using the Millennia Pro continuous wave laser. The output from the Tsunami was guided into the Spitfire Pro amplifier, which amplified the energy of the laser pulses from nanojoules to millijoules. The amplifier also required a pump laser, and the Empower was used for this purpose. The output laser pulses from the Spitfire Pro amplifier, with a wavelength of 800 nm, were then used to perform the experiments.

A small portion of the laser beam was directed onto a photodiode, and the photodiode was used to trigger the fast oscilloscope in experiments where it was required. Another small portion of the laser beam was directed towards a spectrometer that could be used to observe the width of the laser pulse. After this, the laser beam was then split into the two paths - the pump beam and the probe beam.

The pump beam contained filters to reduce the laser power, so as not to damage the sample. The  $\lambda/2$  plate could be altered to change the direction of the linear polarisation of the laser beam. This, coupled with the following polariser cube, provided variable attenuation of the laser beam. The 800 nm wavelength pump laser beam passed through the Fabry-Perot etalon before being focussed onto the GaAs sample with a lens. An acoustic signal was generated directly in the GaAs. This acoustic signal then propagated across the sample, which had a thickness of approximately 17  $\mu\text{m}$ .

The probe laser beam was passed through a frequency doubler to produce a wavelength of 400 nm, and the remaining components at 800 nm were removed using a colour filter. The probe beam was then aligned onto the opposite side of the GaAs sample such that the reflected beam was incident on a photodiode detector. It was this reflected beam that contained the information about the strain pulse in the sample. The retroreflector in the pump beam path allowed the difference between the two path lengths to be changed, so that the acoustic signal could be probed at different times.

Some of the optical components were included to facilitate the observation of small signal changes measured by the photodiode. The optical chopper was included to modulate the pump beam at a lower frequency than the laser repetition rate. The chopper frequency was then used as a reference frequency for a lock-in amplifier, so that changes in the detected

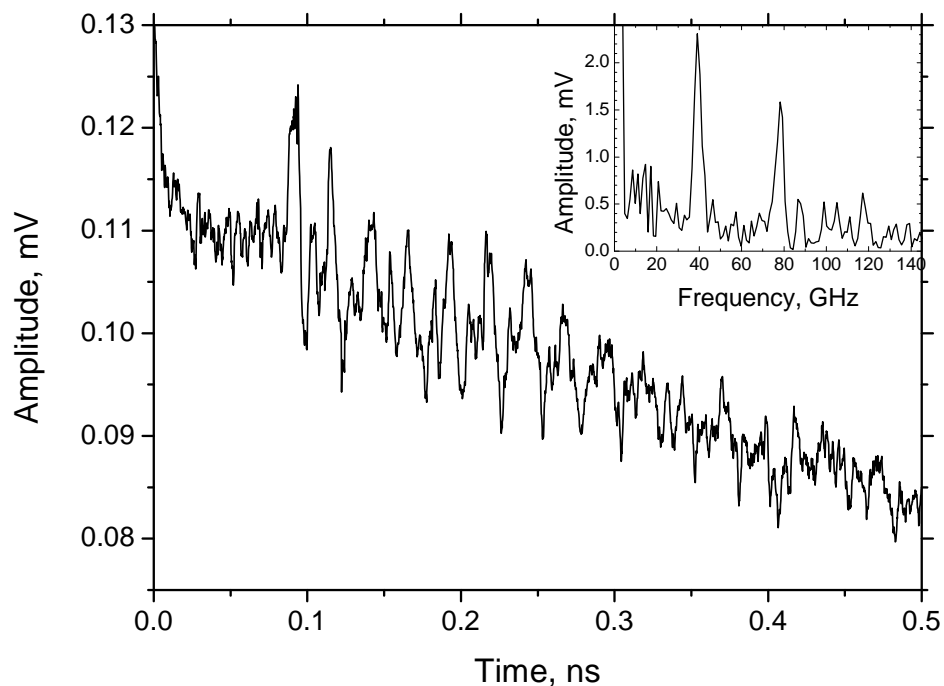


**Figure 3.5:** Optical pump-probe results of the Fabry-Perot cavity function at  $f_0 = 40$  GHz. Clear oscillations can be observed in the measured acoustic signal. The Fourier transform in the inset graph shows the presence of strong components generated at 40 GHz by the cavity, along with higher harmonics.

signal at the frequency of the chopper could be observed. By this method, only effects caused by the presence of the pump beam were included.

A beam splitter in the probe beam sent a portion of the probe beam, which had not been incident on the GaAs sample, to another photodiode detector. The two photodiodes were set up in a differential circuit, and this reduced the noise in the measurements by comparing the signals between the beam that had been reflected from the surface of the sample and the one that hadn't.

The cavity was tested for a range of spacing,  $d$ , to determine the spectral components of the acoustic signal generated in GaAs. The results for when the cavity was set to generate optical pulses at  $f_0 \approx 40$  GHz is shown in figure 3.5. There are clear oscillations present in the detected acoustic signal with a period of  $\approx 25$  ps. The Fourier transform of the signal is shown in the inset graph, which shows clear peaks at both 40 GHz and

80 GHz. A third peak is potentially present at 120 GHz, but the signal-to-noise ratio for this peak is poor. The presence of these peaks demonstrates that the cavity successfully modulates the acoustic signal at the desired frequency and that higher harmonics are generated in the acoustic signal too. Frequencies of up to at least 80 GHz, and possibly up to 120 GHz, are generated by this method and, therefore, the acoustic signal generated was suitable for use in the heterodyne mixing experiments.

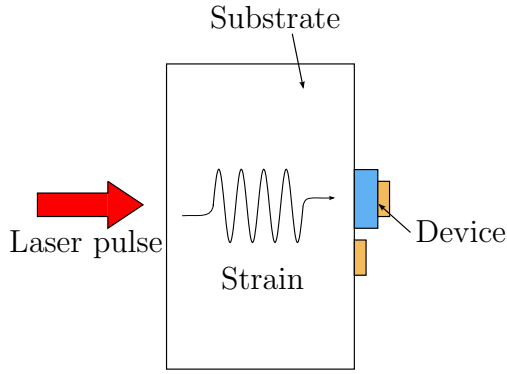
### **3.4 Fast electrical measurements**

To determine how devices respond electrically to a picosecond strain pulse it is necessary to have an oscilloscope with sufficient time resolution to capture the fast features in the signal. In this work a Tektronix DPO71254 12.5 GHz bandwidth real-time oscilloscope and a LeCroy WaveExpert 100 H sampling oscilloscope with a 30 GHz bandwidth sampling head and a 70 GHz bandwidth sampling head were used.

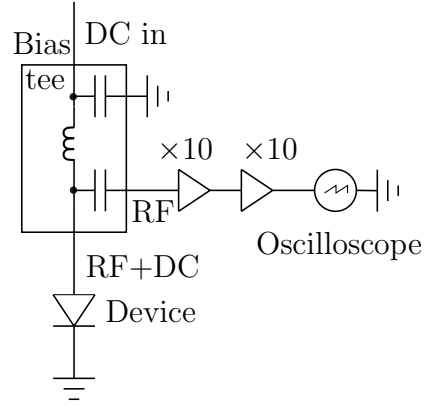
Acoustic signals were generated optically in the samples, as described in section 3.3. The acoustic wavepackets propagated across the sample to the device in use, such as a Schottky diode or a superlattice, as shown in figure 3.6a. The electrical set-up in figure 3.6b allowed the oscilloscope to measure the voltage across the device as a function of time. A bias tee was used to provide a DC bias to the device, while preventing the bias from reaching the oscilloscope. Two broadband 20 dB amplifiers (0.3 MHz - 14 GHz) could be included between the device and the oscilloscope to provide 10 times or 100 times amplification of small signals.

### **3.5 Measuring the microwave response of devices**

To determine if a sample would be suitable for use in the experiments to mix acoustic phonons with microwaves, it was necessary to know if the sample had a sufficient response to incident microwave radiation.



(a) Sample set-up for fast electrical measurements.



(b) Electrical set-up for fast electrical measurements.

**Figure 3.6:** Experimental set-up for fast electrical measurements. Laser pulses incident on the substrate side of the sample generated a strain pulse in the sample that propagated through the substrate to the device. The device was connected to the fast oscilloscope via a bias tee and two optional amplifiers.

Two different methods of coupling the microwave signal into the device were utilised. The initial method involved coupling the microwaves to the device from free space. For this, a bow-tie antenna was integrated into the sample design in the form of large metal contact pads. A 94 GHz Gunn diode oscillator provided by e2v was used in conjunction with a waveguide-fed horn antenna to launch the microwaves into free space. The microwaves propagated through free space and the glass cryostat windows before reaching the device to be detected.

A second method of coupling the 94 GHz signal directly into the device by waveguide was attempted with the e2v beam-lead Schottky diode. This method was significantly more effective at coupling the microwave power to the device. However, as it would be difficult to get a suitable waveguide into the continuous flow cryostat, this method was only appropriate for room temperature experiments.

To measure the microwave response of a device when the signal was small, a lock-in amplifier and an optical chopper were used, as shown in figure 3.7. For free space coupling of the microwaves, the chopper was positioned between the Gunn diode oscillator horn and the cryostat window

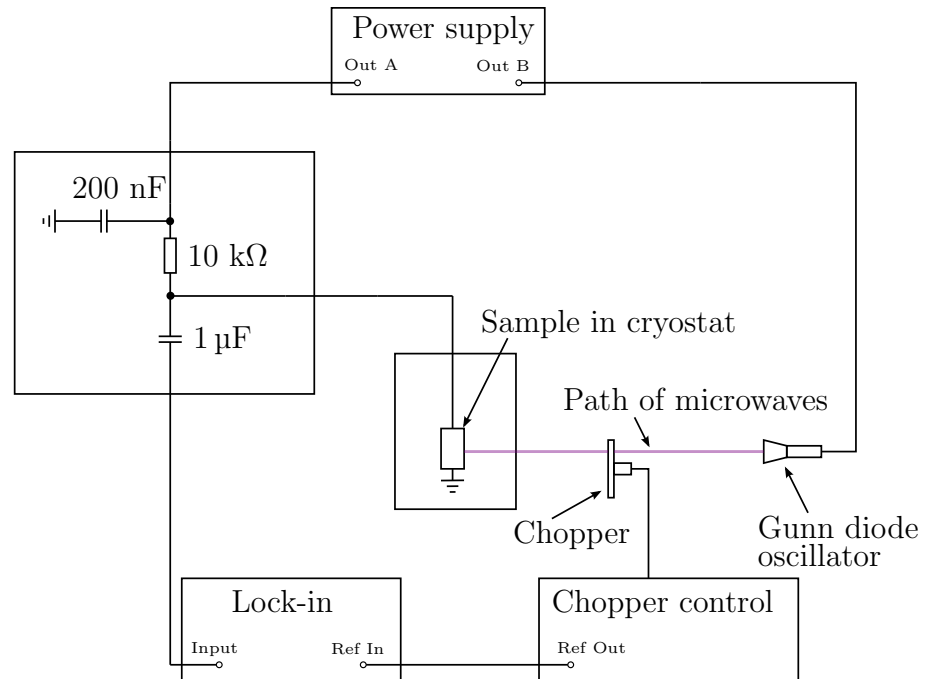


**Figure 3.7:** Experimental set-up to use a lock-in amplifier to measure the microwave response of a device. The microwaves produced by the Gunn diode oscillator were incident on the sample via free space. An optical chopper was used to modulated the microwaves at a known frequency that was used as the reference frequency for the lock-in amplifier. The lock-in amplifier detected electrical signals present that were modulated at the reference frequency.

to modulate the microwave signal by alternately blocking and not blocking its path. The frequency of the chopper provided the reference frequency for the lock-in amplifier. In this way, any changes in the DC component across the device due to the presence of the microwaves could be observed. The circuit containing a  $10\text{ k}\Omega$  resistor and two capacitors was used to create a constant current source for the device, and also to prevent the DC bias from reaching the lock-in amplifier.

For samples with a larger response to the incident microwaves the chopper and lock-in amplifier were not required. It was possible to simply observe the change in current through the device caused by the presence of microwaves as the Gunn diode oscillator was turned on and off. The I-V measurements described in section 3.2 could be used to measure the current as a function of applied bias to determine the effect of the microwaves at different applied biases.

## Chapter 4

# Heterodyne detection of optically-generated coherent acoustic waves using a Schottky diode

This chapter discusses heterodyne detection of optically generated acoustic waves using a Schottky diode. This technique would allow high frequency acoustic waves to be detected electrically with spectral resolution, ruling out the need for a picosecond laser as part of the detection process.

First, some background on the method of heterodyne mixing is presented. In heterodyne mixing, two signals with different frequencies are mixed to produce an output signal that contains new frequency components. This method can be used to convert high frequency signals to lower frequencies that can be processed more easily with currently available electronic instrumentation.

This is followed by an introduction to Schottky diodes, the intended mixer element. Some uses of Schottky diodes as mixers are discussed here, as they are commonly used as microwave mixer devices for multipliers and detectors. Schottky diodes have also been shown to detect picosecond acoustic signals (see section 2.3.2), suggesting that they are suitable for this purpose.

Experimental results presented in this chapter involve Schottky diode devices grown and fabricated in the School, and their response to acoustic and microwave signals. A beam-lead Schottky diode provided by e2v technologies was a more promising candidate as a mixer element due to its greatly improved response to incident microwaves. The first results of heterodyne mixing of microwaves with optically-generated acoustic waves are presented along with a discussion of the mechanism.

## 4.1 Heterodyne mixing

Heterodyne mixing is a common technique used to generate new frequencies by combining two signals that have different frequencies. To achieve this, the mixer element must have strong non-linear characteristics. Some examples of commonly used non-linear mixers include Schottky diodes [85], bipolar transistors, field effect transistors [86], hot electron bolometers and Josephson junctions [87, 88]. This method of combining signals generates frequencies, amongst others, which are the sum of the two input frequencies and the difference of the two. In general, only one of these frequencies is required and the other frequency components present are removed with filters.

The presence of the sum and difference frequency terms in the output signal can be demonstrated simply as follows [89]. Assume that the current-voltage characteristics of the non-linear mixer element can be expanded as a power series

$$I = a_1V + a_2V^2 + \dots \quad (4.1)$$

where  $I$  is the current,  $V$  is the voltage, and  $a_{1,2}$  are constants. The higher terms in the expansion are omitted for simplicity.

Assume that two sinusoidal signals with different frequencies are applied to the mixer element. The total voltage across the mixer element is the sum of the two applied voltages

$$V = V_1\sin\omega_1t + V_2\sin\omega_2t \quad (4.2)$$

where  $V_{1,2}$  are peak voltage amplitudes,  $\omega_{1,2}$  are two different angular frequencies and  $t$  is time. The current is found by substituting equation 4.2

into equation 4.1 and expanding to get

$$I = a_1 V_1 \sin \omega_1 t + a_1 V_2 \sin \omega_2 t + a_2 V_1^2 \sin^2 \omega_1 t + a_2 V_2^2 \sin^2 \omega_2 t + 2a_2 V_1 V_2 \sin \omega_1 t \sin \omega_2 t \quad (4.3)$$

This can be rewritten using trigonometric identities and rearranged to give

$$I = \frac{a_2}{2}(V_1^2 + V_2^2) + a_1(V_1 \sin \omega_1 t + V_2 \sin \omega_2 t) - \frac{a_2}{2}(V_1^2 \cos 2\omega_1 t + V_2^2 \cos 2\omega_2 t) + a_2 V_1 V_2 \cos(\omega_1 - \omega_2)t - a_2 V_1 V_2 \cos(\omega_1 + \omega_2)t \quad (4.4)$$

The first term in equation 4.4 is a direct current, while the second term contains the frequencies present in the initial signal. The third term contains second harmonics of the input frequencies, and higher harmonics would also be present if terms with higher powers of  $V$  were included in equation 4.1. This demonstrates that non-linear mixer elements can be used to generate higher harmonics of an input signal. This effect is commonly used in frequency multipliers to generate high frequency signals [90]. The last two terms contain frequencies that are the sum and the difference of the two initial frequencies, and it is the difference frequency that is of interest in this work.

In many heterodyne mixing applications an incoming signal is mixed with a local oscillator of a known, fixed frequency to generate a signal known as the “intermediate frequency”. It is the intermediate frequency signal that contains new frequency components and is further processed with filters and amplifiers. As the local oscillator has a known frequency, the frequency of the incoming signal can be obtained from the intermediate frequency.

Heterodyne mixing is commonly used in microwave communications, as most modern receivers will employ heterodyne mixing as a method to reduce the transmitted signal to a lower frequency signal that is easier to amplify and further process [86]. Heterodyne mixers are also used in sensors at microwave frequencies for a variety of applications such as space missions, earth sensing [90], fusion plasma diagnostics [88] and radar [91, 92].

For the experiments presented in this chapter, a 94 GHz Gunn diode oscillator was used as the local oscillator and the frequency of the incident

acoustic signal could be varied. The lower frequency component produced during the mixing process was required as in this way, the high frequency signal could be mixed to a frequency band that was within the bandwidth of the oscilloscope.

## 4.2 Schottky diodes

### 4.2.1 General background

A Schottky diode is a metal-semiconductor junction that creates a potential barrier at the interface [93], as demonstrated in figure 4.1. Consider the case where  $e\phi_m > e\phi_s$  for an  $n$ -type semiconductor [94], where the work function  $e\phi_{m,s}$  is the energy required to remove an electron from the Fermi level of the metal ( $E_{Fm}$ ) or the semiconductor ( $E_{Fs}$ ), respectively, to the vacuum level. As the metal and semiconductor are brought together, charge must be transferred so that the Fermi levels align at thermal equilibrium ( $E_F$ ). Electrons from the  $n$ -type semiconductor conduction band ( $E_C$ ) diffuse into the metal, leaving behind positively charged donor ions. The Fermi level in the semiconductor is lowered by an amount  $eV_0 = e(\phi_m - \phi_s)$ , where  $V_0$  is the equilibrium contact potential. This potential, and the associated electric field, prevents further electrons from diffusing into the metal. Another potential barrier, with height  $e\phi_B = e(\phi_m - \chi)$  stops electron injection from the metal to the semiconductor. Here the electron affinity,  $e\chi$ , is the energy required to remove an electron from the bottom of the conduction band of the semiconductor to the vacuum level. A depletion region,  $W_d$ , is formed in the semiconductor by the presence of the positively charged donor ions. The built-in electric field occurs across this region, along with an associated voltage drop. The width of the depletion region can be calculated from the Poisson equation [93] as

$$W_d = \sqrt{\frac{2\epsilon_r\epsilon_0}{eN_D} \left( V_0 - V - \frac{k_B T}{e} \right)} \quad (4.5)$$

where  $\epsilon_r$  is the relative permittivity of the semiconductor,  $\epsilon_0$  is the permittivity of free space,  $e$  is the charge of an electron,  $N_D$  is the donor concentration of the  $n$ -doped semiconductor,  $V$  is the external bias applied

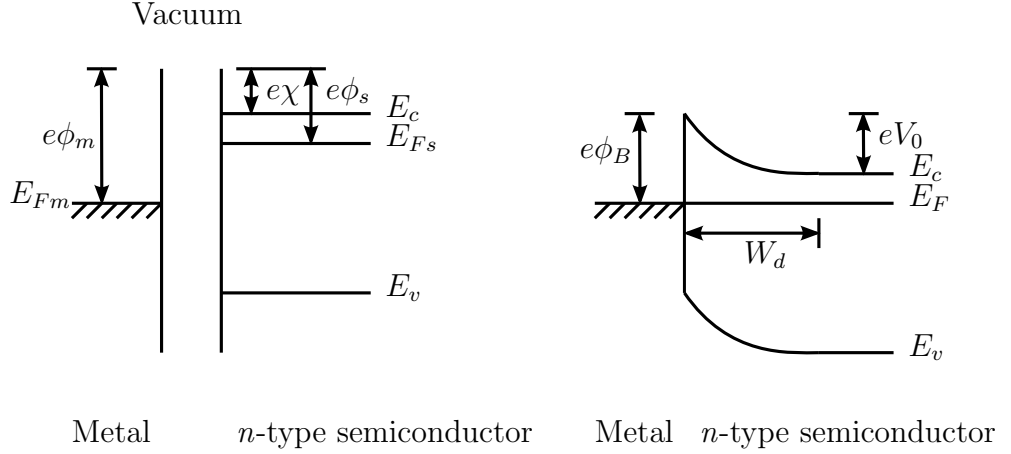


**Figure 4.1:** Energy band diagrams of an  $n$ -type Schottky diode with  $e\phi_m > e\phi_s$ , where  $e\phi_{m,s}$  is the work function of the metal or semiconductor, respectively. When the metal and the semiconductor are brought into contact the Fermi levels must align at thermal equilibrium. This leads to bending of the energy bands in the semiconductor by an amount  $eV_0$ , the formation of a potential barrier  $e\phi_B$  and the formation of a depletion region  $W_d$ .  $E_{Fm,s}$  are the Fermi levels in the metal and the semiconductor when separate, whereas  $E_F$  is the Fermi level of the Schottky diode at equilibrium.  $E_{C,V}$  are the conduction and valence bands in the semiconductor and  $q\chi$  is the electron affinity of the semiconductor.

to the Schottky diode,  $k_B$  is the Boltzmann constant and  $T$  is the temperature. As such, the depletion width for any given Schottky junction is dependent on the applied bias.

When a forward bias voltage  $V_f$  is applied to the Schottky barrier, defined as a positive bias being applied to the metal, the contact potential is reduced from  $V_0$  to  $(V_0 - V_f)$  as shown in figure 4.2. A reduction in the contact potential allows more electrons from the semiconductor conduction band to diffuse into the metal causing a forward current to flow. When a reverse bias voltage  $V_r$  is applied, the contact potential is increased to  $(V_0 + V_r)$  and the electron flow from the semiconductor to the metal is reduced. As the potential barrier for the flow of electrons from the metal to the semiconductor is independent of applied bias, it is possible to increase current flow in the forward direction but not the reverse direction and the junction behaves as a rectifier. For an ideal Schottky diode the relationship between the current flowing through the device,  $I$ , and the applied bias,

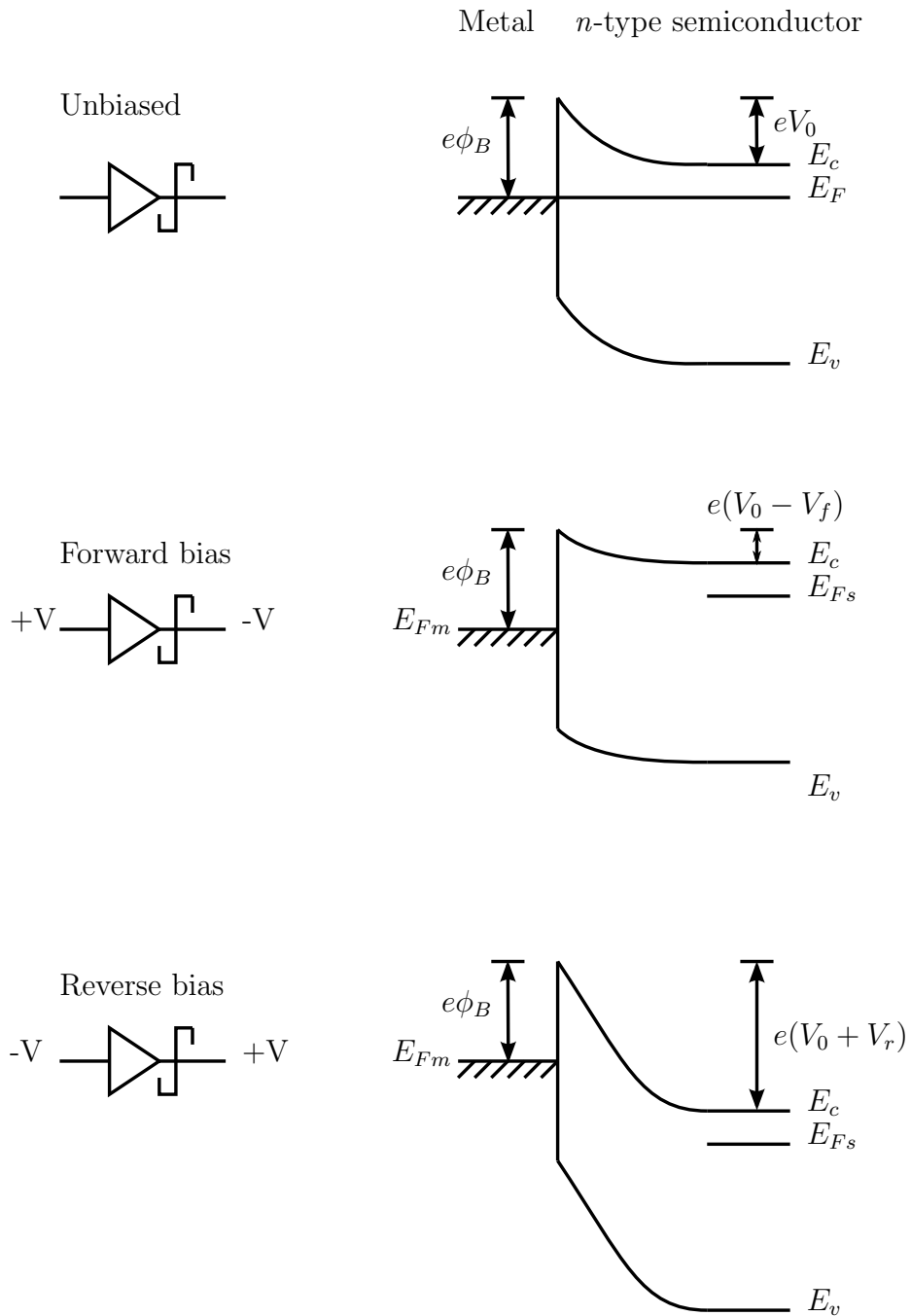


**Figure 4.2:** Energy band diagrams of an  $n$ -type Schottky diode under different biasing conditions. A bias applied across the Schottky diode changes the size of the contact potential and so changes the amount of electrons that are able to diffuse from the semiconductor into the metal.

$V$ , is given by the equation

$$I = I_S(e^{eV/k_B T} - 1) \quad (4.6)$$

where  $I_S$  is the reverse saturation current [93]. The non-linearity of the current-voltage relationship allows Schottky diodes to be utilised as non-linear mixer elements.

To create a Schottky diode from a  $p$ -type semiconductor it is necessary that  $\phi_m < \phi_s$ . To align the Fermi levels at equilibrium, holes flow from the semiconductor to the metal, creating a positive charge on the metal side and a negative charge in the semiconductor. The depletion region is now caused by the presence of negative acceptor ions in the  $p$ -type semiconductor. The potential barrier that stops holes from diffusing from the semiconductor into the metal is given by  $eV_0 = e(\phi_s - \phi_m)$ . As with the  $n$ -type Schottky diode, the application of bias across the Schottky junction changes the potential barrier height, varying the current that can flow through the device.

The two other types of ideal metal-semiconductor junction do not produce rectifying contacts, that is for  $n$ -type semiconductors with  $\phi_m < \phi_s$  and for  $p$ -type semiconductors with  $\phi_m > \phi_s$ . To align the Fermi levels in these junctions majority carriers are injected from the metal to the semiconductor. The potential barrier that forms for current flow from the metal to the semiconductor is small and only a small voltage is required to cause current to flow in either direction through the junction. No depletion region occurs in the semiconductor as majority carriers are accumulated in the semiconductor to align the Fermi levels. As these junctions do not rectify currents they can be used to form ohmic contacts.

The discussion on Schottky diodes so far has been limited to the ideal case. In reality, there are several reasons why Schottky diodes do not follow this ideal. One effect is due to the finite size of the semiconductor crystal. The edge of the semiconductor crystal contains surface states, for example due to incomplete covalent bonds, and these states can trap charges at the metal-semiconductor interface. Another contribution is from a thin interfacial layer between the semiconductor and the metal, as native oxides can form rapidly on the semiconductor surface prior to metal deposition. Carriers are able to tunnel through the thin interfacial layer, however it does

have an effect on the potential barrier. Furthermore, in some compound semiconductors such as GaAs, the presence of the interfacial layer causes states to be present in the semiconductor band gap. These states pin the Fermi level at a fixed position. In this case the barrier height is independent of the metal used to form the contact, as it is the pinned states that determine the barrier height instead of the work function of the metal [94].

The relationship between the current flowing through a Schottky diode and the applied bias given in equation 4.6 was for the case of an ideal metal-semiconductor junction. In the case of realistic diodes this relationship can deviate from the ideal behaviour. An ideality factor  $\alpha$  is then included to account for this, and the expression becomes

$$I = I_S(e^{eV/\alpha k_B T} - 1) \quad (4.7)$$

where the ideality factor,  $\alpha$ , can have a value between 1 and 2 [93]. For an ideal diode  $\alpha = 1$  and equation 4.7 becomes identical to equation 4.6. There are several mechanisms that can cause the deviation from the ideal case, but the main one is the generation and recombination of carriers in the depletion layer. In general the ideality factor is larger for  $p$ - $n$  diodes, those formed with a layer of  $n$ -doped material and a layer of  $p$ -doped material, as these effects are much greater. For Schottky diodes it is typical for the ideality factor to be closer to 1.

Schottky diodes are known as “majority carrier devices” as forward current flow through the device is due to majority carriers from the semiconductor being injected into the metal. Injection of majority carriers is faster than that of minority carriers, so these types of device are often chosen for fast switching speeds and therefore high frequency applications [94].

## 4.2.2 Schottky diodes used as microwave mixers

Schottky diodes have been used extensively as multipliers and mixers for electromagnetic signals up to the terahertz range. They find uses in a wide range of research fields such as astrophysics, atmospheric and planetary monitoring applications [90] and plasma diagnostics in nuclear fusion research [88]. Schottky diode detectors have been used on several space missions, including the Herschel Space Observatory and the Rosetta mis-

sion. A significant advantage of Schottky diodes over alternative mixer elements such as superconductor-insulator-superconductor junctions and hot electron bolometers is the ability to use them at ambient temperature. This avoids the expense, size and weight associated with cooling the mixer to cryogenic temperatures, which is often critical on space missions and satellites. Planar Schottky diodes are also compact and mechanically robust, while being relatively simple to integrate into larger sub-systems.

Schottky diodes are used in both frequency multipliers and mixers in this frequency range. It can be difficult to generate local oscillator signals at the desired frequencies, so frequency multipliers are used to achieve high frequencies by generating the higher harmonics of a microwave source such as a Gunn diode oscillator [90]. Heterodyne mixers are used to down-convert incoming signals to frequency bands that can be easily processed.

### **4.3 Preliminary work on Schottky diodes detecting acoustic and microwave signals**

Two sets of planar Schottky diode devices were fabricated from wafers grown within the University of Nottingham by molecular beam epitaxy (MBE). These were tested for their ability to detect both acoustic and microwave signals. The two sets of devices produced qualitatively similar results; the Schottky diodes successfully detected acoustic signals but had a poor response to incident microwaves.

#### **4.3.1 Device structures**

##### **Mn659 structure**

The Mn659 sample comprised of a single 300 nm thick layer of  $n$ -doped GaAs ( $n = 2 \times 10^{17} \text{ cm}^{-3}$ ) grown by MBE on a semi-insulating GaAs substrate, as shown schematically in figure 4.3. This layer was fabricated into one mesa per device, shaped like a triangle with one rounded point, as shown in the microscope image in figure 4.4. A large trapezium-shaped

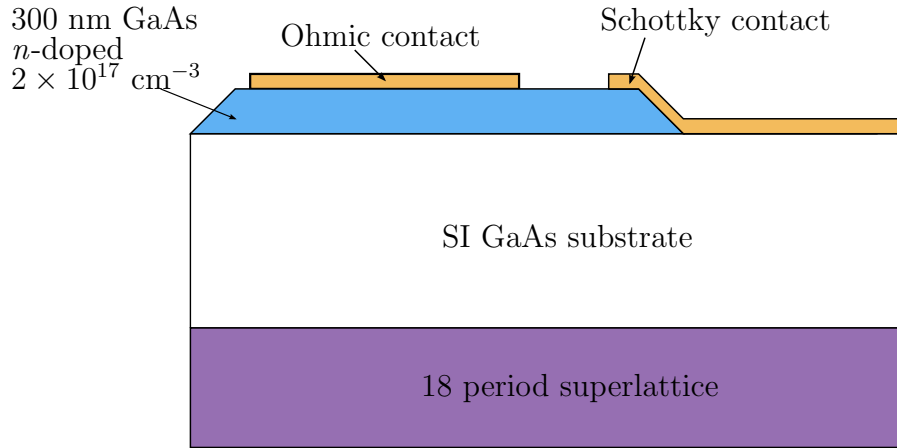


**Figure 4.3:** Schematic diagram of a Schottky diode fabricated from the Mn659 wafer. Mesas were etched from the  $n$ -doped GaAs layer. An annealed ohmic contact and an abrupt Schottky contact were both formed on the top of the mesa. The undoped 18 period GaAs/AlAs superlattice on the back of the substrate was protected during processing.

ohmic contact was made on top of each mesa and a small Schottky contact was formed on the mesa at the curved end. The Schottky contact was connected to a large truncated triangular metal pad to form the second half of a bow-tie antenna, intended to couple in incident microwaves. A superlattice was grown on the reverse of the sample, which was included to act as a filter for acoustic frequencies generated at the back face of the sample, to aid in producing a quasi-monochromatic acoustic signal for mixing experiments. The superlattice was undoped, with 18 periods of 49 nm AlAs barriers and 13 nm GaAs wells. This superlattice was protected with photoresist during processing to maintain a good quality surface for optical generation of coherent phonons in later experiments.

### Mn744 structure

To make improvements to the Mn659 structure, a new sample was grown by MBE and a new mask was designed to alter the fabrication process. A schematic diagram of the Schottky diodes fabricated from Mn744 is shown in figure 4.5. Two doped layers were grown on a semi-insulating GaAs substrate. Initially 500 nm of  $n$ -doped GaAs ( $n = 5 \times 10^{18} \text{ cm}^{-3}$ ) was grown onto the substrate, as the higher doping concentration allows for the formation of a good ohmic contact. The second layer of 100 nm of

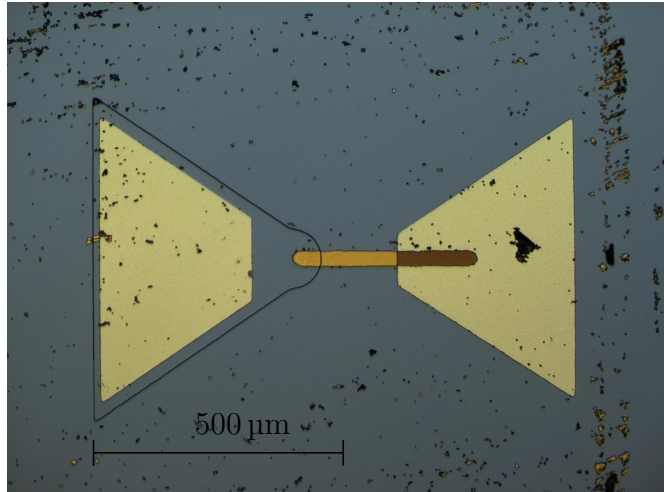


**Figure 4.4:** Microscope image of a Schottky diode fabricated from the Mn659 wafer. The mesa is visible as a black outline on the left-hand side of the image with the small Schottky contact and larger annealed contact formed on top of the mesa. The right-hand part of the antenna is deposited on the semi-insulating GaAs substrate.

$n$ -doped GaAs ( $n = 5 \times 10^{17} \text{ cm}^{-3}$ ) had a lower doping concentration for the formation of the Schottky contact. In this structure the superlattice used in the previous Mn659 sample was omitted for simplicity during the initial characterisation of the devices.

The devices were formed by etching through both doped layers to create one triangular mesa per device, in a similar method to the Mn659 devices and shown schematically in figure 4.5. In this new structure, most of the top layer was removed from each mesa to allow the ohmic contact to be formed to the layer with higher doping concentration. A  $\text{SiO}_x$  dielectric layer was deposited in a thin film by thermal evaporation to electrically insulate the etched side of the mesa before the Schottky contact and associated triangular bonding pad were deposited. The mask was designed such that Schottky contacts of 4 different diameters were created:  $10 \mu\text{m}$ ,  $30 \mu\text{m}$ ,  $60 \mu\text{m}$  and  $100 \mu\text{m}$ . This was to allow the fabrication of devices with a range of capacitances. A microscope image of a completed device is shown in figure 4.6. The left-hand contact is the ohmic contact on top of the mesa. The circular contact is the Schottky contact and the green area is the  $\text{SiO}_x$  insulating layer.

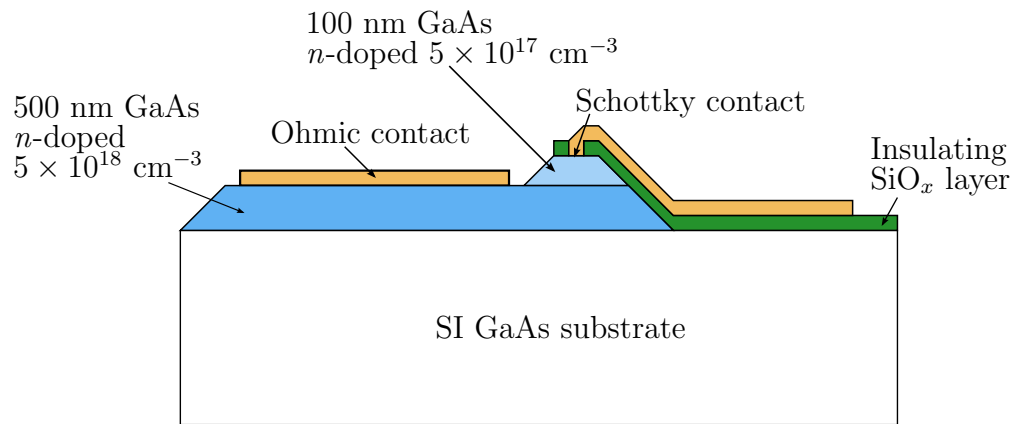


**Figure 4.5:** Schematic diagram of a Schottky diode fabricated from the Mn744 wafer. Mesas were etched such that an ohmic contact could be made to the higher doped  $n$ -layer and a Schottky contact could be made to the lower doped  $n$ -layer. A  $\text{SiO}_x$  layer was deposited to insulate the edge of the mesas and the contacts were fabricated as bow-tie antenna to couple in incident microwaves.

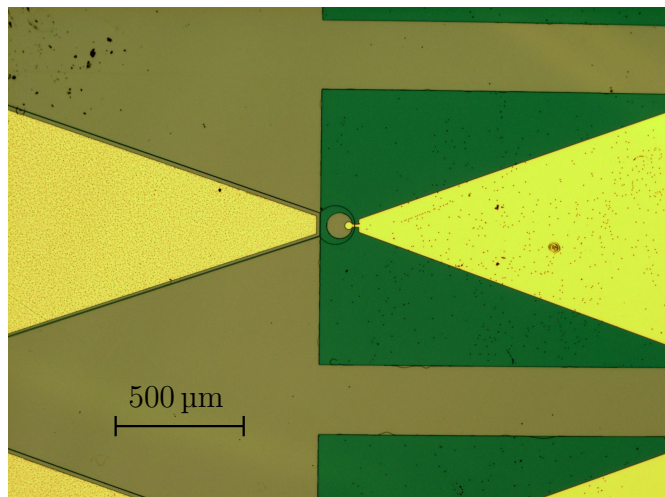


**Figure 4.6:** Microscope image of a Schottky diode fabricated from the Mn744 wafer. The left-hand part of the bow-tie antenna is the ohmic contact and the  $30\ \mu\text{m}$  diameter Schottky contact is the circular area attached to the right-hand part of the bow-tie antenna. The green coloured rectangle is the  $\text{SiO}_x$  insulating layer.

### 4.3.2 Device characterisation

The current-voltage (I-V) characteristics of the Schottky diodes fabricated from the Mn659 and Mn744 wafers were investigated by applying a voltage to the device and measuring the voltage drop across a series resistor to determine the current. These measurements were taken in a continuous flow cryostat at a temperature of 4 K as later experiments required the low temperature to reduce the scattering of acoustic phonons caused by thermal phonons. The results of the I-V measurements are shown in figure 4.7.

The Mn659 device has a turn on voltage of  $\approx 0.7$  V and a series resistance of  $175 \Omega$ . The Mn744 device turns on at  $\approx 0.6$  V and has a series resistance of  $37 \Omega$ . The lower resistance for the Mn744 devices is likely to be due to the improved ohmic contact. The reverse breakdown voltage differs most between the two diodes. The Mn659 device has a reverse breakdown voltage of  $\approx -5$  V, while the Mn744 diode is much more leaky, with a reverse breakdown at  $\approx -2$  V. This is in part probably due to the reduced resistance of the device, while the different doping of the *n*-doped semiconductor used to form the Schottky barrier and a difference in the fabrication method could have made a change to the barrier height. Interface states can have a big effect on the characteristics of a Schottky junction, and these states can vary greatly with surface preparation [95]. With mixing experiments performed in forward bias, the reduced reverse breakdown of the Mn744 devices compared to the previous devices should have little effect on the device's ability to perform as a mixer element.

Devices fabricated from both wafers demonstrate a strongly non-linear relationship between the current and the voltage, which is required for mixing. The turn-on point in the forward bias regime has the most pronounced non-linear feature in the characteristics shown in figure 4.7, and so gives the best region of operation of these diodes for potentially observing mixing.

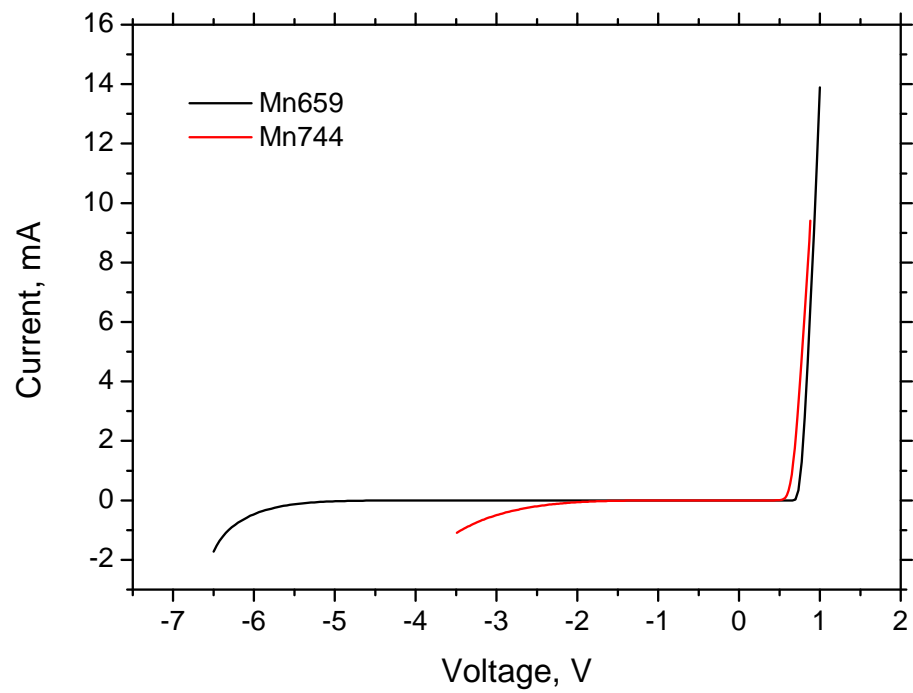


**Figure 4.7:** I-V characteristics of Schottky diodes fabricated from wafers Mn659 and Mn744. Both devices display strongly non-linear characteristics, which are essential for mixer elements.

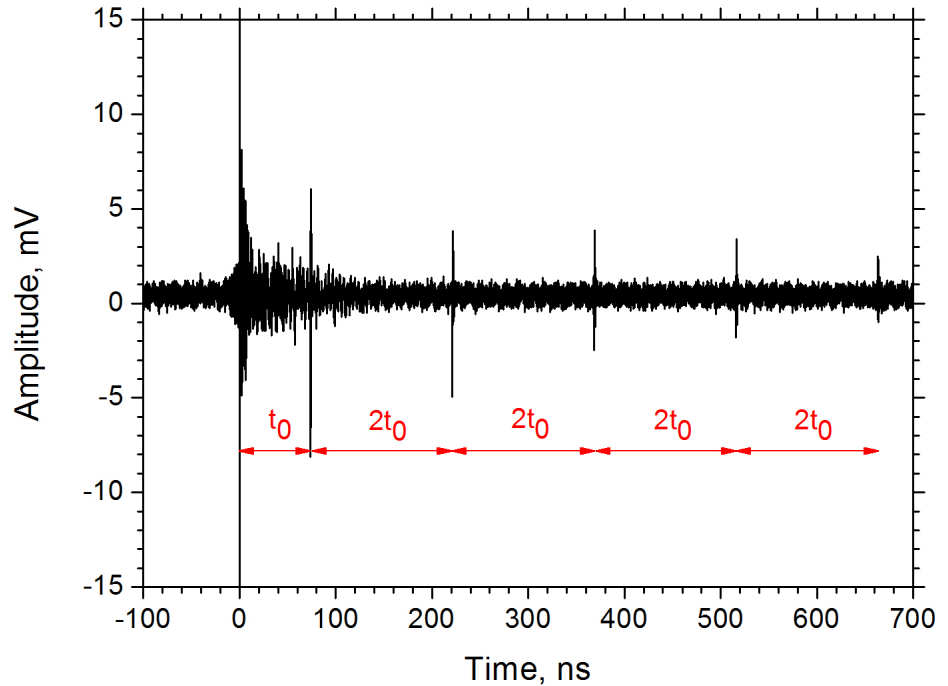


**Figure 4.8:** Acoustic signal detected by a Schottky diode fabricated from the Mn744 wafer. The initial peak is the optical breakthrough, while the later peaks are acoustic signals. Multiple peaks are observed due to reflections within the sample.

### 4.3.3 Detecting acoustic signals

To test the response of both sets of Schottky diode to incident acoustic signals, the samples were mounted in an optical access flow cryostat and cooled to a temperature of 4 K. A pulsed femtosecond laser was used to generate acoustic signals in an Al film thermally evaporated onto the back of the substrate of the samples. The acoustic signal propagated across the substrate of the sample to the Schottky diode. Changes in the voltage across the device caused by the presence of the strain pulse were measured by a fast oscilloscope as described in section 3.4.

The devices fabricated from the two different wafers behaved in qualitatively the same way, so results for only the Mn744 sample are presented here. The main difference between the acoustic signals detected in the two samples was the arrival time  $t_0$  of the acoustic signal at the Schottky diode

and this was due to the difference in thickness of the two samples. The magnitudes of the detected signals for the two devices were very similar. This is not surprising, based on the I-V characteristics. The resistances of the two types of device were a little different, but largely the devices could be expected to behave in the same way.

The acoustic signal detected by the Mn744 Schottky diode is shown in figure 4.8. The initial peak is the optical breakthrough, caused by the Schottky diode responding directly to the laser pulse. The peak at time  $t_0 = 73.7$  ns later than the initial optical response is the first acoustic signal after propagation across the substrate of the sample. With longitudinal sound velocity in GaAs  $v_{GaAs} = 4780$  ms<sup>-1</sup> [68], this time corresponds to an acoustic pulse crossing a thickness of approximately 352  $\mu$ m of GaAs. The following peaks are separated in time by  $2t_0$  intervals and this is due to the acoustic wavepacket reflecting from the sample/air interfaces at the top of the device and the back of the substrate to be detected again by the Schottky diode. These reflections are expected and have been observed in previous work [47].

To investigate the bias dependence of the acoustic signal a range of DC voltages were applied to the Schottky diode via a bias tee, and the voltage across the Schottky diode was recorded on a fast oscilloscope. The results for the Mn744 sample with negative applied bias are shown in figure 4.9. The shape of the detected acoustic signal is complicated due to the structure of the Mn744 device containing several layers, as shown schematically (and not to scale) in figure 4.5. However, it is clear that there is little change to the timing of the detected signal with applied bias, suggesting that the strain-sensitive region of the device is fixed in position.

This is different to the previous work by Moss *et al.* in which they observed a definite shift in time of the peaks in the acoustic signal due to the applied negative bias [47]. The observed signal was simpler, due to the reduced complexity of the Schottky diode device. The observed shift in time of the acoustic signal was  $\approx 40$  ps at -5 V applied bias, with the initial part of the signal arriving earlier for larger applied negative bias and the later part of the signal, that which had reflected back to the device from the top surface of the sample, arriving later. This shift in time was attributed to the change in width of the depletion region with applied bias, as given

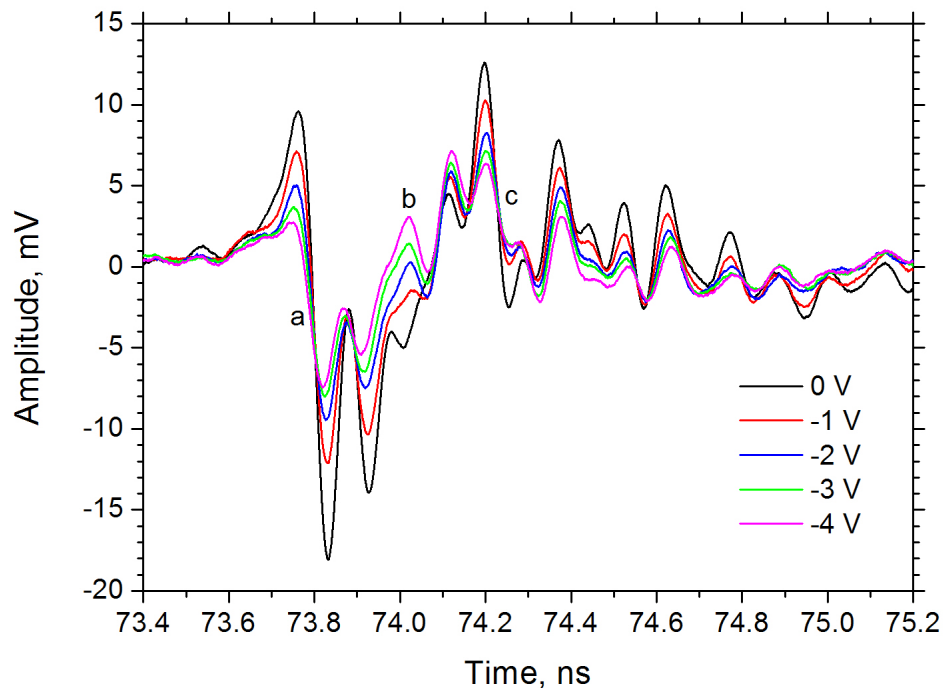


**Figure 4.9:** Bias dependence of the temporal response of the Mn744 Schottky diode for a range of applied negative bias. The shape is complicated, containing many peaks due to the complicated structure of the device with multiple reflections of the acoustic pulse from different layers. Electrical ringing is also present after the initial strain pulse. Applying a larger bias reduces the magnitude of the acoustic signal but has little effect on the shape or timing.

in equation 4.5. This lead to the conclusion that the main contribution to the acoustic signal measured in the work by Moss *et al.* was from the depletion region edge.

The Mn744 device discussed in this thesis is potentially detecting acoustic signals at two distinct fixed boundaries. The acoustic wavepacket propagating across the substrate initially encounters the boundary between the two different  $n$ -doped GaAs layers. These have an order of magnitude difference in the nominal doping concentration, leading to a step change in the carrier concentration between the two layers. Second, the acoustic wavepacket encounters the semiconductor-metal interface of the Schottky diode itself. These boundaries are separated by only 100 nm of GaAs. Using  $v_{GaAs} = 4780 \text{ ms}^{-1}$  [68] the time for the acoustic signal to travel

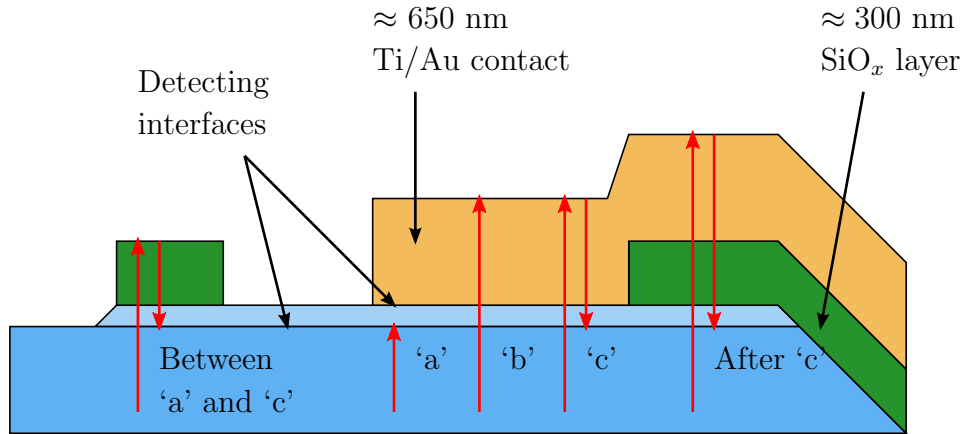


**Figure 4.10:** Layers in the Mn744 structure that lead to reflections of the acoustic wavepacket and the features observed in figure 4.9. The first response ‘a’ occurs as the wavepacket travels towards the surface of the sample. Reflections from different layers lead to further features in the signal.

100 nm in GaAs is only 21 ps. The difference in time is sufficiently small that it is likely that the measurement system cannot resolve separate peaks from these two interfaces and they are combined in the initial part of the response seen at 73.7 ns in figure 4.9. Any change in the signal due to the movement of the depletion region edge would be small, as it could only vary by 100 nm before the top layer with the lower doping concentration became fully depleted. This effect cannot be significant in this sample.

The proposed mechanism for detection is still the deformation potential as in the work by Moss *et al.* [47]. The presence of strain in the semiconductor material causes a change to the lattice spacing and hence also changes the band energies of the semiconductor. In a region of non-uniform charge density the carriers redistribute spatially to screen the perturbation and this leads to a transient current in the Schottky diode.

After the acoustic wavepacket has reached the top of the GaAs layer, it will continue to propagate to the top of the device through the different materials deposited on the GaAs as shown in figure 4.10. The area around the Schottky contact has been coated with a dielectric layer, while the Schottky contact itself is formed of a thicker layer of Ti/Au. Thus, there are at least two possible times for the acoustic signal to reach the top of the device and reflect back towards the detecting interfaces.

The features around point ‘c’ in figure 4.9 are likely to be the reflection of the initial signal at point ‘a’, after the acoustic wavepacket has reached the top of the Au contact and been reflected back to the detecting region with a  $\pi$  phase shift. Using the speed of longitudinal sound in Au  $v_{Au} = 3360 \text{ ms}^{-1}$  [2], this time corresponds to a thickness of 650 nm of Au. During the Au deposition the target thickness was  $>500 \text{ nm}$ . As the deposition rate was not accurately calibrated, it is reasonable to assume that the thickness of the Ti/Au contact is indeed 650 nm.

For good electrical contact between the Schottky contact and its associated triangular bond pad, it was necessary that the metal contact layer was thicker than the dielectric layer, which was estimated to be in the region of 300 nm thick. As the dielectric film is thinner than the metal layer and the acoustic velocity is higher in the dielectric [2, 96], the acoustic reflections from the top of the dielectric layer would arrive back at the detecting region earlier than those from the top of the Au layer, and account for some of the structure seen between points ‘a’ and ‘c’. Due to the processing methods, there is also a region in which the metal layer was deposited over the top of the dielectric. This region will contribute to some of the structure observed after point ‘c’, along with any multiple reflections between the various layers.

An intriguing effect is seen at point ‘b’, in which there appears to be a change in sign in the signal between the zero bias trace and those with negative applied bias. None of the other peaks exhibit this behaviour. The timing of this feature at point ‘b’ is exactly half way between points ‘a’ and ‘c’, suggesting that this is due to the strain pulse reaching the free surface of the Au. It is possible that the surface displacement caused by the strain pulse is also leading to a carrier redistribution due to the deformation potential. This effect has not been studied in detail here, but could lead to an interesting study as part of further work.

#### 4.3.4 Microwave response of devices

The microwave response of devices fabricated from both Mn659 and Mn744 was measured in the continuous flow cryostat at a temperature of 4 K. A Gunn diode oscillator with a horn antenna acted as a source of 94 GHz

microwaves, which propagated through free space to the Schottky diode device via the optical access of the cryostat. As the measured signal was only small, a lock-in amplifier and an optical chopper were required as described in section 3.5. The signals observed on the lock-in amplifier were on the order of tens of microvolts, which was insufficient to perform the mixing experiments with a reasonable signal-to-noise ratio.

The poor response of these devices to incident microwaves is due to the fact that the bow-tie antenna were fabricated directly onto the GaAs substrate. GaAs has a high static dielectric constant of 12.5 [97]. At microwave frequencies, high dielectric materials are not commonly used as substrates for antenna. The large metal contact separated from a ground plane by a dielectric leads to the formation of a parallel plane waveguide type of structure. In this case, the ground plane was on the sample holder that the devices were mounted to. The incident microwave signal coupled into the antenna from free space is then largely converted to substrate modes within the high dielectric substrate, and this makes the antenna ineffective at coupling the microwave signal into the circuit [98]. Patch antenna for use at these frequencies are often made on materials such as quartz or Teflon-based substrates with a much lower dielectric constant in the range 2.6 - 3.5 [99, 100], in which the substrate modes are less pronounced. Examples of microstrip patch antenna fabricated on high dielectric materials such as Si ( $\epsilon_r = 11.7$ ) do exist, but typically the substrate beneath the antenna has been etched or machined away to create a lower effective dielectric constant [101, 102].

Alternative methods of creating an antenna were considered, such as fabricating the antenna on a separate quartz substrate and coupling the received microwave power into the device via bond wires. These fabrication methods were more complicated, and were not certain to improve performance due to other losses in the system, such as in the bond wires. A significantly more effective way of coupling in the microwaves would be through a waveguide, instead of via free space. However, the practicalities of getting an appropriate waveguide down the cryostat cabling is a challenge. Performing the experiments at room temperature is not feasible for the detection of the acoustic signal in these samples. With substrate thicknesses in the region of 350  $\mu\text{m}$  the attenuation of the acoustic phonons would be too great at room temperature.

## 4.4 Beam-lead Schottky diode

A beam-lead Schottky diode was provided by e2v, which had been designed as a microwave mixer for use with a 94 GHz local oscillator. It was mounted in a W-band waveguide circuit that provided a much better efficiency for coupling microwaves into the device compared to coupling through free space. The beam-lead Schottky diode was found to be sensitive to acoustic signals, as well as having a large response to the incident microwaves. The first results for mixing acoustic phonons with microwaves were obtained and are presented in this chapter.

### 4.4.1 Device structure and characterisation

The beam-lead Schottky diode was provided by e2v at the Microwave Technology Centre in Lincoln, and had the structure shown schematically in figure 4.11. The semiconductor sample consists of an  $n$ -doped GaAs substrate ( $n = 3 \times 10^{18} \text{ cm}^{-3}$ ), a  $4 \mu\text{m}$  thick  $n$ -doped GaAs buffer layer ( $n = 4 \times 10^{18} \text{ cm}^{-3}$ ) and a  $120 \text{ nm}$  thick  $n$ -doped GaAs active layer ( $n = 1 \times 10^{17} \text{ cm}^{-3}$ ). As the semiconductor chip is only  $100 \mu\text{m} \times 100 \mu\text{m}$  and it is also very thin, the device is contained in a glass moat for structural stability. The back surface of the substrate was etched until the GaAs was thinner than the glass moat, leaving a total GaAs thickness typically in the range  $10\text{-}15 \mu\text{m}$ . The Schottky and ohmic contacts were formed by thermal evaporation of the contact metals and electroplated gold beam-leads were fabricated. The Schottky contact has a diameter of  $3 \mu\text{m}$  and has been Au plated to approximately  $2 \mu\text{m}$  thick. There is a  $700 \text{ nm}$  thick  $\text{SiO}_2$  passivation layer on the active surface of the device.

The basic characteristics of the beam-lead Schottky diode were measured by e2v. The junction capacitance is  $\approx 1 \text{ fF}$  and the parasitic capacitance is  $\approx 20 \text{ fF}$ , making the total capacitance of the device  $\approx 35 \text{ fF}$ . The series resistance of the device is  $4 \Omega$ , and the ideality constant  $\alpha$ , defined in equation 4.7, is  $\approx 1.1$ .

A microscope image of the beam-lead Schottky diode is shown in figure 4.12a. The GaAs chip is the lighter square in the centre of the image,

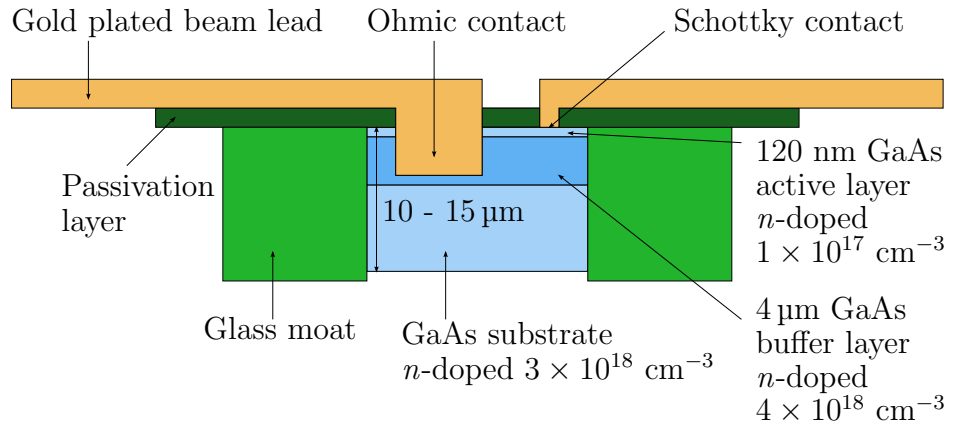


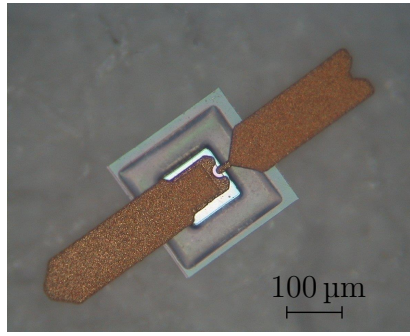
**Figure 4.11:** Schematic diagram of the beam-lead Schottky diode provided by e2v. A thin  $n$ -GaAs substrate with  $n$ -GaAs epilayers was supported by a glass moat. Ohmic and Schottky contacts were formed to different layers of GaAs and the beam-leads were gold plated.

surrounded by a glass moat. The two gold contacts are gold plated beam-leads that extend beyond the edges of the glass moat. The Schottky contact is the smaller contact on the right-hand side of the image, while the ohmic contact is the much larger contact on the left-hand side.

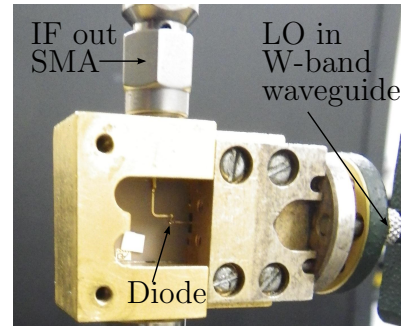
The Schottky diode was mounted in a microwave circuit, shown in figure 4.12b, with a W-band waveguide to allow for efficient coupling of microwaves to the device and an SMA port for DC and low frequency measurements.

The I-V characteristics of the beam-lead Schottky diode were found using a similar set-up to the one described in section 3.2. A  $10\text{ k}\Omega$  resistor was used as a current limiter to protect the diode from potentially damaging currents and only the forward voltage characteristics were investigated.

The I-V characteristics shown in figure 4.13 were taken with the 94 GHz microwave local oscillator (LO) source turned off and turned on. The LO signal was incident on the sample via an attenuator, tuned to give an output power of +10 dBm, followed by a W-band waveguide. With no LO present the device behaves as a typical diode with a turn on voltage of  $\approx 0.6\text{ V}$ . When the 94 GHz LO is applied to the device the I-V characteristics are quite different, with a significant flow of current at biases below the usual turn-on point of 0.6 V. This demonstrates the strong effect of the microwaves on the behaviour of the diode. The presence of the LO



(a) Microscope image of the beam-lead Schottky diode.



(b) Microwave circuit with beam-lead Schottky diode mounted.

**Figure 4.12:** The Schottky diode provided by e2v was formed on a square chip of GaAs supported in a glass moat. The diode was mounted in a microwave circuit with a W-band waveguide to couple in microwaves and an SMA port for DC and low frequency signals.

causing a current to flow in the Schottky diode with no applied bias shows that the diode is rectifying the LO signal. The I-V curve now extends into the negative bias range, despite only applying a positive bias to the device from the voltage source. This indicates how much negative bias must be supplied by the voltage source to have zero current flowing in the Schottky diode in the presence of the LO.

#### 4.4.2 Detecting acoustic signals using a beam-lead Schottky diode

The response of the beam-lead Schottky diode to picosecond acoustic signals was tested at room temperature using the method described in section 3.4. Initially, laser pulses with a wavelength of 800 nm were incident on the back face of the GaAs sample with no cavity present. This generated a broad frequency strain pulse that propagated across the thin substrate, which was known to be in the region of 10-15  $\mu\text{m}$  due to the device fabrication method. The strain pulse travelled to the Schottky diode and then caused a change in the voltage across the diode that was measured on the oscilloscope.

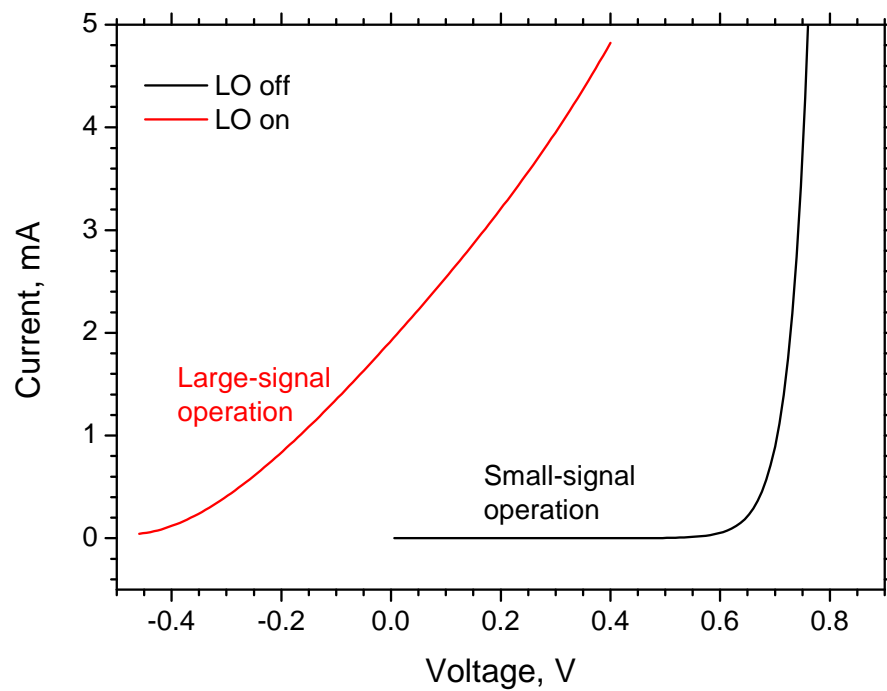


**Figure 4.13:** I-V characteristics of the beam-lead Schottky diode with and without the effect of the microwave local oscillator (LO). With the LO off, the I-V characteristics are those of a typical Schottky diode. With the LO on, a current is induced in the circuit, demonstrating the large response of this device to microwaves.

The acoustic signal measured by the oscilloscope is shown in figure 4.14. The large initial pulse (peak ‘a’) is the optical breakthrough, and is caused by a fraction of the 800 nm light passing through the GaAs to be directly detected by the Schottky diode. The following 3 signals (peaks ‘b’ - ‘d’) are acoustic signals. The time between the pulses  $t_0 = 2.3$  ns corresponds to acoustic signals travelling approximately 11  $\mu\text{m}$  in GaAs, which falls within the expected range of 10 - 15  $\mu\text{m}$  for the thickness of the sample. This method of acoustically probing the sample allows the thickness of the GaAs to be measured by a non-destructive method.

In the previous work by Moss *et al.* [47], and the results for the Mn744 Schottky diode presented in section 4.3.3, the initial acoustic signal was at a time  $t_0$  that corresponds to one trip across the substrate of the sample. Subsequent reflections were observed at intervals of  $2t_0$  as the acoustic signal had to make a round trip of twice the thickness of the substrate before being detected again by the Schottky diode. These samples had substrate thicknesses in the range 350-380  $\mu\text{m}$ .

With the beam-lead Schottky diode sample there are extra acoustic signals present, as a signal is observed at intervals of only  $t_0$ . These unexpected reflections (such as peak ‘c’ in figure 4.14) are caused by an acoustic pulse that is generated on the far side of the sample. The combination of the thin substrate of only 11  $\mu\text{m}$  and the low absorption coefficient for 800 nm light in GaAs allows a fraction of the incident laser light pulse to pass through the sample. It was found that 1.5% of 800 nm light incident on a 17  $\mu\text{m}$  thick piece of GaAs was transmitted through the entire thickness of the sample. As the GaAs in the beam-lead sample is only 11  $\mu\text{m}$  thick, a larger fraction  $\approx 5\%$  of incident light could be transmitted to the far side. As such, an acoustic wavepacket is generated at the far side of the sample at almost the same time as an acoustic wavepacket is generated at the near side. Although only 5% of the laser light intensity reaches the metal at the far side of the sample, generation of strain in metals is very efficient allowing the production of a strain pulse that is comparable in size to the one generated in the almost transparent GaAs. Acoustic signals are then observed at even multiples of  $t_0$  (peak ‘c’) as well as the expected ones at odd multiples of  $t_0$  (peaks ‘b’ and ‘d’). A similar effect was observed by Tas and Maris [3], in work where strain pulses induced optically in a metal film caused hot electrons to propagate to the far side of the film to generate

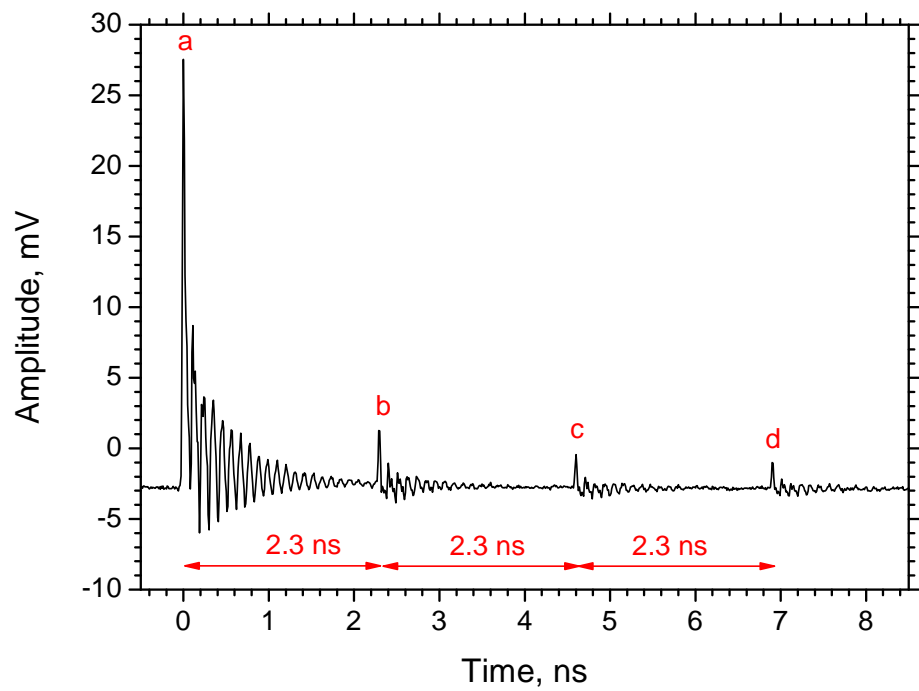


**Figure 4.14:** Acoustic signal detected by the beam-lead Schottky diode after propagation through the substrate. The initial pulse ‘a’ is the optical breakthrough and the later pulses are acoustic signals. Peak ‘b’ is the initial acoustic signal after propagation once across the substrate and peak ‘d’ is due to the same acoustic pulse after a round trip of the substrate caused by reflections at the surfaces. Peak ‘c’ is an unexpected peak due to an acoustic signal generated at the Schottky diode side of the sample.

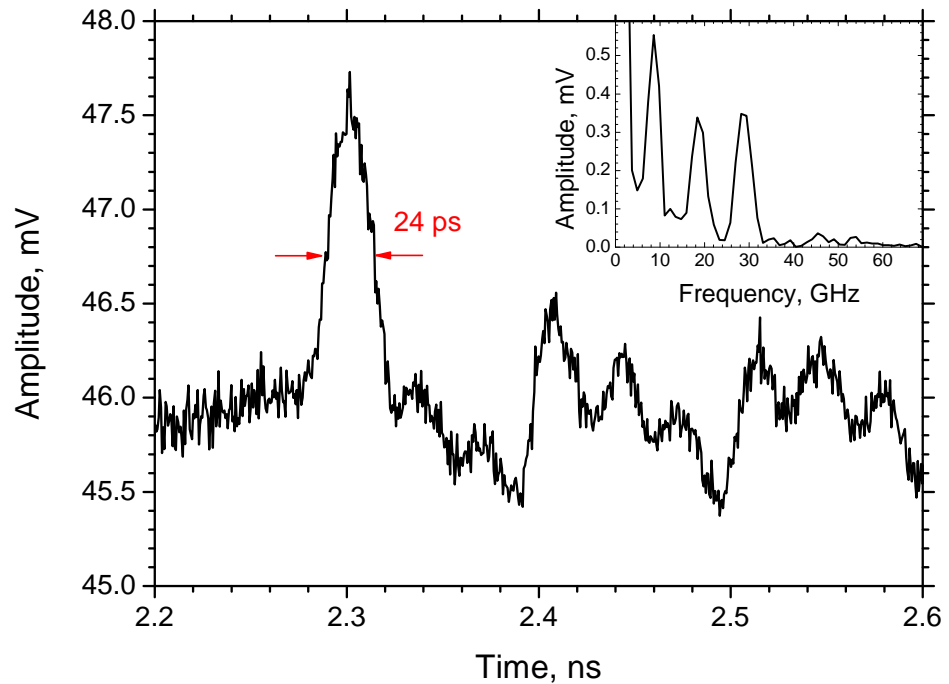


**Figure 4.15:** Zoomed-in view of acoustic signal detected by the beam-lead Schottky diode. The acoustic signal is the initial peak, with a width of 24 ps. The following ringing is electrical ringing set up in the circuit. This ringing comprises of 3 frequencies, as shown in the inset Fourier transform graph.

the additional acoustic wave at the film/substrate interface.

The acoustic signal detected by the beam-lead Schottky diode is shown in greater detail in figure 4.15. A sampling oscilloscope with a 70 GHz head was used for these measurements. The initial peak is the acoustic signal, with a width of 24 ps. The ringing following the initial peak is electrical ringing in the circuit, and the Fourier transform in the inset of figure 4.15 shows that this ringing is comprised of three frequencies that are harmonically related. This is probably due to a resonance or reflections set up in the waveguide circuit and is not of interest in this work.

When generating the acoustic signal with 800 nm wavelength light directly in GaAs, the acoustic signal observed is not a bipolar signal, in contrast with much of the literature about generating acoustic signals [1,8,47]. In general, to generate short duration strain pulses it is typical to use radiation that is weakly penetrating in the desired material, with penetration

depths on the order of 10s of nanometers [1]. The acoustic wavepacket is generated some distance into the sample and a portion travels back to the sample/air interface where it is reflected with a phase-shift of  $\pi$ , which causes the expected bipolar shape. By generating the acoustic wavepacket directly in the GaAs substrate with 800 nm light, as in this case, the optical radiation cannot be described as “weakly penetrating” as the penetration depth is on the order of a micron [103]. Indeed, a fraction of 800 nm laser light incident on a 17  $\mu\text{m}$  thick piece of GaAs was detected after propagation through the entire sample. The strongly penetrating radiation will, in general, give a low frequency acoustic signal due to the large area over which the optical energy is absorbed. However, the dominant part of the acoustic signal is caused by a sharp step change in the optical absorption at the air/sample interface. The presence of this step change leads to the generation of high frequency acoustic components. As these high frequency components are only generated at the surface, they do not form a bipolar signal. A very low frequency signal may be generated further into the material, which is reflected from the sample/air interface to form a bipolar pulse, but this is not observed in figure 4.15. It may be present, but with too low an amplitude to be distinguished from the electrical ringing that follows.

A comparison can be made to generation of the acoustic wavepacket using weakly penetrating 400 nm wavelength light, as shown in figure 4.16. The blue trace shows more of a bipolar characteristic, though this may be partially masked by the large electrical ringing present. This more bipolar shape is to be expected, as the strong absorption of this wavelength of light in GaAs will allow the generation of a picosecond strain pulse at a small distance into the sample that can then be reflected from the surface to form a bipolar pulse. The peaks in the two different traces in figure 4.16 have almost identical widths, which are roughly the same as the widths of the following electrical ringing peaks. This suggests that the rise time of the signal from the beam-lead Schottky diode is being limited by the measurement system.

Generating short duration acoustic signals with strongly penetrating light has been investigated both theoretically and experimentally by Babilotte *et al.* [7]. High frequency acoustic components are always generated, even in the case of strongly penetrating radiation, often providing only a

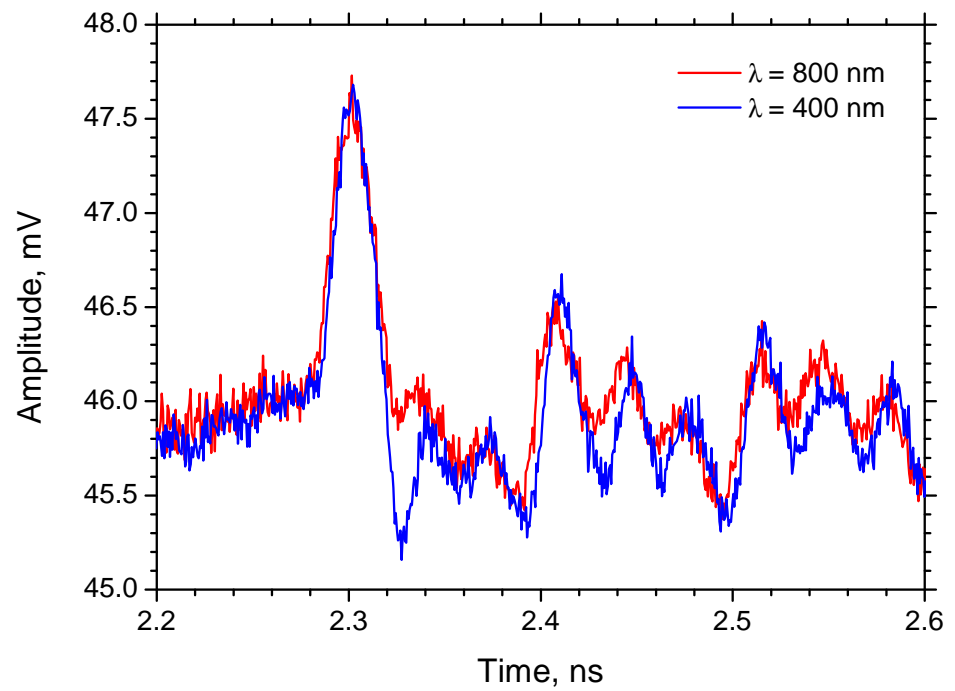


**Figure 4.16:** Comparison of the acoustic signal detected by the beam-lead Schottky diode when exciting the substrate with 800 nm and 400 nm wavelength light. For generation with strongly penetrating 800 nm light the signal is not bipolar. The weaker penetrating 400 nm light generates an asymmetric bipolar signal.

small contribution to the overall acoustic spectrum. The highest frequencies are generally difficult to detect by conventional pump-probe methods due to the penetration depth of the optical probe radiation causing the detection of the acoustic signal to occur over an extended region of space, leading to a broadening of very fast signals. As such, the probe radiation needs to be very weakly penetrating to detect over the smallest range possible. Pump-probe experiments with pump wavelength of 780 nm and probe wavelength of 390 nm produced roughly Gaussian signals with a width of  $\approx 6$  ps. These are similar in shape, but with a narrower width, to the signals observed with the beam-lead Schottky diode. As the width of the acoustic pulse in figure 4.15 is limited by the measurement system the true width of the peak could be much narrower.

The bias dependence of the acoustic signal detected by the beam-lead Schottky diode was investigated in figure 4.17. As measurements were only performed under the application of forward bias to avoid the possibility of damaging the diode provided by  $e2v$ , it is then difficult to make a direct comparison to previous published work that investigated the effect of reverse bias [47]. The observed signal from the beam-lead Schottky diode contains a large amount of electrical ringing as already seen in figure 4.15 and the signal now appears further frequency limited by the measurement system due to the inclusion of the bias tee.

There are no features in the observed signal caused by the acoustic pulse reflecting from the top surface of the sample and passing through the detection region a second time, in contrast with the complicated signal obtained from the Mn744 Schottky diode sample. The beam-lead device has  $2.0 \pm 0.5 \mu\text{m}$  of electroplated Au on top of the Schottky contact, so a reflection from the top surface of the sample would occur approximately 0.75-1.25 ns later than the initial signal, during the time window marked by an arrow on figure 4.17. The Mn744 sample was mounted such that the top surface of the device was free standing, and there is a very strong mismatch between the acoustic impedance of Au and air or vacuum [104], allowing strong reflections of the acoustic signal. The beam-lead Schottky diode is mounted face down in the circuit with Au epoxy, but this is only under the beam-leads themselves. The top surface of the plated Au is still likely to be in contact with air.

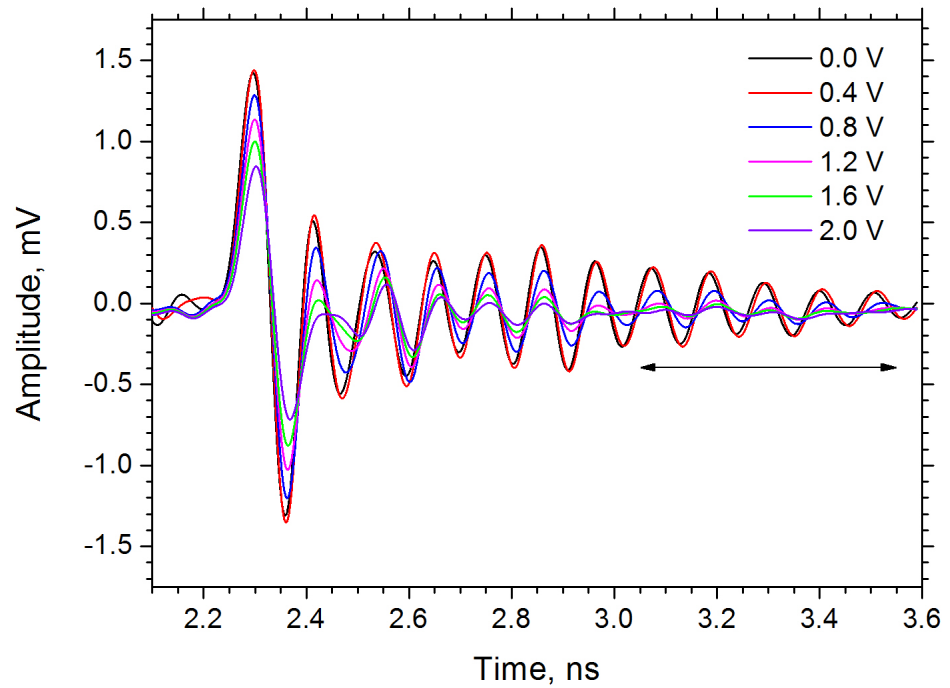


**Figure 4.17:** Bias dependence of the acoustic signal detected by the beam-lead Schottky diode. No reflection from the top of the device is observed, the time for this would be in the region marked with the arrow. A larger applied forward bias leads to a reduction in signal magnitude for both the acoustic signal and the following electrical ringing. The data is strongly rise-time limited by the measurement system.

The absence of an acoustic reflection in figure 4.17 could be attributed to the surface of the Au plate over the beam-lead Schottky diode area. The grain size in the electroplated Au gives the beam-lead sample a relatively rough finish compared to that of the thermally evaporated Au on the Mn744 device. Without a smooth top surface to the Au it is possible that there is no substantial specular reflection from the top surface of the Au plate directly over the Schottky contact. The signals caused by reflections of the acoustic pulses observed in figure 4.14 were probably due to the acoustic pulse reflecting from the relatively smooth GaAs surface and not the rough Au surface.

The application of bias has the effect of reducing the magnitude of both the acoustic signal detected by the beam-lead Schottky diode and the following electrical ringing. Little change in timing is observed with change in applied bias, similar to the bias dependence of the Mn744 device. In forward bias the depletion width is reduced as demonstrated in equation 4.5 and it is likely that the detection is taking place at the semiconductor-metal interface of the Schottky diode, again due to the deformation potential.

The semiconductor-metal interface of the Schottky diode has a thickness on the scale of atomic dimensions, that is  $\sim 5 \text{ \AA}$  [93]. Therefore, the detection region in the Schottky diode is much smaller than that in most optical pump-probe experiments, which is typically in the range 20-30 nm due to the absorption length of the probe beam radiation in the sample [1,105]. As such, it should be easier to detect the weak high frequency acoustic components generated by strongly penetrating laser radiation using a Schottky diode, as the acoustic signal is not broadened by detection over a relatively large distance.

The limiting factors in the results presented in this thesis are the external circuit and the measurement system. As the signal detected by the oscilloscope is clearly frequency limited, the internal processes of the device are too fast for the existing measurement set-up to accurately reproduce. This should not affect the heterodyne mixing experiments, as these utilise the fast internal processes of the diode to mix the two applied signals to produce an intermediate frequency signal in the frequency range that is easily detected by the current measurement system.

The effect of the presence of microwaves on the temporal profile of the acoustic response was investigated by performing the same experiment with the Gunn diode oscillator turned on, with the microwaves coupled to the device via the W-band waveguide circuit. The only noticeable effect on the voltage measured across the beam-lead Schottky diode was a slight reduction of the magnitude of the acoustic response. This is consistent with the fact that the rectification of the microwaves by the Schottky diode causes a change in the operating point of the diode. This rectification of the microwaves is equivalent to applying a larger bias across the Schottky diode, which has been shown in figure 4.17 to reduce the magnitude of the detected acoustic signal.

#### 4.4.3 Heterodyne mixing of optically-generated acoustic waves using a beam-lead Schottky diode

Heterodyne mixing experiments were performed using the e2v beam-lead Schottky diode at room temperature. Quasi-monochromatic acoustic signals, with centre-frequency  $f_0$ , were generated by modulation of the laser beam by the Fabry-Perot etalon as discussed in section 3.3.2. The electromagnetic local oscillator (LO) signal was provided by a Gunn diode oscillator and coupled to the beam-lead Schottky diode via a waveguide. The local oscillator frequency,  $f_{LO}$ , was 94 GHz. A constant DC bias was applied to the Schottky diode via a bias tee. The voltage across the Schottky diode was measured using a 12.5 GHz bandwidth real-time oscilloscope and the Fourier transform of the signal was taken to determine the intermediate frequency,  $f_{IF}$ , produced.

It was not possible to see evidence of mixing in the temporal signal as the Gunn diode oscillator and the pulsed laser were not phase-locked. Any IF components present in the detected signal did not have a constant phase relationship between signals produced by different laser pulses. Averaging in the temporal regime caused the IF components to cancel out with one another. Instead, the Fourier power spectrum of each temporal trace was taken and these were averaged together.

To provide evidence of mixing, the distance between the cavity mirrors

was adjusted to change the centre frequency ( $f_0$ ) of the narrow-band acoustic signal. With a fixed LO frequency this should cause a change in the intermediate frequency detected,  $f_{IF}$ . To be able to detect  $f_{IF}$  using the 12.5 GHz bandwidth real-time oscilloscope, the cavity spacing needs to be set such that  $f_0$  is within the range

$$(f_{LO} - 12.5 \text{ GHz}) < mf_0 < (f_{LO} + 12.5 \text{ GHz}) \quad (4.8)$$

where  $m$  is an integer, all frequencies are in gigahertz and 12.5 GHz is due to the bandwidth of the oscilloscope. As the acoustic wavepackets generated include frequency components at the second harmonic with a reasonable amplitude, it is possible to perform the mixing experiments with either the fundamental frequency ( $m = 1$ ) or the second harmonic frequency ( $m = 2$ ). The acoustic frequency  $mf_0$  that is to be mixed with the LO must be within 12.5 GHz of  $f_{LO}$  such that the IF component generated at the difference frequency will be within the bandwidth of the oscilloscope.

Results from these heterodyne mixing experiments are presented in figures 4.18 and 4.19. Two sets of data are discussed, one in which the second harmonic of the acoustic signal generated in the sample was mixed with the LO, and one for the fundamental acoustic frequency.

### **Mixing with the second harmonic acoustic frequency**

The first evidence of mixing a quasi-monochromatic acoustic signal with a microwave LO is demonstrated in figure 4.18. In this case, the cavity spacing was set to generate frequencies  $f_0$  from 41-52 GHz. This leads to a strong frequency component in the acoustic signal in this range, but also a significant component at the 2nd harmonic,  $2f_0$ . The frequency range of the second harmonic is 82-104 GHz, which when mixed with the 94 GHz LO signal produces intermediate frequencies,  $f_{IF} = (2f_0 - 94 \text{ GHz})$ , which fall within the bandwidth of the oscilloscope. The Fourier transform of the intermediate frequency signal is plotted for different cavity spaces and hence different values of  $f_0$ .

A clear peak is observed in the IF signal that shifts in frequency for different values of  $f_0$ . The zero on the frequency axis corresponds to  $2f_0 = f_{LO} = 94 \text{ GHz}$ . Negative and positive intermediate frequencies cor-

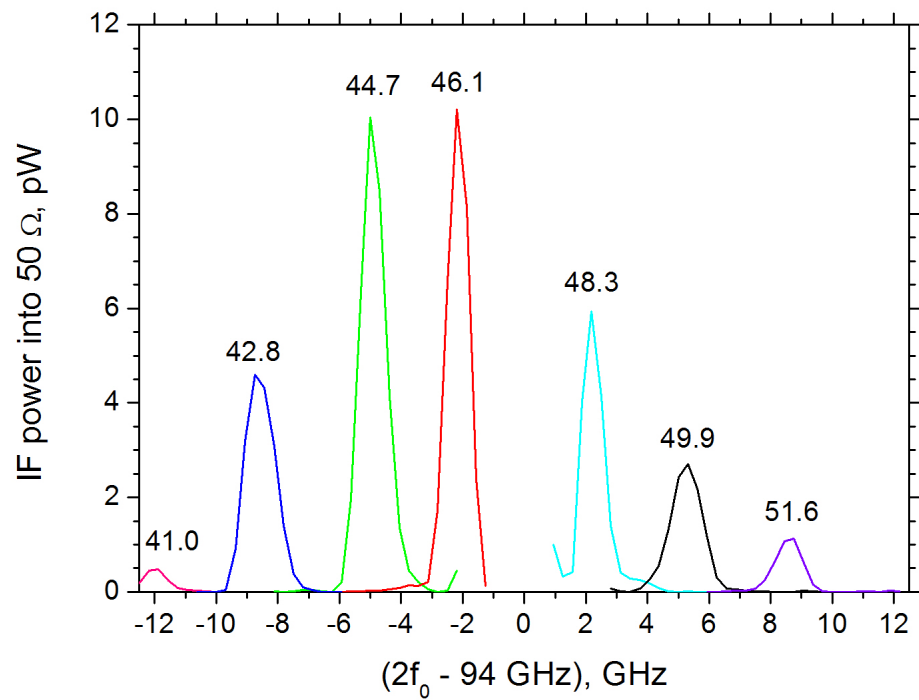


**Figure 4.18:** Results for heterodyne mixing of a microwave local oscillator signal of frequency 94 GHz, with the 2nd harmonic acoustic signal of frequency  $2f_0$  using a beam-lead Schottky diode. The Fourier transform of the IF signal measured across the Schottky diode is shown for a range of acoustic frequencies  $2f_0$ . The values of  $f_0$  are marked on the corresponding peaks.

respond to an acoustic signal with centre frequency  $2f_0$  that is less than and greater than the 94 GHz LO frequency, respectively.

The width of the peaks in the IF are  $\approx 1$  GHz, and are fairly constant for all values of  $f_0$ . The amplitude of the peaks for different  $f_0$ , however, are not constant. One effect accounting for this is the fact that the passband of the measurement system will not be uniform. This includes the oscilloscope, cabling, bias tee and amplifiers. The passband will behave as a low pass filter, with the signal transmission rolling off towards higher frequencies. The peaks for larger difference frequency are closer to the edge of the system's passband and so their amplitude is reduced relative to those with a lower difference frequency. This can be seen quite clearly in figure 4.18, with the peaks closer to zero having larger amplitude than those near to the edges of the graph.

Another trend observed in the amplitude of the peaks is that for the same  $|f_{IF}|$  the amplitude of the peaks are much larger for  $f_{IF} < 0$ , compared to those with  $f_{IF} > 0$ . This corresponds to larger amplitudes of the IF components for a smaller acoustic centre frequency  $f_0$ . This is due to the frequency spectrum of the individual, broad-frequency acoustic pulses that form the train of pulses. A single acoustic wavepacket generated optically in the GaAs will have a broad spread of frequency components, with the contribution from a given frequency decreasing towards higher frequencies. An example spectrum of an acoustic wavepacket generated with 780 nm is given by Babilotte *et al.* [7] in which the amplitude of components around 100 GHz is roughly a factor of 10 smaller than components around 10 GHz. The Fabry-Perot etalon forms a train of these broad-spectrum pulses, with a time separation between pulses that corresponds to the centre frequency of the quasi-monochromatic spectrum. However, to be able to modulate the acoustic spectrum at a given frequency, that frequency must already be present in the initial broad spectrum. So if the amplitude of a given frequency is smaller in the broad-spectrum acoustic wavepacket, the amplitude available for the modulated signal will also have to be smaller.

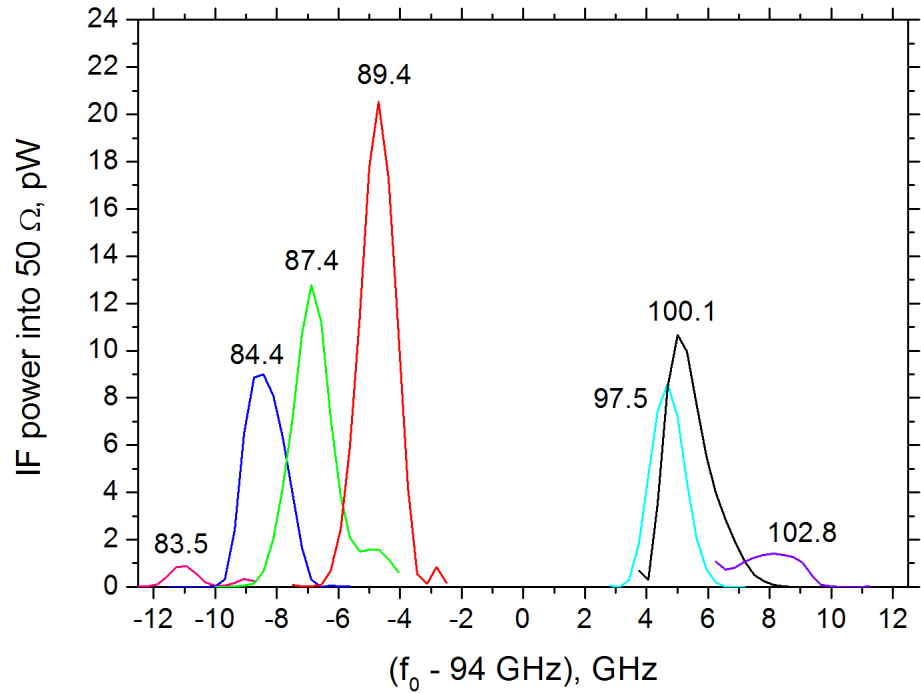


**Figure 4.19:** Results for heterodyne mixing of a microwave local oscillator signal of frequency  $f_{LO}$ , with the fundamental frequency acoustic signal of frequency  $f_0$  using a beam-lead Schottky diode. The Fourier transform of the IF signal measured across the Schottky diode is shown for a range of acoustic frequencies  $f_0$ . The values of  $f_0$  are marked on the corresponding peaks.

### Mixing with the fundamental acoustic frequency

Evidence of mixing quasi-monochromatic acoustic waves with microwaves was also obtained when the cavity was set to smaller spacings and  $f_0$  was in the range 83-103 GHz. In this situation, the fundamental frequency generated in the sample was mixed with the 94 GHz LO signal to produce intermediate frequencies of  $f_{IF} = (f_0 - 94 \text{ GHz})$ , which fall within the bandwidth of the oscilloscope. The Fourier transform of the intermediate frequency signal for different cavity spaces, and hence different values of  $f_0$ , are shown in figure 4.19.

Once again, there are peaks present in the Fourier transform of the IF signal, which shift in frequency for different values of  $f_0$ . The zero on the

frequency axis corresponds to  $f_0 = f_{LO} = 94$  GHz. Negative and positive intermediate frequencies correspond to an acoustic signal with centre frequency  $f_0$  that is less than and greater than the 94 GHz LO frequency, respectively. The widths of the peaks this time are  $\approx 1.5$  GHz.

Similar observations about the variation of the amplitude of the peaks can be made to those already discussed for the second harmonic. The amplitude of the peaks in the IF signal are again largest for smaller difference frequencies due to the pass band of the measurement system rolling off at higher frequencies. The amplitude of the peaks are also larger for  $f_{IF} < 0$  when compared to  $f_{IF} > 0$ , as the frequency spectrum of the individual broad-spectrum acoustic wavepackets generated by individual laser pulses contains more components at lower frequencies.

In both regimes, the graphs presented in this section show the production of an intermediate frequency that varies in frequency as expected as one of the input frequencies is adjusted. This represents good evidence of heterodyne mixing of quasi-monochromatic acoustic waves with microwaves using the beam-lead Schottky diode.

#### 4.4.4 Further analysis of mixing results

##### Spectral width of the intermediate frequency peaks

No oscillator is perfectly monochromatic and the oscillator used to generate the LO signal will have some defined spectral width due to the phase noise. Phase noise has a Lorentzian spectrum defined as

$$\mathcal{L}(f_{off}) = \frac{1}{\pi} \frac{\pi f_{osc}^2 C_{osc}}{(\pi f_{osc}^2 C_{osc})^2 + f_{off}^2} \quad (4.9)$$

where  $\mathcal{L}(f_{off})$  is the phase noise expressed as a ratio,  $f_{osc}$  is the carrier frequency,  $f_{off}$  is the offset frequency from the carrier and  $C_{osc}$  is a scalar constant relating to the phase noise of a particular oscillator [106]. The spectral line width of the oscillator is determined using

$$f_{FWHM} = 2\pi f_{osc}^2 C_{osc} \quad (4.10)$$

Combining equations 4.9 and 4.10 and solving for  $f_{FWHM}$  allows the spectral width of the oscillator to be calculated. The Gunn diode oscillator

phase noise specification is between -75 and -80 dBc/Hz at 100 kHz from the centre frequency. This corresponds to a spectral width of the 94 GHz LO signal of <20 MHz. The measured spectral width of the IF frequency is  $\approx 1.5$  GHz, and as this is much larger than the spectral width of the LO it is expected that the spectral width of the IF is the same as that of the acoustic signal component used in the mixing experiment.

### Spectral components of the intermediate frequency

Let us assume that the strain evolution in the acoustic wavepacket at the metal-semiconductor interface,  $s_{zz}(t)$ , is slower than the characteristic time defined as  $\frac{l_s}{v_s}$ , where  $v_s$  is the sound velocity and  $l_s$  is the screening length. As the strain pulse propagates through the junction it changes the electric field present in the device, and the charge carriers redistribute to oppose this change. The screening length is the length scale over which this process occurs. Outside of the screening length the changes caused by the strain pulse are effectively screened by the moving carriers. The screening length,  $l_s$ , will be on the order of a few nanometres.

The voltage induced at the interface caused by the acoustic signals is

$$v_{ac}(t) = \frac{\Xi_{eff}}{e} s_{zz}(t) \quad (4.11)$$

where  $\Xi_{eff}$  is the effective deformation potential in the metal and  $e$  is the charge of an electron. The injection power of the local oscillator (LO) is +10 dBm into  $50 \Omega$ , corresponding to a peak LO amplitude of  $V_{LO} = 1$  V. As an applied bias of 1 V comfortably exceeds the diode turn on voltage, as shown in figure 4.13, we can consider the case of a single-ended diode mixer with high-level LO injection. Assuming that the diode junction capacitance is sufficiently small that the reactive current contribution is negligible at the frequencies of interest, the time dependent current in the diode can be written as

$$i(t) = g(t)v_{ac}(t) \quad (4.12)$$

where  $g(t)$  is the time dependent part of the conductance of the diode due to the presence of the LO. Consider a typical diode current-voltage characteristic

$$I(V) = I_S(e^{V/\alpha k_B T} - 1) \quad (4.13)$$

where  $I_S$  is the reverse saturation current,  $e$  is the charge of an electron,  $\alpha$  is the diode ideality factor explained in section 4.2.1,  $k_B$  is the Boltzmann constant and  $T$  is the temperature. Following the approach of Professor A. J. Kent (A. J. Kent, personal communication, February 2015) equation 4.13 can be expanded about the point  $(V_{ap} + v_{LO}(t))$ , where  $V_{ap}$  is any applied DC bias, and  $v_{LO}(t) = V_{LO}\cos(2\pi f_{LO}t + \varphi)$  is the local oscillator signal. This leads to an expression for the change in current through the device due to the presence of the acoustic signal of

$$i(v_{ac}) = v_{ac} \left( \frac{dI}{dV} \right)_{V_{ap}+v_{LO}(t)} + \left( \frac{v_{ac}^2}{2} \right) \left( \frac{d^2I}{dV^2} \right)_{V_{ap}+v_{LO}(t)} + \left( \frac{v_{ac}^3}{6} \right) \left( \frac{d^3I}{dV^3} \right)_{V_{ap}+v_{LO}(t)} + \dots \quad (4.14)$$

The voltage induced by the acoustic signal,  $v_{ac}$ , is on the order of millivolts, and this can be used to show that the first term in this expansion is much larger than the others. It is then sufficient to consider just the first term of the expansion, which can be divided by  $v_{ac}(t)$  to produce an expression for the conductivity as a function of time

$$\begin{aligned} g(t) &= \left( \frac{dI}{dV} \right)_{V_{ap}+v_{LO}(t)} \\ &= \frac{I_S e}{\alpha k_B T} e^{e(V_{ap}+v_{LO}(t))/\alpha k_B T} \\ &= \frac{I_S e}{\alpha k_B T} e^{eV_{ap}/\alpha k_B T} e^{eV_{LO}\cos(2\pi f_{LO}t+\varphi)/\alpha k_B T} \end{aligned} \quad (4.15)$$

The acoustic signal used in the mixing experiments was a train of strain pulses generated by the optical output from the Fabry-Perot cavity. The pulses were attenuated and delayed due to multiple reflections of the initial laser pulse inside the cavity. This can be expressed as

$$v_{ac}(t) = \frac{\Xi_{eff}}{e} \sum_{m=0}^{\infty} (r_1 r_2)^m s_{zz(0)} \left( t - \frac{m}{f_0} \right) \quad (4.16)$$

where  $m$  is an integer,  $r_{1,2}$  are the reflection coefficients of the cavity mirrors,  $\frac{1}{f_0}$  is the time for a light pulse to complete a round trip of the cavity and  $s_{zz(0)}$  describes the shape of the acoustic signal produced by the first optical pulse in the train ( $m = 0$ ). Substituting equations 4.15 and 4.16 into equation 4.12 leads to the time dependent part of the diode current

$$i(t) = \frac{I_S \Xi_{eff}}{\alpha k_B T} e^{eV_{ap}/\alpha k_B T} e^{eV_{LO}\cos(2\pi f_{LO}t+\varphi)/\alpha k_B T} \sum_{m=0}^{\infty} (r_1 r_2)^m s_{zz(0)} \left( t - \frac{m}{f_0} \right) \quad (4.17)$$

The frequency spectrum of the current in the diode can be found by taking the Fourier transform of equation 4.17. In the experiments performed, the phase of the LO signal from the Gunn diode oscillator changed randomly between measurements. To be able to average together multiple traces to improve the signal-to-noise ratio the power spectrum  $|I(\omega)|^2 R_L$  was taken and then averaged, where  $R_L$  is the load resistance. The actual strain pulse shape,  $s_{zz(0)}$ , is difficult to determine quantitatively and the diode characteristics deviate from the ideal form. As such, a full quantitative analysis of the power spectrum is beyond the scope of this work. However, by inspecting equation 4.17 the main experimental observations can be accounted for.

First consider the spectrum of  $v_{ac}(t)$ . Let the Fourier transform of the strain pulse shape  $s_{zz(0)}$  be  $S_{zz(0)}$ . Applying the shift theorem and noting that  $r_1 r_2 < 1$  to take the sum of a geometric series leads to

$$\begin{aligned} V_{ac}(\omega) &\propto \sum_{m=0}^{\infty} (r_1 r_2)^m S_{zz(0)}(\omega) e^{-im\omega/f_0} \\ &\propto \frac{S_{zz(0)}(\omega)}{1 - r_1 r_2 e^{-i\omega/f_0}} \end{aligned} \quad (4.18)$$

The frequency spectrum of the strain induced voltage  $V_{ac}(\omega)$  contains peaks that correspond to harmonics of  $f_0$ . If the spectrum of the strain pulse,  $S_{zz(0)}(\omega)$ , contains sufficiently high frequency components, and these components are not too strongly attenuated as the acoustic wavepacket crosses the substrate of the sample, then  $V_{ac}$  will contain harmonic terms proportional to  $\cos(2m_1\pi f_0 t)$ , where  $m_1$  is an integer. By expanding the expression  $e^{eV_{LO}\cos(2\pi f_{LO}t + \varphi)/\alpha k_B T}$  in a Maclaurin series it can be shown that the change in conductivity of the diode  $G(\omega)$ , due to the LO contains terms of  $\cos^{m_2}(2\pi f_{LO}t + \varphi)$ , where  $m_2$  is an integer.

To investigate the frequency components produced in the mixing experiments, the product of the terms  $\cos(2m_1\pi f_0 t)$  and  $\cos^{m_2}(2\pi f_{LO}t + \varphi)$  is taken using  $m_1 = 2$  and  $m_2 = 1$ . This corresponds to the situation in which the fundamental frequency of the LO is mixed with the second harmonic of the cavity frequency. This leads to components at the difference frequency  $(2f_0 - f_{LO})$ , which were detected in the experiment. Alternatively the use of  $m_1 = 1$  corresponds to using the fundamental frequency produced by the cavity. Many other frequencies corresponding to other combinations of  $m_1$  and  $m_2$  are produced, but as they do not fall within the 12.5 GHz

bandwidth of the oscilloscope they are not detected.

This analysis has been expanded upon by a collaborator, Dr B. A. Glavin, to produce a theoretical calculation of the intermediate frequency power spectral density  $P$ . The finite-value LO voltage was assumed and the voltage due to the strain pulse was treated as a perturbation  $U^{(1)}$ . The IF power was defined as  $P = R_L^{-1} \langle |\tilde{U}^{(1)}|^2 \rangle$  where  $\tilde{U}^{(1)}$  denotes the Fourier spectrum of the voltage perturbation and  $\langle \rangle$  indicates averaging over the phase  $\varphi$ . The perturbation was expanded in a Fourier series to produce the expression

$$P \approx \frac{(A_1^2 + B_1^2)}{2R_L} \left( \frac{|S_{zz(0)}(\omega_{LO} + \omega)|^2}{1 + r_1^2 r_2^2 - 2r_1 r_2 \cos(2\pi(\omega_{LO} + \omega)/\omega_0)} + \frac{|S_{zz(0)}(\omega_{LO} - \omega)|^2}{1 + r_1^2 r_2^2 - 2r_1 r_2 \cos(2\pi(\omega_{LO} - \omega)/\omega_0)} \right) \quad (4.19)$$

where  $A_1$  and  $B_1$  are Fourier coefficients from the expansion,  $\omega_0 = 2\pi f_0$  is the angular frequency of the acoustic signal generated by the cavity, and the remaining symbols have been defined previously. Only the sum and difference frequency terms have been included here for simplicity, but many other frequencies are generated. For  $r_1 r_2$  close to unity and under the condition  $\Delta\omega = (\omega - \omega_{LO}) \ll \omega_0$ , the power spectral density  $P$  has a Lorentz-like form

$$P \approx \frac{(A_1^2 + B_1^2) |S_{zz(0)}(2\omega_0)|^2 \omega_0^2}{8\pi^2 R_L r_1 r_2} \left( \frac{1}{|\omega - \Delta\omega|^2 + \gamma^2} + \frac{1}{|\omega + \Delta\omega|^2 + \gamma^2} \right) \quad (4.20)$$

where

$$\gamma = \frac{\omega_0(1 - r_1 r_2)}{2\pi\sqrt{r_1 r_2}} \quad (4.21)$$

Glavin calculated  $P$  using equation 4.20 while assuming ideal diode characteristics and a Gaussian profile for  $S_{zz(0)}$ . When mixing the second harmonic acoustic signal with the fundamental frequency of the local oscillator  $\Delta\omega = (2\omega_0 - \omega_{LO})$ . The results obtained from this calculation are presented in figure 4.20. This theoretical analysis produces narrow peaks in the IF with centre frequencies that can be seen to closely match those of the experimental data shown in figure 4.18. The width of the calculated peaks are  $\approx 1.5$  GHz and so agree closely with the values obtained experimentally.

Comparison of the magnitude of the peaks is difficult due to the un-

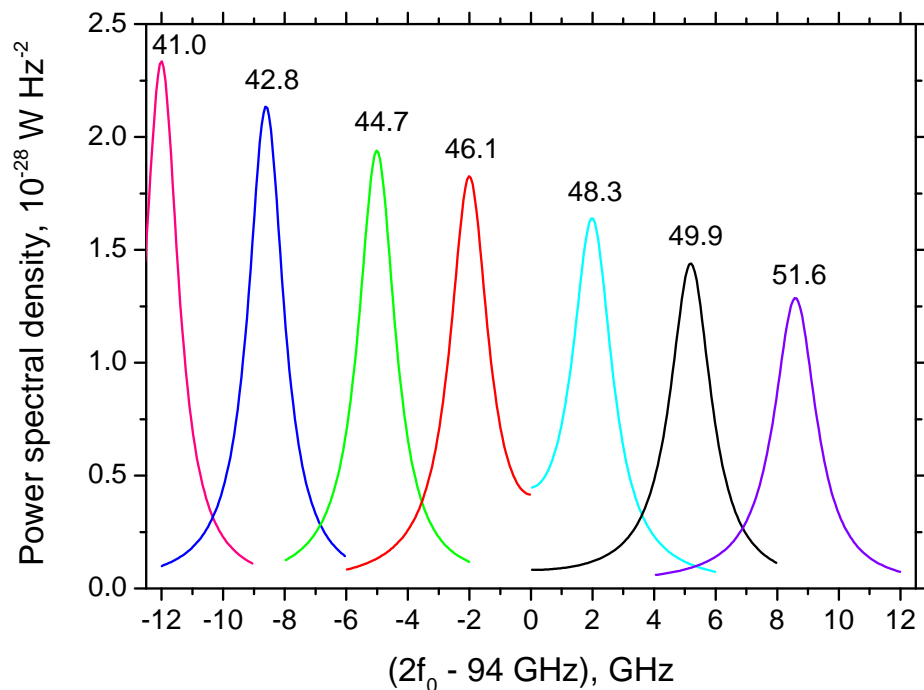


**Figure 4.20:** Theoretical calculation of the IF spectrum for mixing of the microwave LO with the 2nd harmonic acoustic signal, produced by B. A. Glavin using the expression in equation 4.20.

certainty in several factors such as the size and shape of the initial strain pulse, the value of the deformation potential, and phonon scattering in the substrate of the sample. The external circuit also has an effect on the magnitude of the observed peaks, as previously discussed. However, it is possible to make a rough comparison of the magnitudes between the experiment and the theoretical calculation. Consider the peak at  $f_0 = 44.7$  GHz in figure 4.18, as this peak is far from the edge of the bandwidth of the measurement system. To compare amplitudes with those in figure 4.20 the 500 MHz resolution bandwidth of the oscilloscope spectrum analyser must be taken into account. Thus, the experiment gives  $P = 10 \text{ pW}/(500 \times 10^6)^2 = 4 \times 10^{-29} \text{ W Hz}^{-2}$ , which roughly agrees to the order of magnitude with the calculated result.

The tails of the Lorentz-like peaks are not observed in the experimental mixing results. This is probably due to the broadband noise background from the signal averaging obscuring the smaller amplitude tails. This noise

background has been subtracted from the results presented in figures 4.18 and 4.19.

### **Comparison of mixing results using the fundamental frequency and the second harmonic acoustic signal**

It is interesting to directly compare the results between figures 4.18 and 4.19. The amplitude of the IF peaks in the Fourier transform is consistently larger for the case in which the cavity spacing was smaller and the fundamental frequency of the acoustic signal was mixed with the LO. However, the peak width is greater and the peaks are less well defined.

A simple simulation was generated in Matlab to compare the frequency spectrum of the modulated acoustic wavepacket generated for the different Fabry-Perot cavity spacings,  $d$ , used in the experiments described. A series of delta functions, with spacing equal to the time between optical pulses exiting the cavity, was generated with a decaying amplitude based on the reflectivities of the cavity mirrors. It was assumed that only a finite number of optical pulses would generate an acoustic pulse in the sample with reasonable amplitude; 20 pulses were used for the purpose of this simulation. To represent the acoustic signal generated in the sample, the train of optical pulses was then convolved with a Gaussian profile with a 6 ps width [7] to represent the broad frequency acoustic pulse generated by a single optical pulse. The fast Fourier transform was obtained to determine the frequency spectrum of the acoustic wavepacket and the results for two relevant cavity spacings are shown in figure 4.21.

A cavity spacing of  $d = 1.5$  mm corresponds to generating 100 GHz components as the fundamental frequency, while a cavity spacing of  $d = 3$  mm leads to a fundamental frequency of 50 GHz and a smaller contribution at the second harmonic at 100 GHz. The calculated widths of the peaks are not accurately represented, as both the width of the broad acoustic signal and the number of pulses were estimated, but they agree with the observed widths of the peaks within roughly a factor of two. No attempt has been made to calculate the absolute magnitudes of the peaks as there are several unknown variables to estimate, it is only the relative magnitudes that are of interest here.

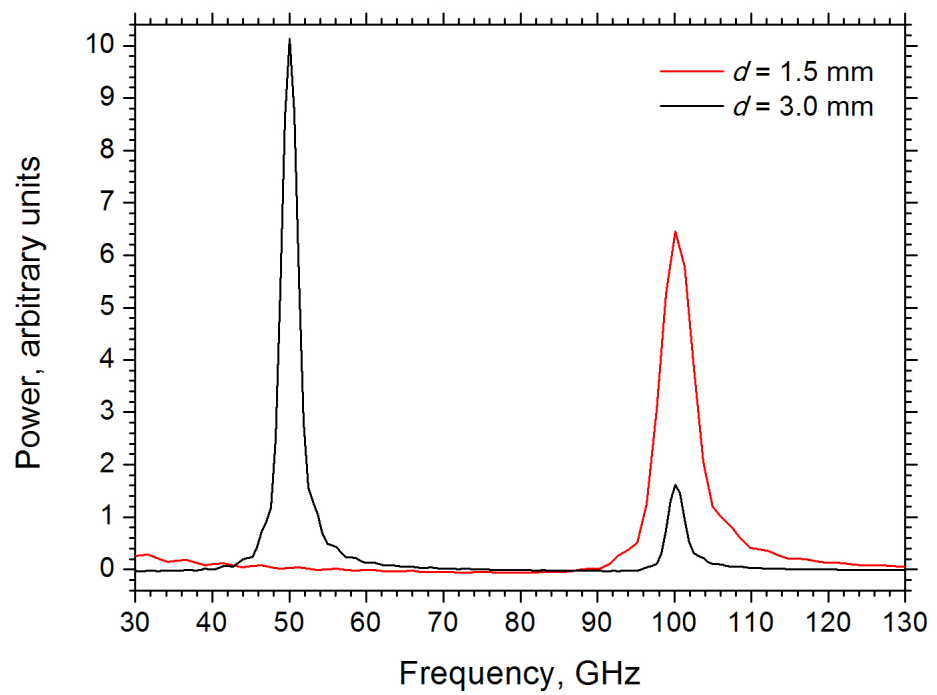


**Figure 4.21:** Simulation results for frequency components present in the modulated acoustic signal for two different values of the cavity spacing,  $d$ . The amplitude of a given frequency component is larger when it is generated as the fundamental frequency instead of as the second harmonic.

The simulation results in figure 4.21 clearly show that the contribution at 100 GHz is larger when the 100 GHz component is generated as the fundamental frequency compared to the second harmonic, in agreement with the observed relative amplitudes in the heterodyne mixing experiments. This suggests that the generation of a particular frequency as the fundamental frequency is more efficient than generating it as the second harmonic. This is perhaps expected, as for the 3 mm cavity spacing the signal will be strongly modulated at 50 GHz. As the signal is not a perfect sine wave it can be constructed as a sum of harmonically related sine and cosine waves, as in standard Fourier series [107], and there will be a component at 100 GHz. This 100 GHz modulation is likely to be less pronounced in the acoustic signal than the 50 GHz set by the cavity spacing.

The relative widths of the peaks from the simulation are also in agreement with the experimental observation that the peaks were wider for mixing with the fundamental frequency compared to that at the second harmonic. In figure 4.21 the width of the peak at 100 GHz is larger for the 1.5 mm cavity spacing than for the 3 mm spacing. This is likely to be due to the decay in time of the modulated acoustic signal. The train of optical pulses from the Fabry-Perot has a decaying amplitude, due to the partial reflectivity of the cavity mirrors. There will be some number of pulses after which the amplitude of the laser pulse is too small to effectively generate an acoustic signal in the sample. This number of pulses will be constant, independent of the cavity spacing. However, the cavity spacing determines the time separation of the optical pulses; for a larger cavity spacing there is a longer time between pulses. This means that the decay constant of the modulated acoustic signal is effectively longer for larger cavity spacings, and the width of the peak in the Fourier transform is therefore narrower.

This simple simulation can also be used to investigate the high frequency limit of this acoustic modulation technique. For a 6 ps width Gaussian strain pulse, as assumed here, there is a strong component present in the Fourier transform of the expected acoustic signal up until a frequency of 150 GHz. At this frequency the period of the optical pulses generated by the cavity is comparable to the width of the strain pulse so there is limited modulation of the acoustic signal.

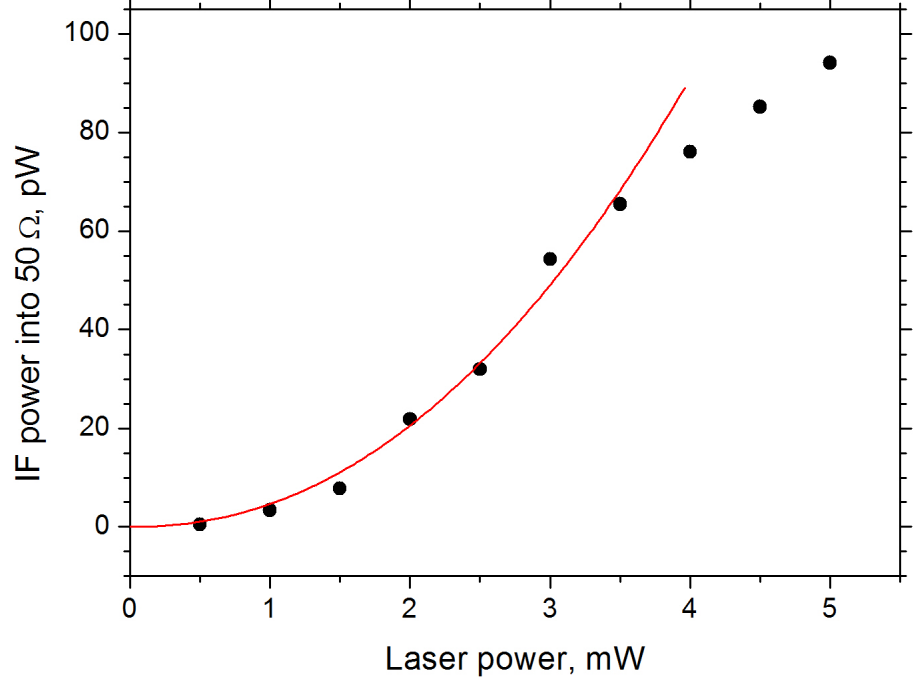


**Figure 4.22:** Laser pump power dependence of peak IF power at a frequency of  $(2f_0 - 94 \text{ GHz}) = -6.2 \text{ GHz}$ . The red curve shows a power law fit to the data of the form  $y = a_1 x^{a_2}$ , where  $a_1 = 4.7 \pm 0.9$  and  $a_2 = 2.1 \pm 0.2$ . The data deviates appreciably from this fit at laser powers above approximately 3.5 mW.

### Laser power dependence of the intermediate frequency

It can be seen from equation 4.18 that the IF power ( $\propto V_{ac}^2$ ) should be proportional to the square of the amplitude of the strain, and hence proportional to the square of the pump laser power. The peak power of the IF produced was determined for a range of pump laser powers for an IF of  $(2f_0 - 94 \text{ GHz}) = -6.2 \text{ GHz}$ . This is shown in figure 4.22, where the red curve is a power law fit to the experimental data of the form  $y = a_1 x^{a_2}$ , where  $a_1 = 4.7 \pm 0.9$  and  $a_2 = 2.1 \pm 0.2$ . This is close to being a square law within the associated error, which is consistent with the earlier analysis. The deviation observed at high pump power ( $> 3.5 \text{ mW}$ ) is probably due to non-linear effects in the strain generation process.

## 4.5 Conclusion

Schottky diodes have been investigated as the mixer element in the heterodyne mixing of optically generated coherent acoustic phonons with microwaves, and it has been shown that they are successful in this application.

Initially, Schottky diodes were fabricated from two semiconductor wafers grown at the University of Nottingham for use in the heterodyne mixing experiments. These device structures included bow-tie antenna to couple in the incident microwaves from free space. The Schottky diodes responded well to an incident acoustic signal, and were compared to previous Schottky diodes that have been used to detect picosecond strain pulses. However, their microwave response was poor, and this was due to the integrated antenna being fabricated on high dielectric GaAs. The incident microwave energy collected by the antenna was probably converted into substrate modes in the GaAs instead of being effectively coupled to the Schottky diode.

A beam-lead Schottky diode was provided by e2v mounted in a W-band waveguide circuit. This arrangement was substantially better at coupling in incident microwaves, and the first evidence of heterodyne mixing of quasi-monochromatic acoustic phonons with microwaves was obtained. A fixed frequency local oscillator signal was mixed with a tunable acoustic signal to produce an intermediate frequency that was seen to shift in frequency as expected. This was observed for both the fundamental acoustic frequency and the second harmonic generated in the sample.

The Fabry-Perot cavity used to produce the quasi-monochromatic acoustic signals is effective up to a frequency of approximately 150 GHz. To perform heterodyne mixing experiments at higher frequencies it would be possible to employ a superlattice transducer to generate the acoustic wavepacket. These are not tunable as they are a fixed structure, but they offer a means to access higher frequency acoustic signals for use as an acoustic local oscillator in a mixer detector for the detection of incoming electromagnetic signals.

## Chapter 5

# Electrical detection of confinement of acoustic phonons in a superlattice

This chapter includes details of the experiments performed to electrically detect picosecond acoustic signals using a semiconductor superlattice (SL). The detection of incoming acoustic phonons using superlattices has been previously studied using incoherent heat pulse experiments [51] and coherent optical methods [49]. The experiments discussed in this chapter used a superlattice device to electrically detect coherent acoustic phonons and investigate their effect on the electron transport in the superlattice.

First, some of the background on semiconductor superlattices and their relevant properties are discussed. Superlattice research is a large and ongoing area of work and it cannot possibly all be covered in this chapter. Only the information required to understand the results presented in this chapter are included.

This is followed by the experimental results obtained from a 50 period GaAs/AlAs superlattice sample. A range of Al thin film acoustical transducers were used on the opposite side of the substrate and transient voltages were detected across the SL due to the incident acoustic wavepacket. The case of the thinnest Al film showed an interesting effect, which was not present for thicker Al films. This took the form of a peak with a width of

2 ns, which is too slow to be a strain pulse and too fast to be a heat pulse. It is proposed that this extra contribution to the signal is due to the confinement of phonon modes from the centre of the mini-Brillouin zone. This effect was not observed in a 10 period SL with the same nominal growth properties due to the lack of confinement in the short SL structure.

The size of the approximately 2 ns width peak was investigated as the laser beam generating the acoustic wavepacket was tracked across the Al film behind the device. The spatial range over which this peak was present provides evidence that this extra peak is caused by coherent phonons and distinguishes it from the longitudinal heat pulse.

The 2 ns width peak and both of the heat pulses also present were observed for a range of applied bias and incident laser power. These are discussed later in the chapter, taking into account the presence of confined modes within the superlattice. These results are also compared to previous work on similar superlattice structures.

## 5.1 Background of superlattices

Semiconductor superlattices are structures comprised of alternating layers of semiconductor materials with different properties, as illustrated in figure 5.1. This artificial periodicity is much larger than the atomic spacing and this leads to the formation of new periodic potentials within the material [108]. The artificial periodicity is of great interest scientifically as it causes fundamental changes to both the acoustic and electronic properties of the structure compared to those in bulk materials.

There are different methods of creating an artificial periodicity in semiconductor samples, either by changing the doping density of the material or by using two different materials that have different properties. In this work the superlattices were created with alternating layers of GaAs and AlAs, which is a commonly used material system for these types of device. These two semiconductor materials have different band gaps and different acoustic impedances. One property that does not differ greatly between GaAs and AlAs is the lattice spacing, and this allows good-quality lattice-

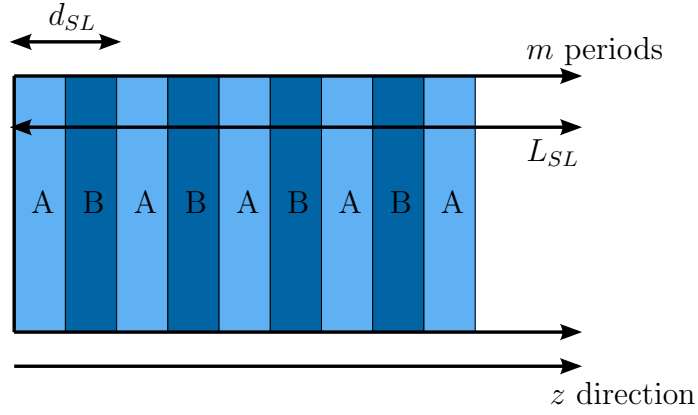


**Figure 5.1:** Schematic diagram of a superlattice structure. Alternating layers of two materials A and B are stacked in the growth direction  $z$ . The superlattice period  $d_{SL}$  is the artificially imposed period and a number of periods  $m$  make up the length of the superlattice  $L_{SL}$ .

matched structures to be grown by molecular beam epitaxy.

### 5.1.1 Electronic properties of superlattices

The difference in band gap between the GaAs and AlAs layers leads to a change in the band energies of the semiconductor structure. Alternating layers of AlAs and GaAs leads to the formation of a series of GaAs quantum wells separated by AlAs barriers and this new periodic band structure affects the electronic transport through the material.

The periodic square-well potential in the SL leads to the formation of minibands in the SL band structure, as illustrated for the case of a small applied bias in part a) of figure 5.2. This was theoretically presented by Esaki and Tsu in 1970 [109], and later demonstrated experimentally by Esaki and Chang [110]. Transport of electrons through the SL device occurs in the minibands for zero and small applied electric fields. The miniband width  $\Delta_m$  depends on the interwell coupling, with narrow minibands forming for weak coupling between wells.

The application of sufficient bias across the SL, and hence a large enough applied electric field strength, leads to a tilting of the band structure of the SL. This leads to the splitting of the QW energy levels, causing the

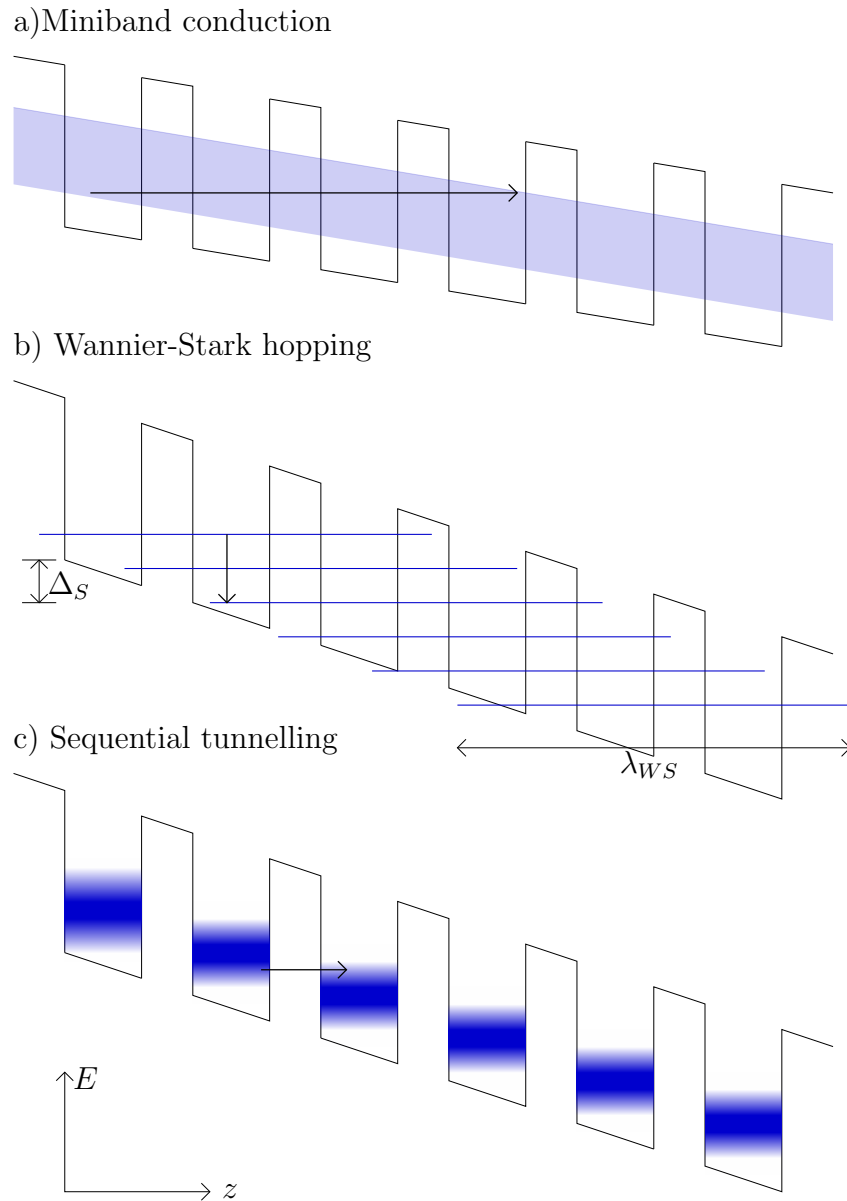


**Figure 5.2:** Different electron transport regimes in a semiconductor superlattice. The energy  $E$  is shown as a function of growth direction  $z$  for the 3 cases of a) miniband transport, b) hopping in a Wannier-Stark ladder and c) sequential tunnelling.  $\Delta_S$  is the Stark splitting and  $\lambda_{WS}$  is the Wannier-Stark localisation length.

minibands to be destroyed. Electron transport in the SL must then occur by a different mechanism. The electron transport at larger applied bias can fall into one of two different regimes: hopping in a Wannier-Stark ladder or sequential tunnelling. These are shown schematically in parts b) and c) of figure 5.2. Which regime a particular superlattice falls into depends on the properties of the superlattice layers such as the coupling between wells, the applied electric field and the scattering rates within the wells.

In the Wannier-Stark regime the application of bias across the superlattice leads to the localisation of the electron states on a scale of  $\lambda_{WS} \sim \Delta_S/eF$ , where  $\lambda_{WS}$  is known as the Wannier-Stark localisation length,  $\Delta_S$  is the Stark splitting, and  $F$  is the applied electric field strength [108]. For moderate electric fields the localisation can be spread over a few periods of the SL, but for high fields the electronic states are strongly localised in a single quantum well. Transport through the SL is then due to the hopping of electrons between different wells via the absorption or emission of a phonon [111].

In the sequential tunnelling regime there are typically thick barriers between the quantum wells, with sufficiently low coupling between adjacent wells that they can be considered as separate quantum wells. Electron transport occurs via tunnelling through the barriers, which can be phonon-assisted [111]. The energy states in the wells are often broadened due to scattering.

It is not always clear in the literature which regime applies in a given situation. Wacker and Jauho developed a quantitative theory to describe all three regimes of electrical transport in a superlattice described in this section [112,113]. They developed a full quantum transport theory based on nonequilibrium Green's functions that led to a result that could be simplified to agree with each of the three regimes in different limiting cases.

The different regimes of transport in a superlattice have also been discussed at length by Bonilla and Grahn [114], who made a distinction between weakly and strongly coupled superlattices. For weakly coupled SLs the widths of the barriers between wells are much larger than the electron wavefunction inside the barrier and the electronic properties can be thought of in terms of the sub-band structure of isolated wells and resonant

tunnelling across the barriers. For strongly coupled SLs the barriers are thin and the electronic properties are described by extended states. Bonilla and Grahn argue that any weakly coupled superlattice is in the sequential tunnelling regime.

### 5.1.2 Acoustic properties of superlattices

The artificial periodic structure of the superlattice also leads to a change in the dispersion of acoustic phonons travelling through the structure. Bragg reflections occur, due to the alternating acoustic impedances of the two different materials [59].

The condition required for Bragg reflections is given by

$$m\lambda = 2d_{SL}\cos\theta \quad (5.1)$$

where  $\lambda$  is the phonon wavelength,  $d_{SL}$  is the superlattice period,  $\theta$  is the angle of incidence of the phonons measured from the normal of the interfaces and  $m$  is an integer. Phonons that satisfy this condition are reflected in an ideal superlattice, and dips in the transmission of high-frequency phonons in superlattices have been observed experimentally since 1979 [115].

The artificial periodicity caused by the alternating layers on a scale larger than the atomic spacing also leads to the folding of the acoustic phonon dispersion curve into a mini-Brillouin zone, as demonstrated in figure 5.3 [59]. Bragg reflections within the superlattice structure cause energy gaps known as “stop bands” to open up at the mini-zone centre and edge boundaries, with phonon wave vector  $q = 0$  and  $q = \pi/d_{SL}$ , respectively. These folded-phonon modes are of great interest and have been the subject of numerous studies over the years [23, 49, 50, 116].

### 5.1.3 Applications

Semiconductor superlattices have been used in a variety of different applications in the field of terahertz acoustics. They can be used as acoustic transducers that are capable of generating high-frequency narrow-band

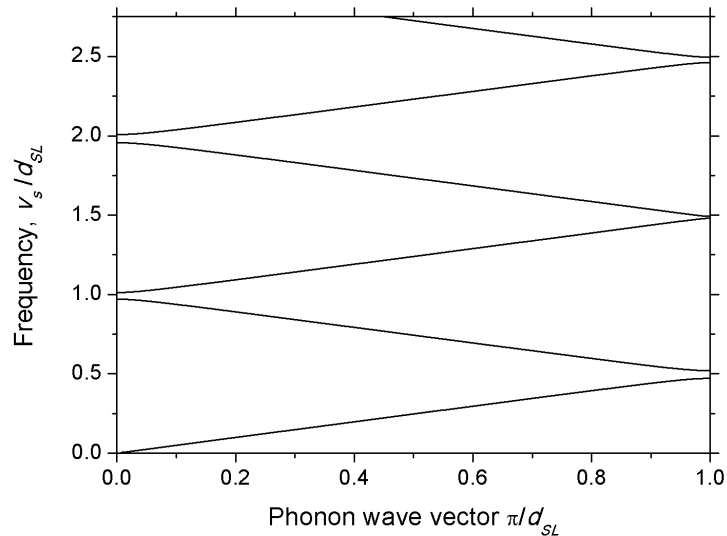


**Figure 5.3:** Folded acoustic phonon dispersion for a semiconductor superlattice. Stop bands open up at the zone centre and edge due to Bragg reflections within the structure.  $v_s$  is the speed of sound in the superlattice and  $d_{SL}$  is the superlattice period.

acoustic wavepackets and also as receivers that detect acoustic signals in a sensitive and frequency selective manner [49]. Filters for acoustic frequencies can also be formed from SLs due to the Bragg reflections of certain frequencies based on the periodicity of the structure [115]. These Bragg mirrors formed from SLs have been used to form acoustic cavities that allow the study of other acoustic phenomena within the cavity [117].

One interesting application of superlattices in terahertz acoustics is in the development of a SASER device, the acoustic analogue of the laser, which uses sound amplification due to the stimulated emission of acoustic radiation. It has been shown that sound amplification is indeed possible in a semiconductor superlattice with the appropriate parameters under an applied bias [29, 118]. Detailed discussions can be found in other works dedicated to this area [119, 120].

Semiconductor superlattices have also been used in several applications relating to terahertz electromagnetic signals. It has been demonstrated that they can be used as millimeter-wave oscillators and amplifiers with frequencies up to 70 GHz [121]. They have also been used as frequency

multipliers, with frequency doubling and tripling of terahertz radiation observed in SL structures [122]. It is also possible to use SLs as detectors of terahertz radiation pulses [123].

## 5.2 Device structures

Two wafers grown using molecular beam epitaxy (MBE) at the University of Nottingham were used in the following experiments. Both samples contained a GaAs/AlAs superlattice (SL) with 3.9 nm thick AlAs barriers and 5.9 nm thick GaAs wells, but the number of periods of the SL differed between the two samples. The device structures for the two types of device are shown in figure 5.4. Initially, a 500 nm thick  $n$ -doped GaAs layer ( $n = 2 \times 10^{18} \text{ cm}^{-3}$ ) was grown on top of a semi-insulating GaAs substrate to form the bottom contact layer. This was followed by a 20 nm undoped GaAs spacer layer before the SL was grown with an appropriate number of periods doped at  $2 \times 10^{16} \text{ cm}^{-3}$ . NU1727 contained a 50 period SL, while NU1778 contained a SL with only 10 periods. The SL was followed by another undoped spacer layer and a final  $n$ -doped layer with  $n = 2 \times 10^{18} \text{ cm}^{-3}$  to form the top contact layer.

The undoped spacer layers were included to separate the high doping concentration in the contact layers from the low doped SLs. In practise this region had a graded doping so as not to act like a capacitor.

These samples were etched to the bottom contact layer to create cylindrical mesas, and ohmic contacts were formed to both the top and bottom contact layers. A microscope image of the NU1727 sample is shown in figure 5.5. The mask set used creates cylindrical mesas of different sizes. The top contacts have a horse-shoe shape to allow optical access to the semiconductor for experiments that require it, while the back contact is a large grid common to all devices.

As the substrates had been mounted in the MBE machine using indium during the growth process, the back surface of the substrate had to be polished to remove contamination and provide an optically flat surface to work with. Aluminium films with thicknesses ranging from 30 nm to

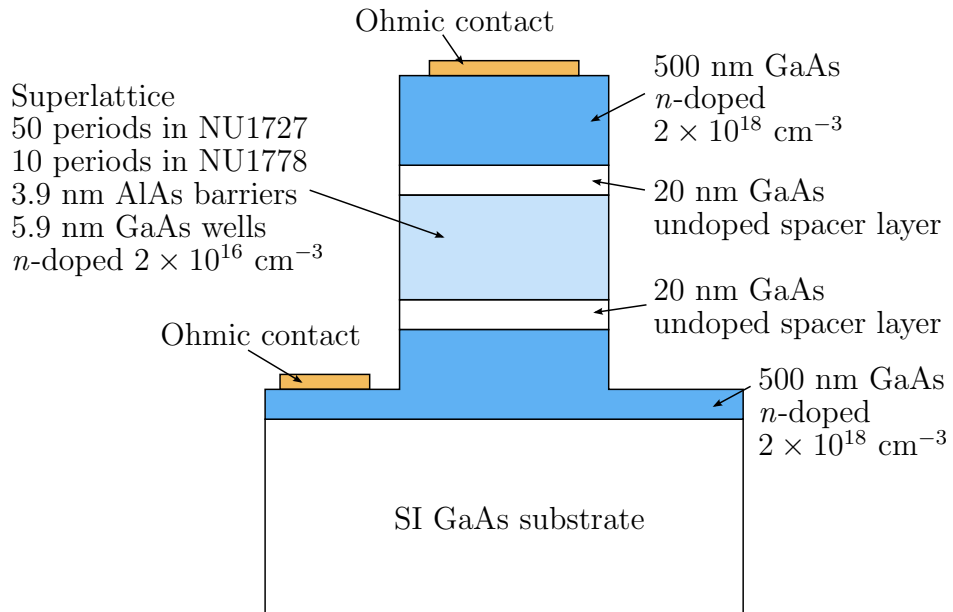


**Figure 5.4:** Schematic diagram of superlattice devices fabricated from the NU1727 and NU1778 wafers. Both structures contained a superlattice with 3.9 nm AlAs barriers and 5.9 nm GaAs wells. The NU1727 wafer had a 50 period superlattice, while the NU1778 wafer had only 10 periods. Both were fabricated into cylindrical mesas with ohmic contacts formed to the two  $n$ -doped contact layers. Undoped spacer layers were included to separate the high doping concentration in the contact layers from the low doped superlattice.

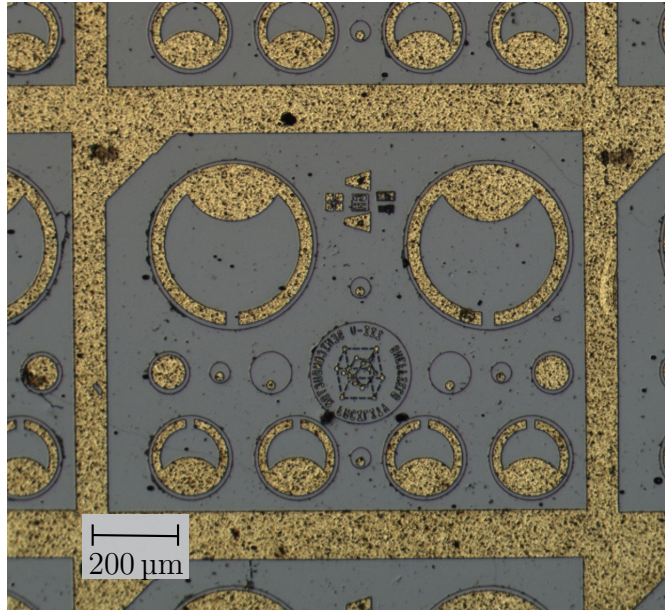


**Figure 5.5:** Microscope image of superlattice devices fabricated from the NU1727 wafer. Cylindrical mesas were etched from the material to form the devices. Horse-shoe shaped ohmic contacts were formed to the tops of the mesas while a larger grid-style back contact was formed to the bottom contact layer.

300 nm were thermally evaporated onto the back of the samples.

## 5.3 Electrical measurements of acoustic signals in 50 period superlattice samples

### 5.3.1 Device characterisation

#### I-V characteristics

The current-voltage (I-V) characteristics of the 50 period NU1727 superlattice were investigated using the standard method described in section 3.2, in which a voltage was applied to the device via a series resistor and the current through the device was determined from the voltage measured across the resistor. Throughout the following experiments, several different Al films with different thicknesses were thermally evaporated onto the back

surface of the sample for use as acoustical transducers. For each new Al film the SL device had to be electrically connected to the sample holder with Al wire. Initially the same SL device was disconnected and reconnected to make a direct comparison of the different Al films. Later, it was not possible to use exactly the same SL device due to damage to the sample, so the nearest neighbour devices were used to minimise any differences caused by variations in the semiconductor wafer or the processing of the devices. The I-V characteristics were then compared in each case, as shown in figure 5.6, to ensure that the devices bonded were comparable. 200  $\mu\text{m}$  diameter mesas were used for the following experiments.

Devices fabricated from this wafer have previously been used to investigate acoustic phonon-assisted tunnelling in SLs [51], and later sound amplification in SLs [29, 119]. The I-V characteristics shown in figure 5.6 agree closely with those observed in these previous studies. Small variations in the I-V characteristics between devices made at different times can be expected due to differences in the processing, such as contact formation.

For low applied bias, up to  $\approx 50$  mV in both directions, there is negligible current flow through the SL. Once the applied bias exceeds 50 mV a current is seen to flow, and the current increases with increasing applied bias. This threshold voltage,  $V_T$ , corresponds to the bias required to align the Fermi energy of the emitter with that of the nearest quantum well [51]. The I-V characteristics then become asymmetric, with the current in the device becoming self limiting at different biases in the forward and reverse directions. It has been suggested that this difference is due to the difference in the device contacts as the one on top of the mesa is small relative to the large back contact, as shown in the microscope image in figure 5.5.

At high applied bias, a plateau is seen to form in the forward bias direction for  $V > 610$  mV, while several peaks are observed in the negative bias direction for  $V < -240$  mV. These effects are both due to the formation of electric field domains of significantly different electric field strengths that are separated by a region of space charge [108, 110]. The series of peaks in the reverse directions is caused by the formation and expansion of stable domains [51]. If the space charge present is not sufficient to form stable domains, domains with unstable boundaries can be formed that propagate through the SL causing oscillating currents. This leads to a plateau in the

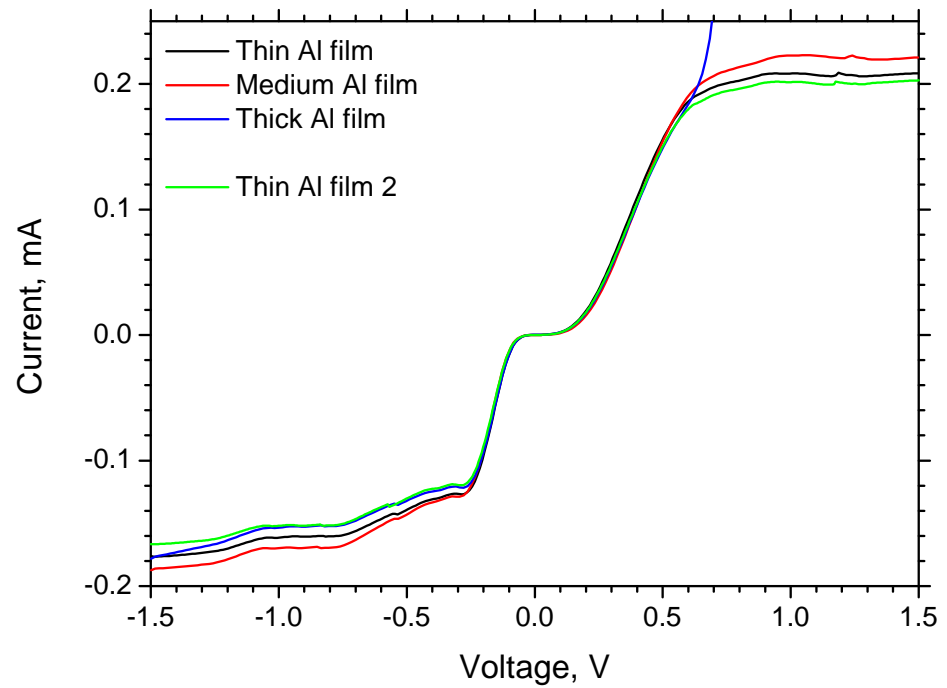


**Figure 5.6:** I-V characteristics of the 50 period superlattice sample NU1727 for the various devices used for the different Al film thickness measurements. The four devices behave the same in the range of interest, with a threshold at low biases before the current increases with increasing applied bias. At larger biases the current plateaus due to the formation of electric field domains within the SL.

I-V characteristics as observed in the forward bias direction. The formation of the domains does not occur in a reproducible way, as seen by the small variations between the four curves in figure 5.6. For this reason, the experiments were performed in the predictable range between -0.2 V and 0.5 V.

The characteristics of the device used in the thick Al film experiments deviates from the others at positive biases above 0.6 V. This is possibly due to damage caused during the wedge bonding of the device. However, as this occurs in the charge domain regime of the I-V characteristics this falls outside the region of interest and should have no further consequence on the experiments.

### Calculated acoustic phonon dispersion

The dispersion of acoustic phonons within superlattices has previously been calculated using several different models. One commonly used model is the Rytov model, which is an elastic continuum model that considers alternating layers of two isotropic substances and was used long before the introduction of semiconductor superlattices [124]. This model was chosen by Beardsley in previous work on the same superlattice wafer for the ease of calculations [119]. As only the longitudinal acoustic modes were required, it was considered unnecessary to spend time using other more complicated models to also recreate the dispersion relationships for the transverse acoustic and the optical modes.

The equation for the dispersion of longitudinal acoustic phonons in a semiconductor superlattice obtained using the Rytov model, as given by Tamura *et al.*, is

$$\cos(qd_{SL}) = \cos\left(\frac{\omega d_A}{v_A}\right) \cos\left(\frac{\omega d_B}{v_B}\right) - \frac{1 + \delta^2}{2\delta} \sin\left(\frac{\omega d_A}{v_A}\right) \sin\left(\frac{\omega d_B}{v_B}\right) \quad (5.2)$$

where  $q$  is the phonon wave vector and  $\omega$  is the phonon angular frequency [59]. The superlattice period  $d_{SL} = d_A + d_B$ , where  $d_A$  and  $d_B$  are the thicknesses of the two different layers. The constant  $\delta = \rho_A v_A / \rho_B v_B$  is the ratio of the acoustic impedances with  $\rho_{A,B}$  and  $v_{A,B}$  the densities and sound velocities in layers A and B, respectively.

**Table 5.1:** Layer parameters used to calculate the phonon dispersion for the NU1727 superlattice, as given in reference [119].

Material	Layer width	Sound velocity	Elastic constant
GaAs	5.9 nm	4750 ms <sup>-1</sup>	11.90×10 <sup>10</sup> Nm <sup>-2</sup>
AlAs	3.9 nm	5646 ms <sup>-1</sup>	12.02×10 <sup>10</sup> Nm <sup>-2</sup>

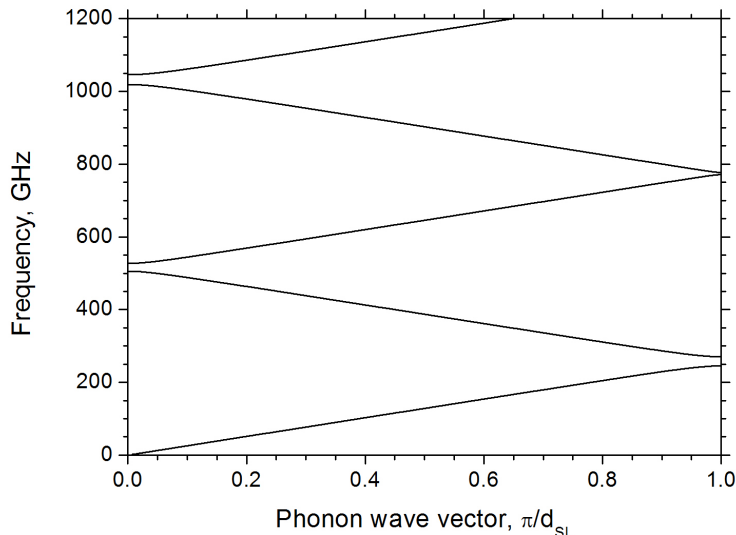


**Figure 5.7:** Calculated longitudinal acoustic phonon dispersion for the NU1727 superlattice. A folded dispersion relationship was calculated using the Rytov model [124] and the parameters in table 5.1 as given by Beardsley [119]. Stop gaps open up at the mini-zone edge and centre in the frequency ranges 246-270 GHz and 505-527 GHz, respectively.

The dispersion of the LA phonons has been calculated for the NU1727 sample using equation 5.2 and the parameters given in table 5.1 as used by Beardsley. This calculation produced the folded dispersion relation shown in figure 5.7. A mini-Brillouin zone is formed and stop gaps open up at the mini-zone edge and centre where  $q = \pi/d_{SL}$  and  $q = 0$ , respectively. The two lowest frequency stop gaps are at frequencies of 246-270 GHz at the mini-zone edge and 505-527 GHz at the zone centre.

As the Rytov model uses an elastic continuum approach, it produces a continuous dispersion curve. However, the discrete nature of the superlattice leads to a quantisation of the dispersion not shown by this calculation. This quantisation leads to a series of discrete states that sit on the cal-

culated dispersion curve. The number of available states is linked to the number of periods in the superlattice.

The calculated dispersion curve will not necessarily completely agree with the observed phonon modes. The calculation assumes the properties of an ideal superlattice and the thickness of the layers grown by MBE can deviate from the nominal values. A change in 10% of the thickness of the SL layers can lead to a shift in the stop gap frequencies of approximately 10%. The calculation does, however, give a good indication of the frequency range in which the stop gaps can be expected to occur.

### 5.3.2 Acoustic signal with a thin Al film transducer

The superlattice sample initially had a thin ( $\approx 30$  nm thick) Al film thermally evaporated onto the back of the substrate to function as a transducer for acoustic signals. The 800 nm wavelength laser pulses were focussed onto the Al film and a broad frequency acoustic pulse was launched into the sample. The generation of coherent acoustic phonons in thin Al films was described in section 2.1.1 and is well documented in the literature [1,3,8,44]. The acoustic wavepacket generated in the Al film then travelled across the GaAs substrate to the SL device. The change of voltage across the device was recorded on a 12.5 GHz bandwidth oscilloscope and is shown in figure 5.8. A bias tee and two 20 dB amplifiers were included to allow the application of a DC bias and the amplification of small signals.

The initial pulse is the optical breakthrough caused by the SL device directly responding to the incident laser light. This is quite long and followed by a large amount of ringing due to the thin Al film used as the transducer allowing a fraction of the light to pass through. The signal at  $t_0 = 76$  ns is the signal caused by the acoustic wavepacket reaching the SL for the first time after propagation across the GaAs substrate. The following peaks at  $2t_0$  time intervals are caused by multiple reflections of the acoustic wavepacket in the sample. It is not easy to determine  $t = 0$  from the optical breakthrough, but the very regular time intervals between reflections allows an accurate calculation of the time for the acoustic phonons to travel across the substrate. Using the speed of longitudinal acoustic phonons in GaAs of  $4780 \text{ ms}^{-1}$  [68] the thickness of the sample can be

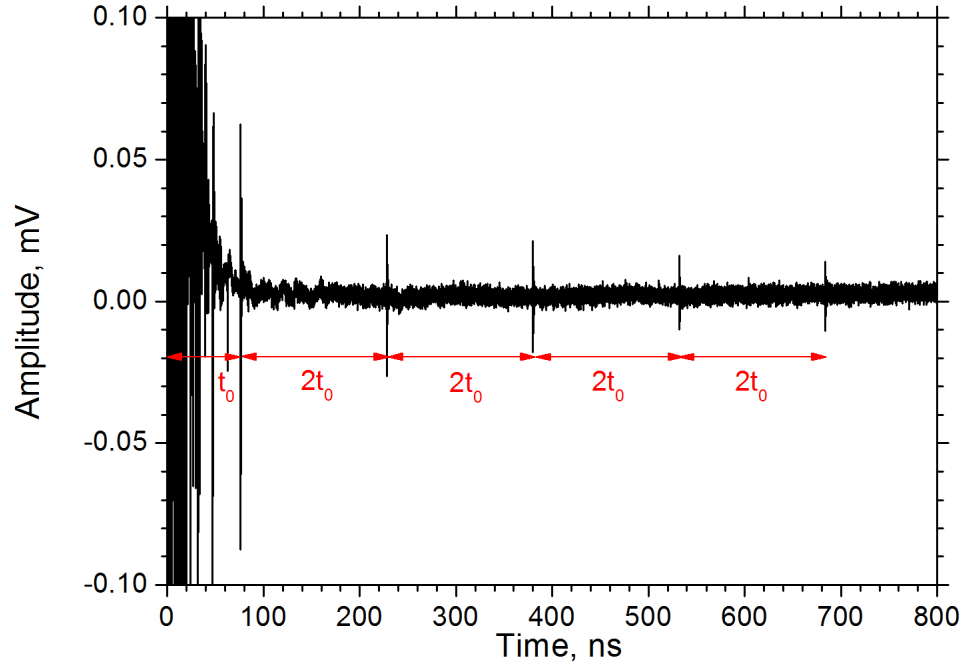


**Figure 5.8:** Acoustic signal detected by the 50 period superlattice sample NU1727. The initial large signal is the optical response due to a fraction of the incident laser light passing through the thin Al film used as the acoustic transducer. The following peaks are acoustic signals caused by multiple reflections of the acoustic wavepacket across the substrate of the sample.

calculated as  $363 \pm 1 \mu\text{m}$ .

The acoustic signal obtained when using a thin Al film transducer is shown in figure 5.9 for a range of applied bias. As the I-V characteristics in figure 5.6 are asymmetric, a different size applied bias is required in the forward and reverse directions to observe the same size effect on the acoustic signal. It is important for these experiments that the applied bias is not within the domains region of the I-V characteristics, as this can lead to large current oscillations that are not reproducible.

There are two distinct peaks observed in the voltage measured across the SL. The first pulse is the longitudinal acoustic (LA) phonon contribution at  $t = 76 \text{ ns}$ . The later peak is a heat pulse caused by transverse acoustic (TA) phonons. These transverse phonons have a speed of  $3340 \text{ ms}^{-1}$  in GaAs [125]. Using this speed and the thickness of the sample obtained

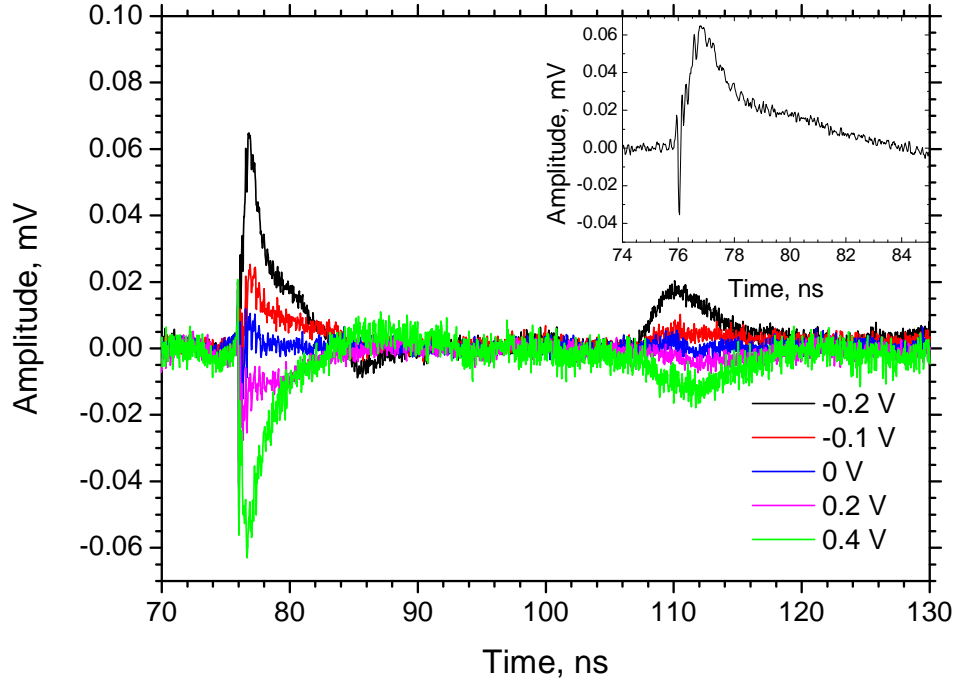


**Figure 5.9:** Acoustic signal detected by the 50 period superlattice sample NU1727 for a range of applied bias. The first peak is due to the longitudinal acoustic phonons and the later peak is a transverse heat pulse. The inset graph shows an expanded view of the first pulse for a single trace with -0.2 V bias applied to better display the initial fast part of the signal.

from the arrival time of the LA contribution, the TA heat pulse should arrive at the SL at  $t \approx 108$  ns, in good agreement with the time of the second peak in figure 5.9.

The inset graph provides a more detailed view of the initial peak caused by longitudinal acoustic phonons. At the very beginning there is a fast strain pulse component, which does not change in shape or magnitude with applied bias. This is followed by a rise in the voltage measured across the SL that forms a peak with a width of approximately 2 ns, followed by a slower decay tail. This 2 ns part is too slow for a typical strain pulse [1] and too fast to be a heat pulse, which is typically on the order of 10s of nanoseconds when generated with a very short laser pulse [51].

Applying a positive bias to the SL via the bias tee leads to a negative voltage response when the phonons are present at the SL. In comparison,

the application of negative bias leads to a positive response in the voltage across the SL. This trend is true for both the LA and TA contributions, as demonstrated in figure 5.9. Based on the electrical arrangement of the bias tee, SL device and oscilloscope the fact that the observed response has the opposite polarity to the applied electrical bias suggests that the resistance across the SL is decreasing in the presence of the incident phonons.

The electrical circuit for connecting the superlattice device, oscilloscope and bias tee is shown in figure 5.10. The bias tee equivalent circuit is shown in the box, and contains a capacitor ( $C_2$ ) and an inductor ( $L$ ) to block the DC bias from the oscilloscope and the high frequency signals (RF) from the DC power supply.  $R_{\text{scope}}$  is the input impedance of the oscilloscope and this was set at  $50 \Omega$  for these experiments.  $R_{\text{dev}}$  is the resistance of the SL device, and  $C_{\text{dev}}$  is the parasitic capacitance of the device. The parasitic capacitance of the oscilloscope can be neglected, as the impedance of the oscilloscope is small, even at high frequencies. This circuit can be simplified for the DC and high frequency cases, as illustrated by the equivalent circuits given in figure 5.11. These were obtained using the following expressions for the reactance of the inductor and the capacitors

$$X_L = 2\pi fL \quad (5.3)$$

$$X_C = \frac{1}{2\pi fC} \quad (5.4)$$

where  $X_L$  and  $X_C$  are the reactances of the inductor and capacitor, respectively,  $f$  is the frequency,  $L$  is the inductance and  $C$  is the capacitance.

Part a) of figure 5.11 shows the equivalent circuit for the DC case. When  $f = 0$ ,  $X_L \rightarrow 0$  and  $X_C \rightarrow \infty$ . The impedance of the decoupling capacitor  $C_2$  becomes very large and prevents any DC voltages from entering the oscilloscope. The impedance of the inductor becomes small enough to be ignored. A change in the resistance of the device would lead to a change in the current flowing through it, but the voltage across the oscilloscope would remain constant. The parasitic capacitance of the device,  $C_{\text{dev}}$ , can also be ignored, as the impedance becomes very large and the current preferentially flows through the SL device. Considering only DC voltages is not realistic as the transient phonon wavepacket will cause high frequency changes to the superlattice properties.

The high frequency case shown in part b) of figure 5.11 is of greater in-

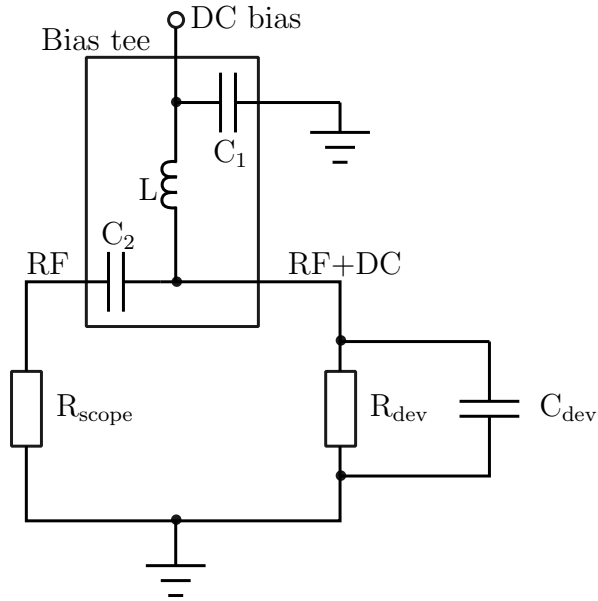


**Figure 5.10:** Electrical circuit connecting the superlattice device to the oscilloscope via the bias tee. A capacitor  $C_2$  and an inductor  $L$  within the bias tee block the DC bias from the oscilloscope and the high frequency signals (RF) from the DC power supply.  $R_{\text{dev}}$  represents the device resistance and  $R_{\text{scope}}$  represents the resistance of the oscilloscope, which was set at  $50 \Omega$ .  $C_{\text{dev}}$  represents the parasitic capacitance of the device.

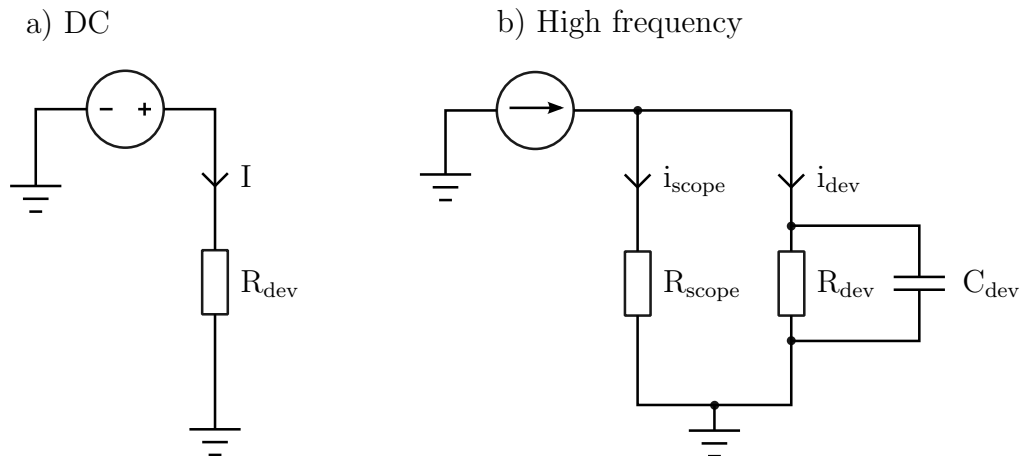


**Figure 5.11:** Equivalent circuits for the ideal electrical set-up for the DC and high frequency cases. The DC case is not very interesting as a change to the device does not affect the oscilloscope. The high frequency case is more applicable, and a change in the resistance of the superlattice will affect the voltage measured with the oscilloscope.

terest here, as it is more applicable. For high frequencies, when  $f$  is large,  $X_L \rightarrow \infty$  and  $X_C \rightarrow 0$ . The inductor then has a very large impedance and effectively behaves as a constant current source. For large enough frequencies the constant current tends towards zero current. The impedances of the capacitors  $C_1$  and  $C_2$  become small enough that they can be treated as short circuits, and the device and the oscilloscope are then connected in parallel. The currents through the device and the oscilloscope are linked in the equation

$$i_{dev} + i_{scope} = 0 \quad (5.5)$$

where  $i_{dev}$  and  $i_{scope}$  are the currents through the device and oscilloscope, respectively. As the device and oscilloscope are in parallel with one another, the same voltage drop must be present across the two of them. The parasitic capacitance of the device can be important at high frequencies as it will have a low impedance.

For the high frequency case, if a change in the resistance of the superlattice device occurs it will have an affect on the voltage seen across the oscilloscope. If the superlattice resistance  $R_{dev}$  decreases, as proposed, this would lead to a negative change in the voltage across the SL device and so a negative change in the voltage seen on the oscilloscope. This agrees with the experimental observations and confirms that the resistance of this superlattice decreases in the presence of the incident phonon wavepacket.

### 5.3.3 Comparison with other film thicknesses

These measurements were repeated for two other Al film thicknesses – 100 and 300 nm. The frequency spectrum of the broad acoustic wavepacket generated in the Al film is dependent on the film thickness. Thin films are required to generate acoustic pulses with the highest frequency components as the broadening caused by hot electron diffusion is limited [3]. The thicker films used in these measurements will generate fewer high frequency components compared to the thin film used initially.

A comparison of the detected signal for the 3 different thickness Al films is shown in figure 5.12, for an applied bias of -0.2 V. The data is quite noisy as the signal is very small, leading to a poor signal-to-noise

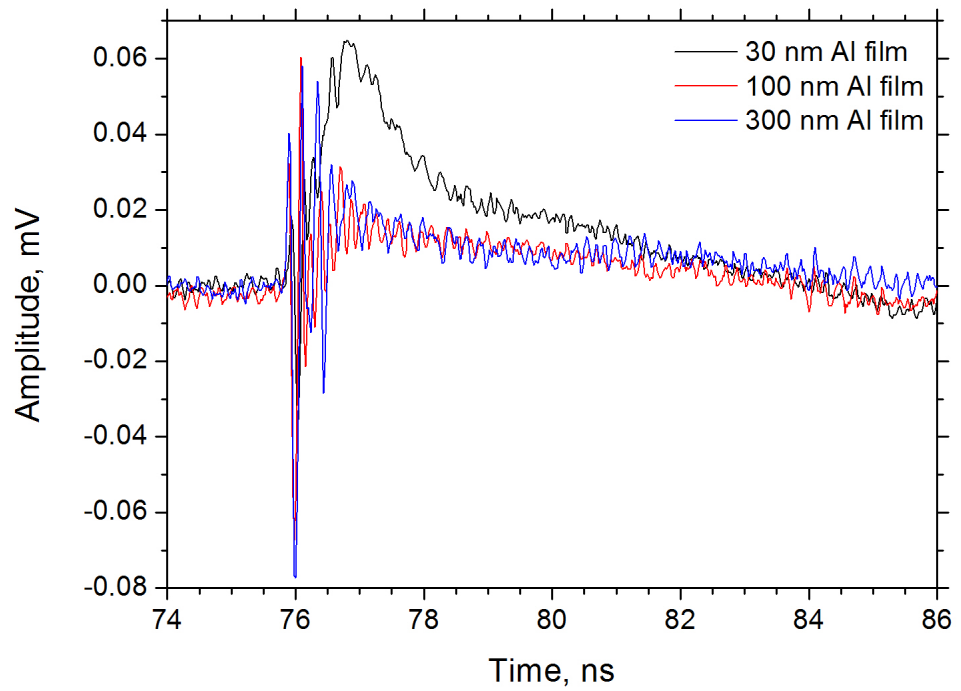


**Figure 5.12:** Effect of Al film transducer thickness on the acoustic signal detected by the 50 period superlattice sample NU1727 with -0.2 V bias applied. Three different Al film thicknesses were investigated and an extra contribution to the signal is observed for the thin Al film compared to the two thicker films.

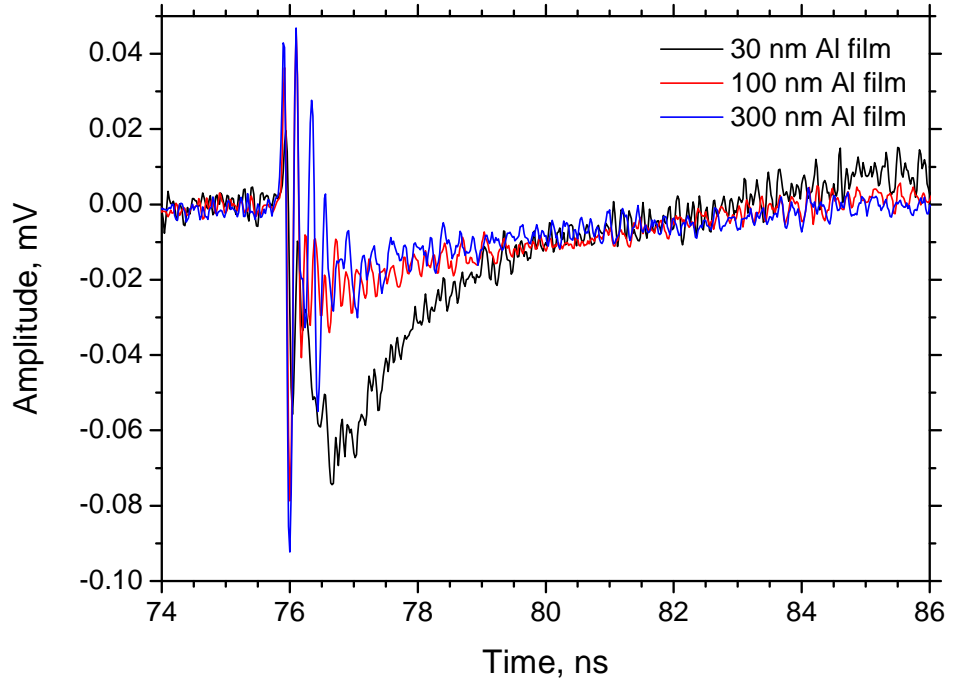


**Figure 5.13:** Effect of Al film transducer thickness on the acoustic signal detected by the 50 period superlattice sample NU1727 with 0.5 V bias applied. Three different Al film thicknesses were investigated and an extra contribution to the signal is observed for the thin Al film compared to the two thicker films.

ratio. This signal has been obtained by averaging the traces from many laser pulses, and a background signal taken with the laser beam blocked has been subtracted for clarity of the laser induced effects. All three traces have a very similar initial fast strain pulse part such that the three curves are almost indistinguishable on the graph. The curves for the two thicker Al films appear to agree quite closely with one another over the whole time range, while the thin Al film signal has an additional contribution in the form of a larger amplitude but shorter duration peak. This additional peak does not rapidly increase at  $t = 76$  ns with the initial fast strain pulse; it instead has a slower build-up over approximately 0.5 ns.

The same effect is also observed for positive applied bias, as demonstrated in figure 5.13. The two thicker Al films lead to a very similar transient change in the voltage across the SL, whereas the signal for the thin Al film transducer is quite different. The two biases chosen were both

large enough to give a noticeable effect due to the application of an external bias, but small enough to have not entered the electric field domain region of the I-V characteristics in figure 5.6. As these characteristics are asymmetric a different magnitude bias must be applied in the forward and reverse directions to achieve a similar size effect.

For all applied biases, little effect was seen on the size or shape of the TA heat pulse signal at  $t = 108$  ns for strain generation in the 3 different Al film thicknesses. This suggests that this extra contribution is due to an effect that involves only the LA phonons detected in the initial pulse and not the incoherent TA phonons.

The proposed cause of this extra contribution observed only in the case of the thin Al film is confinement of particular long-lived phonon modes in the superlattice. The confined phonon modes present in this SL structure were investigated previously by optical pump-probe techniques by Beardsley *et al.* [50]. Phonon modes corresponding to the centre and the edge of the mini-Brillouin zone were observed in this work at frequencies of approximately 450 GHz and 240 GHz, respectively. The Brillouin backscattering mode was detected at 45 GHz.

Normally, the experimentally observed modes are those with phonon wave vector  $q \leq 2k$  where  $k$  is the photon wave vector in the SL, as these modes satisfy the conditions for momentum conservation in the photon-phonon interactions. The photon momentum is defined as  $\mathbf{p}_{\text{photon}} = \hbar\mathbf{k}$  and the crystal momentum for the phonon is given by the expression  $\mathbf{p}_{\text{phonon}} = \hbar\mathbf{q}$ . This condition tends to mean that only modes near the mini-zone centre are detected. Those modes near the mini-zone edge with  $q > 2k$  are not typically expected to be observed in optical pump-probe experiments as they do not conserve momentum in these interactions. However, in the work by Beardsley the zone-edge mode was observed and it was proposed that the presence of free carriers due to the intentional doping with Si allowed momentum to be conserved.

The initial strain pulse propagating through the sample would contain frequency components at the frequencies of the confined modes, and these phonons would be trapped due to Bragg reflections within the structure. As this is a finite SL structure with imperfect layers these phonons do escape

over time. The lifetime of the modes observed by Beardsley are on the right time scale for the  $\approx 2$  ns width additional peak. The backscattering Raman mode is expected to escape from the SL in approximately 200 ps but the lifetimes of the zone centre and edge modes are in the 1-2 ns range.

These zone edge and centre modes are at the high frequency end of the acoustic spectrum generated in an Al film transducer. For the thin Al film transducer there would be a component present in the generated acoustic wavepacket at these frequencies. However, when using the medium or thick Al film transducers those frequency components would be strongly reduced or entirely absent. This is consistent with the fact that the effect is only observed when using the thin Al film.

### 5.3.4 Position dependence

The size of the peak in the signal caused by the longitudinal phonons was investigated for different positions of the incident laser spot relative to the superlattice device for the case of the thin Al film transducer. The acoustic signal was generated in the Al film and the transient voltage changes across the SL were detected by a fast oscilloscope, as in the previous experiments. The signal on the oscilloscope was adjusted to find the maximum by moving the sample relative to the laser beam, and this position of maximum signal was defined as position zero. The laser beam was positioned such that it was incident upon the Al to one side of the mesa of interest, as shown in figure 5.14, and then the laser spot was moved laterally across the sample in the  $x$  direction to traverse the Al film behind the mesa. A series of data was recorded that shows the voltage measured across the SL for a range of positions of the laser spot relative to the device.

The area under the curve was integrated over different time windows to give a quantifiable measure of the size of the signal as a function of position, and two of these relationships are shown in figure 5.15. The time windows used are marked on the schematic diagram of a typical response shown in the inset graph; these were chosen to determine if there was a different spatial dependence for the 2 ns width peak and the slower decaying tail. The amplitudes of the integrated areas are scaled to make direct comparison of the two curves easier by eye.

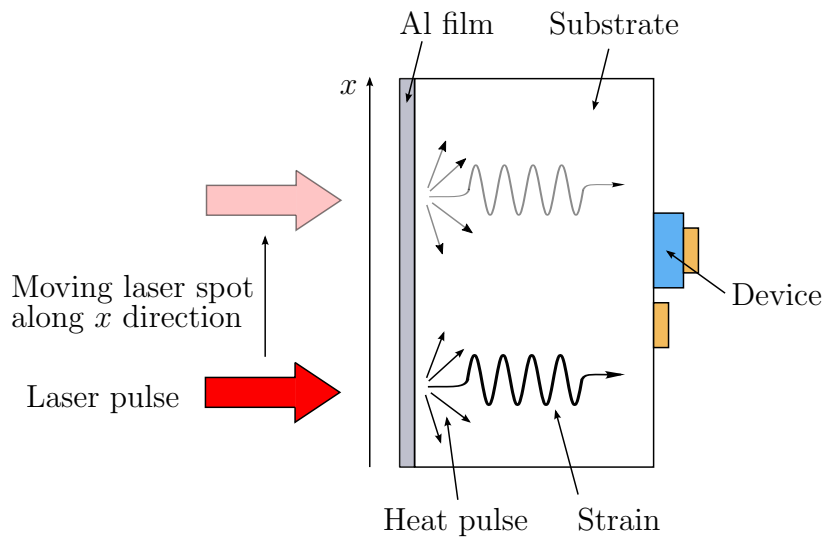


**Figure 5.14:** Schematic diagram of the position dependence experiment. A laser was used to generate an acoustic pulse in the Al film, which then travelled across the substrate of the sample. Coherent strain pulses propagate directly across the substrate in a narrow collimated beam, while incoherent heat pulses are emitted isotropically from the source. The laser beam was moved in the  $x$  direction across the Al film directly opposite the device of interest and the transient voltage changes across the device were recorded for each laser spot position.

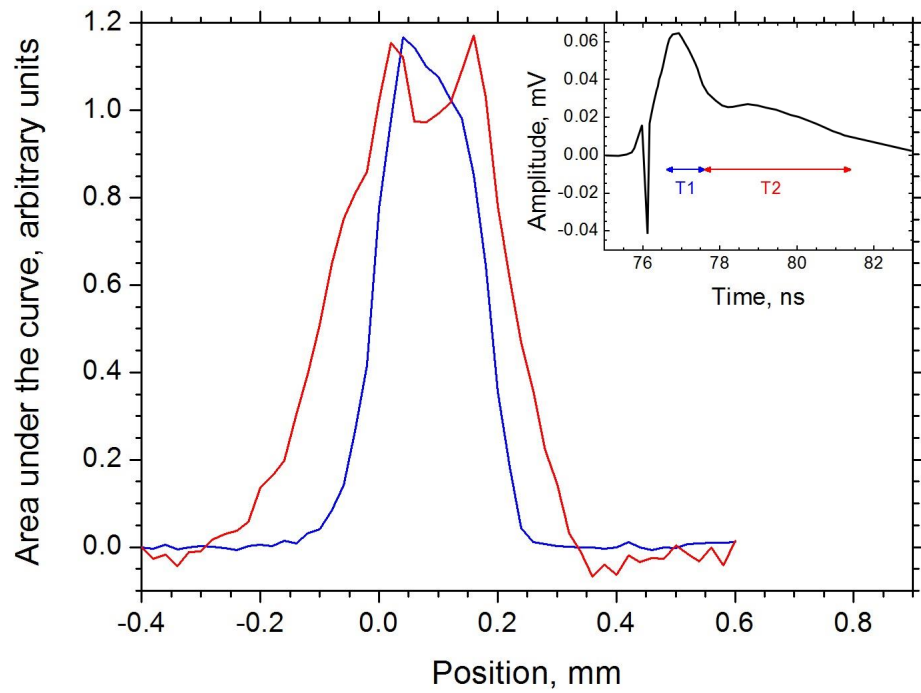


**Figure 5.15:** Position dependence of the longitudinal acoustic peak in the NU1727 signal for the thin Al film. The area under the curve was integrated for the two different time windows T1 and T2 shown in the inset graph on a schematic representation of the temporal response. The earlier part of the peak in the temporal response occurs over a smaller spatial range than the later part of the peak. The region of slower decay later in the temporal response exhibits a double peak behaviour in the spatial domain.

The earlier time window, T1, was intended to cover the 2 ns width peak only present in the thin film traces. This part of the peak has a spatial dependence with a well defined peak corresponding to when the laser spot was incident on the Al film behind the device. It has a width of 200  $\mu\text{m}$ , which is the same size as the diameter of the mesa chosen. This suggests that this is due to coherent phonons as they travel directly across the GaAs substrate to the device in a narrow collimated beam [42].

The later time window, T2, covers the slower decaying tail to see how the spatial dependence of this part differed from the 2 ns part of the peak proposed to be due to the confinement of certain phonon modes within the SL. The spatial dependence of this part of the signal also has a peak with the same centre as that for T1 but a larger width of 310  $\mu\text{m}$ . This is larger than the 200  $\mu\text{m}$  diameter mesa of the SL device. This would be consistent with the slow tail response being caused by incoherent phonons, which are emitted isotropically from each point of the source [42].

With the earlier part of the peak occurring over a smaller spatial region than the later part of the peak, it is proposed that the earlier part is due to coherent phonons while the later part is due to incoherent phonons, similar to previous work by Fowler *et al.* [42]. This is consistent with the suggestion that the 2 ns part of the peak is caused by phonons from the initial strain pulse that are trapped in the SL due to Bragg reflections. The slow decay following this is likely to be a longitudinal acoustic heat pulse. The heat pulse phonons experience dispersion and scattering as they propagate across the substrate and so they arrive at the device with a spread of times. The two effects are superimposed on top of one another to create the signal shape observed on the oscilloscope.

The later part of the signal (T2) also appears to show a double peak behaviour with position, whereas the earlier part (T1) only shows a single peak. This is further evidence that the later part of the peak is a heat pulse comprised of longitudinal acoustic phonons. The phonon focussing pattern for these phonons, while weak, is stronger at certain angles. The focussing effect peaks at  $40^\circ$  from the normal of the surface in [100]-oriented GaAs, which leads to a ring pattern over a 2D area [59]. A line scan taken through the phonon focusing results leads to a phonon intensity profile with a similar double peak behaviour. This result is not expected to closely match the

expected phonon focussing pattern as the phonon source, detector mesa and thickness of the substrate are all of comparable sizes, but certain positions of the laser spot relative to the detector device will still lead to an increased phonon intensity compared to other positions.

### **5.3.5 Comparison with a superlattice with only 10 periods**

The results presented so far were compared with those obtained from a different wafer (NU1778) that had a superlattice structure with the same nominal growth properties as NU1727 but only 10 periods instead of 50, which was shown schematically in figure 5.4. For a superlattice with only 10 periods, the confinement of modes within the structure will be poor.

The experiments performed on the 50 period SL were repeated using 200  $\mu\text{m}$  diameter devices fabricated from the 10 period SL wafer. The transient voltage across the device caused by an incident acoustic wavepacket was recorded for a range of biases and Al film thicknesses. The initial fast strain pulse component and the 2 ns width peak were not present for any thickness of Al film transducer, while both the LA and TA heat pulses were. This is consistent with the 2 ns width peak being caused by acoustic phonon modes confined within the 50 period superlattice structure, as the 10 period SL does not have a sufficient number of periods to lead to a strong confinement of modes.

## **5.4 Properties of the peak caused by confined coherent modes**

The response of the superlattice device to the incoming phonon wavepacket is comprised of several parts, as shown in figure 5.9. There is an initial fast strain pulse, a 2 ns width peak due to confined coherent phonons, a longitudinal acoustic heat pulse and a transverse acoustic heat pulse. The heat pulses will be considered in more detail in section 5.5, but for this section the focus will be on the peak caused by the confined coherent

phonon modes.

Over the course of the experiments, several different Al films with a range of thicknesses were deposited on the back surface of the substrate. Some of these Al film transducers led to a different sized heat pulse contribution in the SL response. One of the films that had a smaller heat pulse contribution was used for the following analysis. The analysis was performed on the earlier part of the peak, labelled as T1 in the spatial dependence data in figure 5.15, to avoid including the LA heat pulse.

### 5.4.1 Bias dependence

The response of the superlattice to the confined coherent phonon modes was investigated for a range of applied bias. The Al film on the opposite side of the substrate was excited with a femtosecond pulsed laser, in the same set-up as for the previous experiments. The bias was applied to the SL via a bias tee and the change in voltage across the SL device was recorded on an oscilloscope. To get a measure of the size of the detected signal for a given bias the area under the curve was integrated and this was plotted against the applied bias in figure 5.16.

A peak is clearly visible in the negative part of the bias range investigated, which is centred at approximately -0.18 V. It is proposed that the presence of this peak occurs when the applied bias leads to a Stark splitting of the energy levels in the superlattice that is resonant with one of the confined modes.

As the presence of the acoustic wavepacket travelling through the SL device leads to a reduction of the resistance of the device, as discussed in section 5.3.2, this means that there is an increase in current through the device when the phonons are present and therefore increased electron transport through the SL. As electron tunnelling through the structure is a phonon-assisted process [113], the presence of incoming phonons will trigger more electron hopping through the structure. This would be caused by phonons with a spread of frequencies, but it could be expected that this would be dominated by the phonons that are in resonance with the Stark splitting.

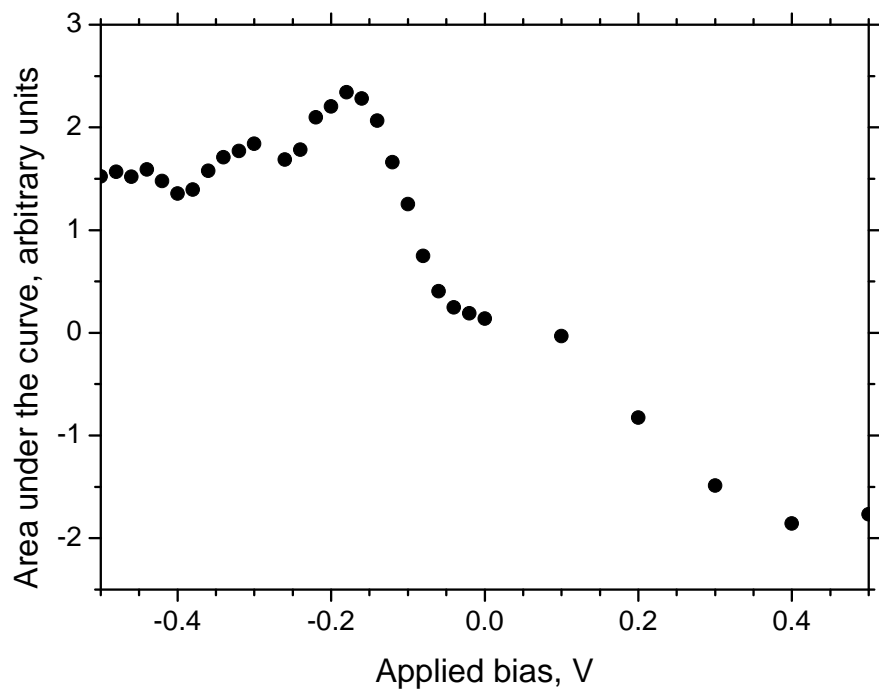


**Figure 5.16:** Bias dependence of the 2 ns part of the NU1727 signal caused by confined coherent phonons using thin film number 2. A clear peak is present at -0.18 V, with a possible negative peak at 0.4 V.

The Stark splitting  $\Delta_S$  can be estimated for a given applied bias  $V$  using the expression

$$\Delta_S = \frac{\Upsilon e(V - V_T)}{50} \quad (5.6)$$

where  $\Upsilon$  is the fraction of the applied bias that is dropped across the SL,  $e$  is the electronic charge and  $V_T$  is the threshold voltage determined from the I-V characteristics of the SL device. The division by 50 is due to the 50 periods in the superlattice.

It is difficult to accurately calculate the Stark splitting, as not all of the applied bias is dropped across the superlattice. There are several parts of the device that could contribute an additional resistance including bond wires, ohmic contacts, the thick doped contact layers and the undoped spacer layers within the structure. This leads to the inclusion of the pre-factor  $\Upsilon$  in equation 5.6.

From the I-V characteristics shown in figure 5.6, the threshold voltage  $V_T = 50$  mV. It is estimated that 70-80% of the applied bias is dropped over the SL itself. For an applied bias of -0.18 V, this leads to an energy level splitting that would be resonant with modes with a frequency in the range of 440-500 GHz.

Previous optical pump-probe experiments on this wafer detected zone-edge and zone-centre modes at 240 GHz and 450 GHz, respectively [50]. As 450 GHz falls within the frequency range estimated from the Stark splitting calculation, it then seems likely to be this zone-centre mode that is causing the peak observed in figure 5.21, with the fraction of the applied bias dropped across the SL  $\Upsilon$  close to 70%.

The peak is quite broad, with a width of 100 mV. The Stark splitting in the SL will not be perfectly defined due to broadening of the energy levels caused by scattering of electrons within the quantum wells. The confined mode would then be resonant with the energy level splitting over a range of applied bias and lead to a broader peak, as observed. The peak is also situated close to the rising edge and it is possible that the peak is not fully resolved from the initial rising edge.

The 450 GHz zone-centre mode is not the lowest frequency mode observed in this superlattice structure by optical pump-probe measurements,

yet the 240 GHz zone-edge mode does not appear to lead to any features in the bias dependence of the SL response to the incident strain pulse. It is likely that we are simply unable to resolve any effect caused by this mode. If the broadening of the energy levels is sufficiently great compared to the energy level splitting for this lower frequency mode, electron transport would occur through the SL at a similar rate for a range of applied bias without a distinct peak at a particular bias. Also, as any peak caused by this lower frequency mode would appear on the steeply rising edge in the bias dependence, it would be difficult to resolve. There is not enough resolution to observe the presence of a weak shoulder-type feature.

There is possibly also a peak for positive applied bias, but this is much less clear than for the case of negative bias and it occurs at a larger bias of 0.4 V. This reflects the fact that the I-V characteristic is strongly asymmetric; it is likely that in the forward bias direction less of the applied bias is dropped across the SL and it then requires a higher applied bias to form the same amount of energy level splitting.

It is important to note that this bias dependence does not simply follow the I-V characteristics of the device, or its derivative. The current threshold is still present, with no appreciable current flow at low applied bias, followed by an increase in current with increasing bias. However, the peak present on the negative bias side when the phonons are present does not correspond to a feature in the initial I-V characteristics, and so is an effect produced by the incident phonon packet.

An attempt was made to investigate the width of the peak in the temporal trace for different applied bias to look for any evidence of amplification of the confined phonons. This would lead to an increase in the width of the peak for certain applied bias as the phonon population within the SL structure would decay more slowly due to “feeding” of the mode by stimulated emission. However, the signal-to-noise ratio was poor and there was not sufficient resolution to determine if there was any change to the timing. This would be an interesting study to be performed as part of future work on this topic.

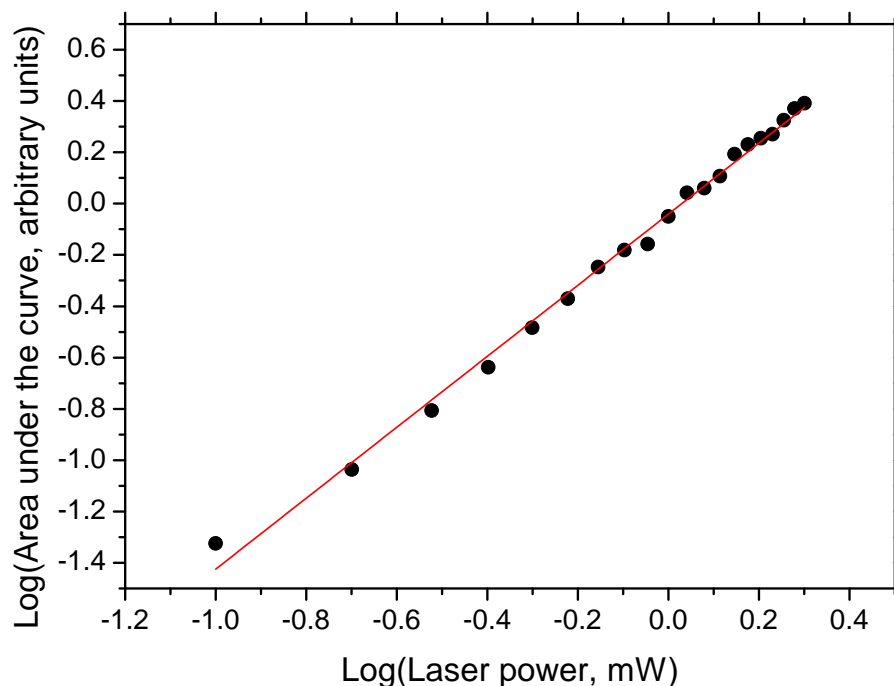


**Figure 5.17:** Laser power dependence of the 2 ns part of the NU1727 signal using thin film number 2. Logarithms of the data were taken to allow the power law to be determined from the gradient of the straight line fit made to the experimental data; a value of  $1.38 \pm 0.02$  was obtained.

### 5.4.2 Laser power dependence

The size of the signal caused by the confined coherent modes was also investigated for different laser powers incident upon the thin Al film transducer. The area under the curve was integrated to get a measure of the size of the signal for a range of laser power. To determine the power law, logarithms were taken of both the area and the laser power and these are plotted in figure 5.17.

The laser power dependence of the confined coherent modes is super-linear, falling somewhere between a linear relationship and a square law. Calculating the gradient of the linear fit to the log-log graph to determine the power law leads to a value of  $1.38 \pm 0.02$ .

Typically, when generating a strain pulse at low laser intensities the magnitude of the strain generated is proportional to the applied laser power.

At higher laser powers the generation becomes non-linear, but the laser powers used in this work are below this limit. It seems reasonable to assume that the observed non-linear effect is due to the response of the SL to the incident acoustic wavepacket.

### 5.4.3 Comparison to previous work

In recent work by Poyser *et al.* [53], a superlattice device with the same nominal growth structure but a higher doping density was seen to have an electronic response to a high frequency train of strain pulses. In that work it was found that the size of the signal should depend on the square of the laser power. However, the theory in that paper is not applicable to this situation as the strain pulses used in this work were not part of a train of pulses and had a broad frequency spectrum.

Another reason that the model is not applicable here is the strikingly different behaviour of the two superlattice structures. In this work, the observed transient voltage caused by the phonon wavepacket had the opposite polarity to the applied bias, as discussed in section 5.3.2, and it can be shown that this is due to the device resistance decreasing in the presence of the incident phonons. In the work by Poyser *et al.* the same electrical set-up was used but the transient voltage had the same polarity as the applied bias, which implies an increase in the superlattice device resistance in the presence of phonons. It was also found that the equation used by Poyser *et al.* to fit the I-V characteristics is a very poor fit for the NU1727 I-V characteristics. The higher-doped SL did not have a threshold for current conduction through the device, and it had a different shape to the rising edge and a large negative differential resistance effect in forward bias.

It is not clear why the response seen by Poyser should be so different to the response seen for the NU1727 SL used in this work. The growth parameters were nominally the same, except for the increased doping level in Poyser's SL. It is possible that the carrier screening caused by the additional doping was affecting the transport through the SL, but it was not expected to have such a large effect.

A more plausible explanation is the possible deviation of the thicknesses of the layers grown from the nominal values. The calculated dispersion for the NU1727 SL given in figure 5.7 does not give the same values for the zone edge and centre modes as those observed by Beardsley *et al.* in optical pump-probe measurements on the same wafer [50]. One way to account for the discrepancy is to assume that the layers grown were thicker than expected by approximately 12%, which leads to a calculated dispersion that agrees closely with the frequencies observed by Beardsley. Unpublished optical pump-probe experiments performed by Poyser on the SL structure used in reference [53] give a zone-centre mode of approximately 500 GHz, which agrees closely with the expected value based on the nominal layer thicknesses.

It has been unclear exactly which transport regime this SL structure should fall into under applied bias. In the past both the Wannier-Stark hopping model and the sequential tunnelling model have been used to describe transport in this structure [52,118], but in the most recent papers the sequential tunnelling model has become more strongly favoured [53,69]. It is likely that the different layer thicknesses from the two different growths can have a big effect on the charge transport in the device. A 12% increase in the thickness of all of the SL layers grown would lead to thicker barriers and therefore a reduced coupling between wells, while wider wells would have an effect on the energy levels within the wells. Alternatively, if the calibration error in the MBE growth was in the Al cell only the barriers could be up to 35% wider than expected, leading to a much larger change in the coupling between wells. The additional doping in the SL used by Poyser *et al.* would also increase the scattering rates in the quantum wells. These factors combined will all have an effect on the electronic transport through the two different SL structures, and this in turn could explain the difference seen in the I-V characteristics and the response to the incident acoustic wavepacket.

### **Estimate of miniband widths for the different possible layer thicknesses**

To make a quantitative comparison of the difference in the electron transport caused by the possible differences in layer thicknesses, the coupling

between the wells in the SL can be characterised in terms of the miniband width. This can be estimated using the Kronig-Penney model [126].

In the Kronig-Penney model, the 1D Schrödinger equation is solved for a square well potential using the boundary conditions that the wavefunction and its derivative must be continuous between the wells and barriers. As the superlattice is formed of two different materials a weighted effective mass is used to satisfy the boundary conditions. Other models use different boundary conditions that take into account the different effective masses in the two materials, but as these do not improve the accuracy of the miniband width calculation the simple Kronig-Penney model will suffice [108].

The equation that arises from the Kronig-Penney model that must be solved to determine the miniband width is

$$\cos(k_{SL}d_{SL}) = \frac{k_b^2 - k_w^2}{2k_b k_w} \sinh(k_b d_b) \sin(k_w d_w) + \cosh(k_b d_b) \cos(k_w d_w) \quad (5.7)$$

where  $k_{SL}$  is the wave vector in the superlattice,  $d_{SL}$  is the superlattice period,  $k_{b,w}$  are the wave vectors in the barriers and the wells, respectively, and  $d_{b,w}$  are the widths of the barriers and wells, respectively [126].

Equation 5.7 is solved by a numerical method, by the substitution of appropriate wavefunctions with trial energy values. Only solutions that satisfy the condition  $|\cos(k_{SL}d_{SL})| \leq 1$  are valid, as these solutions correspond to travelling waves. For other energy values there are no travelling wave solutions and forbidden gaps are formed.

The miniband widths were calculated for the GaAs/AlAs superlattices using a weighted average of the effective masses in the two layers taken from reference [79]. The energy gaps used for the two materials were 1.424 eV and 2.949 eV for GaAs and AlAs, respectively [127], the appropriate values for a type I superlattice at 10 K. The difference between type I and type II superlattices is shown in figure 5.18 [108], and is briefly outlined below. The value of the conduction band offset used in the calculation was 0.45 [128].

Semiconductor superlattices can be divided into two different types, called type I and type II [108]. In type I superlattices the conduction band minima and the valence band maxima occur in the same layer of the superlattice. This is illustrated in the energy band diagram in part a) of figure 5.18. In Type II superlattices the conduction band minima

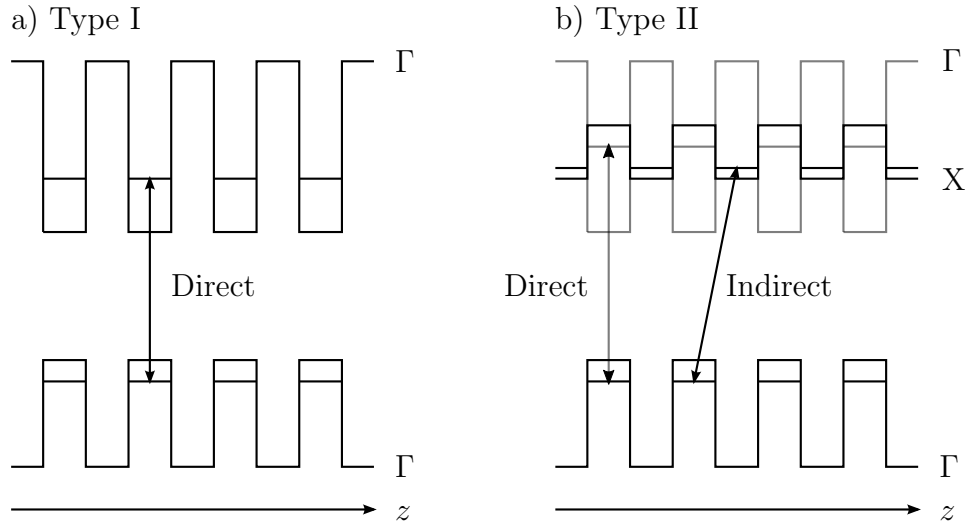


**Figure 5.18:** Schematic energy diagrams of type I and type II superlattice structures. In type I structures the conduction band minima and the valence band maxima occur in the same layer. In type II structures the conduction band minima and valence band maxima are separated in both real and reciprocal space.  $\Gamma$  and X refer to different regions of reciprocal space, and  $z$  shows the growth direction of the superlattice structure in real space.

and valence band maxima are separated in both real and reciprocal space. This is illustrated in part b) of figure 5.18. A transition from the valence band to the local minima of the conduction band at the  $\Gamma$  point is direct, however, the conduction band minima at the X point has a lower energy than the minima at the  $\Gamma$  point. This causes the electrons and holes to be confined in different layers of the structure, and transitions are then indirect. GaAs/AlAs superlattices can be either type I or type II depending on the thickness of the layers. The NU1727 superlattice has thick enough layers that it is probably a type I superlattice structure.

The first miniband width was calculated for 3 different scenarios: the nominal growth layers, which Poyser's SL is likely to conform to; a SL in which both the wells and barriers are 12% thicker; and a SL in which only the barriers are thicker by 35%. The latter two scenarios lead to acoustic phonon dispersion relationships that agree with the confined modes observed by Beardsley in the NU1727 superlattice [50].

The outcome of these calculations is summarised in table 5.2. The intended growth layers would have a first miniband width of approximately

**Table 5.2:** Results of calculations of the miniband width for different possible layer thicknesses for the NU1727 superlattice.

Well width	Barrier width	Miniband width
5.90 nm	3.90 nm	0.71 mV
6.61 nm	4.37 nm	0.28 mV
5.90 nm	5.27 nm	0.09 mV

0.71 mV. For thicker barriers between the wells, the coupling is reduced and the miniband becomes narrower. For the case where both the wells and barriers are thicker by 12% the miniband width would be  $\approx 0.28$  mV and for 35% thicker barriers the miniband width would be  $\approx 0.09$  mV.

As electron tunnelling depends exponentially on barrier width, a small change in the barrier thickness leads to a large change in the miniband width. A 12% increase in the thickness of all of the superlattice layers leads to a 60% reduction in the miniband width, while a 35% increase in the barrier thickness alone leads to an 87% reduction in the miniband width. The possible differences in the layer thicknesses between the two superlattice samples would make a huge difference to the miniband width, and hence the electron transport through the superlattice.

For superlattices that are considered to be weakly coupled the miniband width is less than the energy broadening due to scattering [114]. The energy broadening due to scattering can be estimated using the following equation

$$E_{scat} \approx \frac{\hbar}{\tau_{scat}} \quad (5.8)$$

where  $\hbar$  is the reduced Planck constant and  $\tau_{scat}$  is the scattering time. The main contributions to the electron scattering in the superlattice will be ionised impurity scattering, surface roughness scattering from the different layer boundaries and phonon scattering. At the low temperatures used in these experiments phonon scattering is negligible, and the good growth capabilities of molecular beam epitaxy mean that the surface roughness scattering is also likely to be low. The ionised impurity scattering is then the dominant scattering mechanism.

The scattering time associated with ionised impurity scattering can be estimated from the average time an electron travels before colliding with an impurity, using the Fermi velocity of the electrons and the average

distance between the ionised impurities. For the nominal layer thicknesses the estimated energy broadening is of the same order of magnitude as the miniband width. It is then unclear exactly which electron transport regime this superlattice should fall into. However, for the two scenarios in which the barriers are thicker than expected, the scattering due to broadening is an order of magnitude bigger than the miniband width. These two structures are then firmly in the weakly coupled regime. The possible differences in the layer thicknesses would have a big effect on the electron transport.

### Transitions contributing to the tunnel current

A decrease in the resistance of the superlattice device in the presence of phonons can be linked to an increase in the rate of phonon assisted carrier transport, while an increase in the device resistance implies a decrease in carrier transport. For weakly coupled superlattices, with wide barriers between the quantum wells, the electron transport is dominated by transitions between nearest neighbour wells. A “two well model” can then be used to describe the electron transport, as considered by Tsu and Döhler [111]. This was expanded upon by Glavin *et al.* [129] and later applied to the NU1727 superlattice structure by Cavill *et al.* [51].

There are two different basic mechanisms through which the incident phonons can change the current through the superlattice. In one case, the incident phonons cause interwell electron transitions. Electron hopping between different wells directly leads to a change in the current through the device. Alternatively, the nonequilibrium phonons cause intrawell electron transitions. This leads to electron heating, which indirectly affects the current through the SL device.

The angle of phonon incidence becomes important in determining if the interwell or intrawell transitions are dominant. Let the angle  $\theta$  be defined as the angle between the phonon wave vector  $\mathbf{q}$  and the SL axis. Due to the conservation of energy and momentum, it can be shown that intrawell phonon transitions occur for phonons that satisfy the condition  $\theta > v_s/v_F$ , where  $v_s$  is the speed of sound and  $v_F$  is the Fermi velocity [130]. For coherent phonons generated optically in the metal film,  $\theta \approx 0$  and interwell

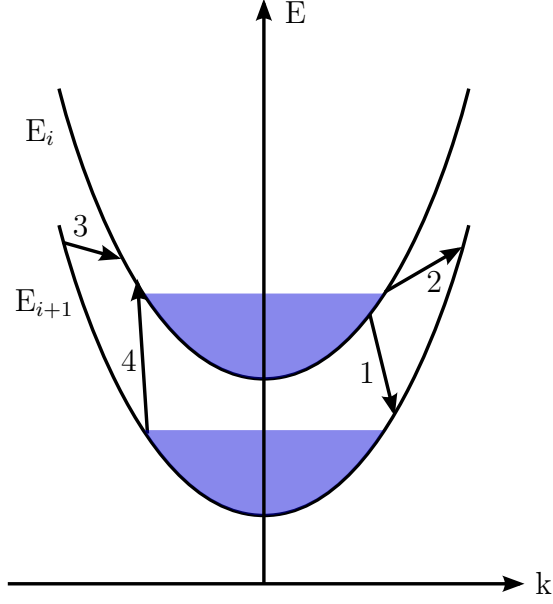


**Figure 5.19:** Illustration of one-phonon assisted tunnelling processes between two quantum wells with energies  $E_i > E_{i+1}$ . There are four such transitions of interest. Two processes involve the stimulated emission of a phonon (1 and 3) and the other two are absorption processes (2 and 4).

transitions dominate.

There are four possible one-phonon assisted interwell tunnelling processes that need to be included when considering the transient change in current  $\Delta I$ . This is illustrated in figure 5.19. Two of the processes involve the stimulated emission of a phonon (1 and 3), and two are absorption processes (2 and 4). Spontaneous emission of phonons can be neglected when considering the effects of an incident phonon pulse.

The transient change in the current  $\Delta I$  can be calculated for the case when the incident phonon energy  $E_p > k_B T_e$ , where  $T_e$  is the electron temperature, using the following equation modified from Cavill *et al.* [51]:

$$\Delta I = eA \sum_{\mathbf{q}} W(\mathbf{q}) g_d(\mathbf{q}) (n_{\mathbf{q}}^*(E_p) - n_{\mathbf{q}}^*(k_B T_e)) \quad (5.9)$$

where  $A$  is the area of the superlattice device and  $g_d(\mathbf{q})$  is the phonon density of states.  $W(\mathbf{q})$  is the transition rate, which is the sum of the rates of the four different transition processes:

$$W(\mathbf{q}) = W_1^+ + W_2^- - W_3^+ - W_4^- \quad (5.10)$$

where the superscripts  $+$  and  $-$  indicate phonon emission and absorption,

respectively, and the subscript relates to the four different processes shown in figure 5.19. The phonon occupation number is given as  $n_q^* = a_1 n_q$  where  $a_1 \leq 1$  as not all the phonons are incident on the device if heat pulses are considered, as in the work of Cavill *et al.* The  $-n_q^*(k_B T_e)$  term is included so that  $\Delta I = 0$  when  $E_p = k_B T_e$ .

The transition rate  $W(\mathbf{q})$  depends on the electron wave functions of the initial and final states in the two wells involved in the tunnelling process. The phonon matrix element between the two states depends on the energy difference between the two wells, the coupling between the wells, the well widths, and the superlattice period. It is likely that the transition rates for the four phonon-assisted tunnelling processes are different in the two superlattice samples, and this leads to the resistance decreasing in one sample in the presence of phonons whereas it increases in the other.

## 5.5 Measuring the transient voltage across the SL caused by incident heat pulses

It has previously been mentioned that some Al film transducers led to a transient voltage signal across the SL with different sized heat pulse responses. This is demonstrated graphically in figure 5.20, which shows the LA peak for two different Al films that were both nominally 30 nm thick. For the one labelled “Thin film 1” the LA heat pulse is more prominent, which appears at later times as a shoulder that is not fully resolved from the initial peak. For the one that is labelled as “Thin film 2” the peak that has been attributed to confined coherent phonons has a smoother decay. The data taken when using the film that produced a more prominent heat pulse component was used to analyse the properties of the heat pulses detected by the SL device.

As the film thicknesses were nominally 30 nm for both films in figure 5.20, it is unclear why the superlattice response should be so different. It is proposed that this difference is due to variations in the Al film deposition. The recent paper by Poyser *et al.* showed that different Al films could lead to a very different SL response [53]. Over time the same semiconductor

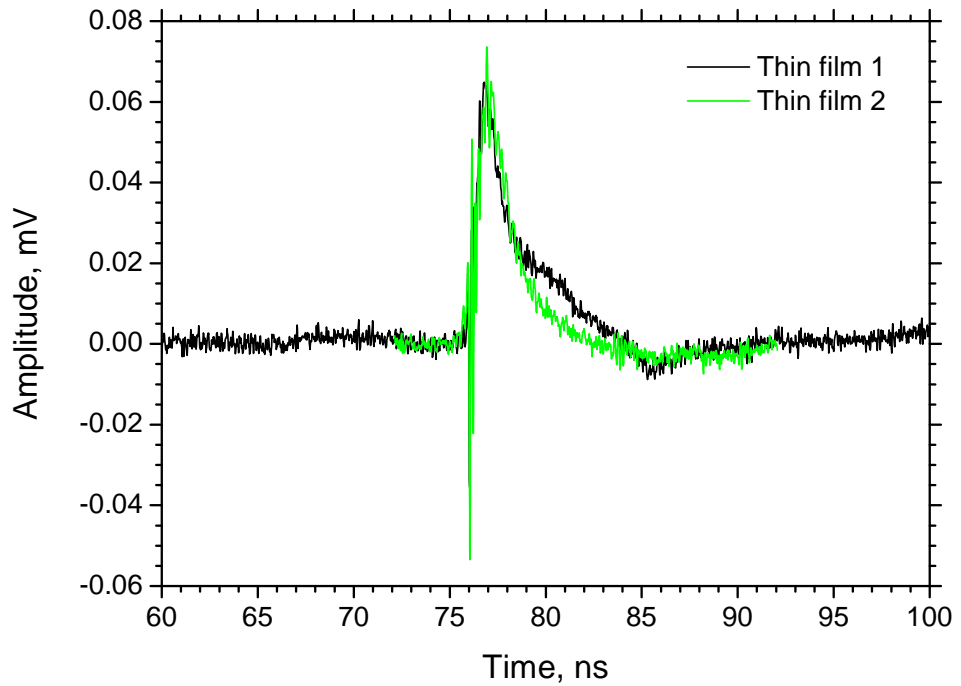


**Figure 5.20:** Comparing the superlattice response to an incident acoustic wavepacket generated in two different 30 nm Al transducer films. The amplitudes have been scaled for easy comparison. Thin film 1 displays a larger heat pulse contribution after the initial peak that is not present for thin film 2.

chip has been repeatedly processed, with the old Al film having to be removed before the application of a new one. Al films are very susceptible to oxidation during the deposition process and the adhesion of thin films depends heavily on surface preparation. Many factors could contribute to a difference in the Al film and then lead to a different acoustic pulse launched into the sample.

As the shape of the response of the SL to the propagating acoustic wavepacket was not easily reproduced between different applications of the Al film, further work is required to make the Al deposition more repeatable. It would also be useful to understand how the Al deposition conditions affect the composition of the acoustic wavepacket launched into the sample.

The transient voltage across the superlattice device was recorded for a range of applied bias and incident laser power when using the Al film

that produced a more prominent heat pulse. This allows an investigation of traits displayed by both the LA and TA heat pulses detected by the SL. This can be compared to previous work by Cavill *et al.* in which heat pulse experiments were performed using the same superlattice structure as a detector [51]. In that work, the heat pulses were generated by heating a thin constantan film with either a relatively long 12 ns duration laser pulse or an even longer duration electrical pulse in the 50-100 ns range.

### 5.5.1 Bias dependence

The bias dependences of the LA and TA heat pulses were investigated by the method previously described in section 5.4.1. The area under the transient voltage curve was integrated and this area was plotted against the applied bias, as shown in figures 5.21 and 5.22 for the LA and TA heat pulses, respectively.

In figure 5.21, the size of the detected LA heat pulse is shown for a range of applied bias for both the thin and thick Al film transducers. As seen for the bias dependence of the coherent confined phonons in section 5.4.1, a peak is present for negative applied bias at a value of -0.18 V. The proposed mechanism for this is the same as the one for the coherent phonons: the increased sensitivity of the superlattice as a detector when the Stark splitting of the energy levels in the SL is resonant with the confined modes in the SL device. This bias corresponds to the zone-centre mode at a frequency of 450 GHz.

This figure looks remarkably similar to the equivalent one for the coherent phonons in figure 5.16. In both cases a phonon wavepacket containing longitudinal acoustic phonons with a broad spread of frequencies has travelled through the SL structure. Both wavepackets contained a component at the frequency of the zone-centre mode that became trapped in the structure due to Bragg reflections. The main difference between the two situations is that the heat pulse phonons are incoherent whereas those from the initial strain pulse are coherent.

The peak in the thick film bias dependence is less pronounced than that for the case of the thin film Al transducer. This can be attributed to the

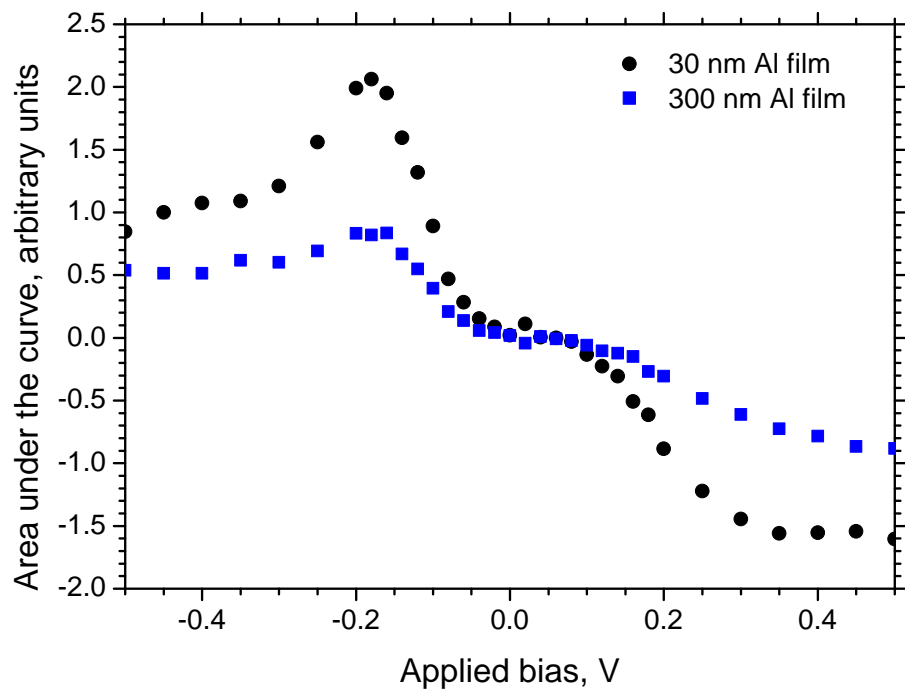


**Figure 5.21:** Bias dependence of the LA heat pulse in the NU1727 signal. A peak is present at -0.18 V, which is more pronounced for the thin Al film transducer compared to the thick film.

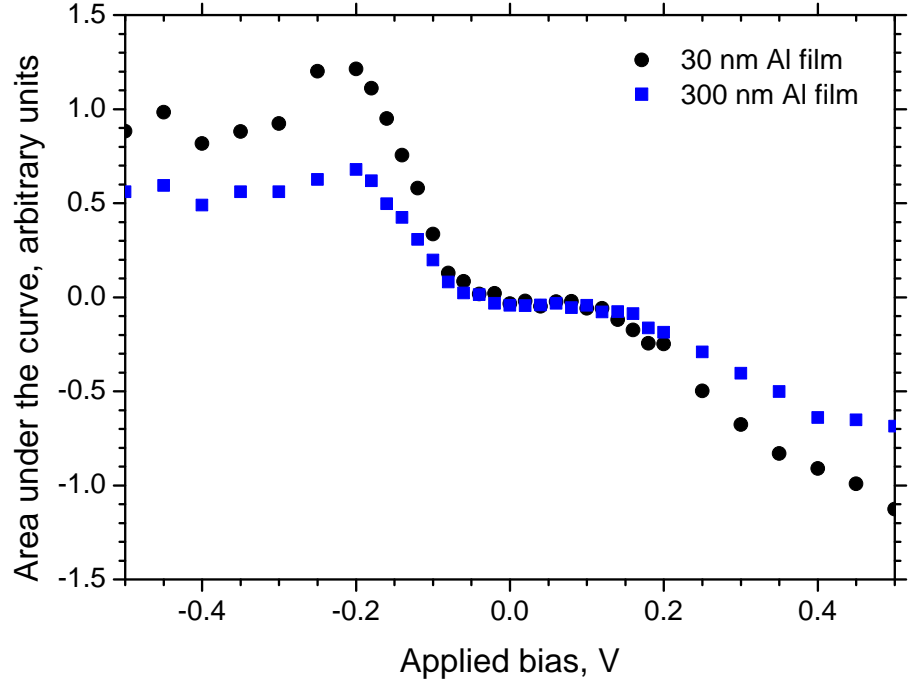


**Figure 5.22:** Bias dependence of the TA heat pulse in the NU1727 signal. A peak is observed at -0.22 V, which is more pronounced for the thin Al film transducer compared to the thick film.

spectrum of the heat pulse generated in the Al film. For thicker films the incident laser energy is absorbed in a larger volume. This will cause the heater temperature for the heat pulse generation to be lower and so less frequency components in the range of the confined modes will be generated.

Figure 5.22 shows the equivalent data for the size of the TA heat pulse for the same range of applied bias. Again, a peak is clearly present in the negative part of the bias range, this time at approximately -0.22 V. The same approach can be used as for the strain pulse in section 5.4.1 using equation 5.6. The threshold voltage  $V_T = 50$  mV and the fraction of the bias dropped across the SL itself,  $\Upsilon$ , was estimated to be 70-80%. This would lead to an energy level splitting that is resonant with phonons at frequencies in the range 570-660 GHz.

The fraction of the applied bias that is dropped across the SL,  $\Upsilon$ , will not necessarily be constant under the application of different magnitude biases. If some of the voltage drop was caused by a potential barrier, the

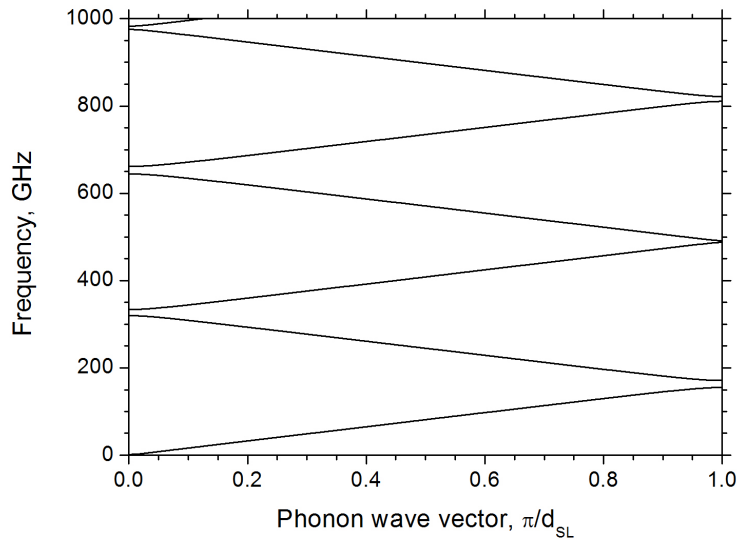


**Figure 5.23:** Calculated dispersion for transverse acoustic phonons in the NU1727 superlattice. The layer thicknesses have been assumed to be 12% larger than specified based on Beardsley’s pump-probe results [50] as discussed in section 5.4.2. The stop gaps open up at lower frequencies than for the LA phonons, with the first zone-centre gap at only 320-334 GHz.

barrier height could change with changing applied bias and this would alter the fraction of the applied bias that was dropped across the superlattice.

Transverse acoustic phonons travel slower than longitudinal acoustic phonons, and so the stop gaps in the dispersion open up at lower frequencies. An example TA phonon dispersion is shown in figure 5.23 where it has been assumed that the SL layers are 12% thicker than specified based on Beardsley’s optical pump-probe measurements [50] and the discussion in section 5.4.2. This should then lead to a peak in the bias dependence at a smaller bias compared to the case of the LA heat pulse, but the peak is instead observed at a larger applied bias. As discussed for the case of the LA phonons, it is possible that the lower frequency modes are simply not resolved in this experiment due to broadening of the energy levels and the position of the peak relative to the large rising edge of the signal.

The peak observed in figure 5.22 could be due to a higher order transverse mode that is trapped within the SL, as this would account for the higher frequency. The second order zone-centre mode has a frequency of

approximately 650 GHz, and this falls within the predicted frequency range when assuming that  $\Upsilon = 0.7-0.8$ . For phonons with a frequency of 650 GHz to be resonant with the splitting of the energy levels in the SL,  $\Upsilon \approx 0.8$ . This is consistent with part of the bias being dropped across a potential barrier that decreases in height as the applied bias is increased.

Coupling between phonons and electrons is typically different for the LA and TA phonons. Using the traditional model that assumes an acoustic isotropy, only LA phonons can couple to electrons via the deformation potential and TA phonons couple via the piezoelectric effect [72, 76]. The deformation potential interaction is proportional to the phonon wave vector  $q$ , while the piezoelectric effect interaction is proportional to  $q^{-1}$ . As such, the deformation potential coupling is expected to dominate at high frequencies and a TA phonon effect that is much smaller than the LA phonon effect would be expected. Instead, the size of the signals are comparable for the LA and TA phonons. This larger TA contribution can be attributed to acoustic anisotropy in the crystal leading to quasitransverse modes that are able to couple to electrons via the deformation potential [60].

## 5.5.2 Comparison to previous work

These experiments are similar to previous work by Cavill *et al.* in which the same superlattice structure was used to detect heat pulses generated in a constantan film [51]. Two generation methods were used: an optical method and an electrical method. In the optical method a 12 ns duration laser pulse was used to excite a heat pulse in an extended constantan film. In the electrical method a 50-100 ns electrical pulse was used to generate the heat pulse in a small area constantan heater. The arrival of the heat pulses at the SL was detected by observing the transient current measured in the SL device.

In both methods used by Cavill *et al.*, the heat pulse generation in the film was caused by a relatively long exciting pulse compared to the femtosecond laser used in the work discussed in this thesis. With the longer pulses it was difficult to resolve the separate longitudinal and transverse contributions.

The bias dependence of the change in the size of the tunnel current was measured for a range of heater temperatures. It was found that there was a peak at a bias value that increased with increasing heater temperature. The Stark splitting  $\Delta_S$  was estimated from the applied bias and the relationship between the peak Stark splitting and the heater temperature was given by

$$\Delta_{\max} = 0.7k_B T_h + 1.1\text{meV} \quad (5.11)$$

when the applied bias  $V < 0$ .  $\Delta_{\max}$  is the splitting of the energy levels for which the peak in the tunnel current response occurred at a given temperature,  $k_B$  is the Boltzmann constant and  $T_h$  is the heater temperature.

An estimate of the heater temperature generated by the femtosecond laser can be calculated for comparison using the volume of the film in which the laser light is absorbed, the heat capacity of aluminium and the following expression

$$\Delta T = \frac{E}{\rho V_{ol} C_m} \quad (5.12)$$

where  $\Delta T$  is the rise in temperature,  $E$  is the energy absorbed in the Al film,  $\rho$  is the density of Al,  $V_{ol}$  is the volume in which the laser energy is absorbed and  $C_m$  is the specific heat capacity of Al.

The laser output energy was 1 mJ per pulse, but after attenuation in the optical set-up the energy incident on the Al film was  $\approx 1 \mu\text{J}$  per pulse. The reflectivity of bulk Al is approximately 90%, however, for sufficiently thin Al films a large fraction of incident light can be transmitted through the entire film. For 800 nm wavelength light the penetration depth in Al is only a few nanometres, so for a 30 nm film there will be some transmission of the incident laser light, but the fraction will be small enough to ignore for the purpose of this estimate. In practise, 30 nm thick Al films are often used for acoustic transducers in picosecond acoustic experiments because the film is thick enough to absorb most of the laser light that is not reflected, while being thin enough to limit the broadening caused by hot electron diffusion in the film [8, 17, 18, 49]. Assuming that 10% of the incident laser light was absorbed by the Al film, the energy  $E$  absorbed for a single laser pulse was approximately 0.1  $\mu\text{J}$ . The femtosecond laser pulses are sufficiently short that heat loss from the film on this time scale can be ignored.

The Al film thickness was 30 nm and the laser was focussed to a spot with a diameter of  $\approx 100 \mu\text{m}$  leading to a volume  $V_{ol} = 3 \times 10^{-16} \text{ m}^3$ . With

$\rho = 2712 \text{ kg m}^{-3}$  and  $C_m = 0.91 \text{ kJ kg}^{-1}\text{K}^{-1}$  for aluminium it can be estimated that the temperature rise  $\Delta T \approx 140 \text{ K}$ . As the sample was mounted in a continuous flow cryostat at a temperature of 4 K, this is approximately equal to the heater temperature  $T_h$ .

With a heater temperature in the region of 140 K when using the amplified femtosecond laser, this is vastly different from the heater temperatures investigated by Cavill *et al.*, which were in the range of 5-20 K. Clearly the regime discussed by Cavill *et al.* cannot be extrapolated to apply to the results given in this thesis.

Cavill *et al.* assumed a black body spectrum for the heat pulse and expected to see a gradient of the  $\Delta_{\max}(k_B T_h)$  slope 4 times larger than the gradient observed experimentally. It is probably not realistic to assume a black body spectrum due to cooling of the film, along with phonon down conversion and other scattering effects in the substrate. Importantly, the confinement of phonon modes within the superlattice was not considered in the Cavill work as there was no evidence for it in the temporal regime due to the long duration heater pulses and the lack of resolution. In the work presented in this thesis, the LA and TA components are well resolved and the temporal resolution is sufficient to suggest that there is evidence of confinement of phonons in the SL.

When considering the confined modes within the SL, changing the heater temperature will change the amount of phonons present at the frequency of the confined mode. If the confined modes have a significant effect then this could be dominant over the frequency shift in the peak of the black body spectrum.

### 5.5.3 Laser power dependence

The variation in the size of the LA and TA heat pulses was also investigated as the incident laser power was changed. The area under the curve was integrated for each heat pulse for a range of laser powers. The results of this are shown for the case of the thin Al film transducer and an applied bias of -0.14 V in figure 5.24. Both the LA and TA heat pulses show a roughly linear dependence as demonstrated by the straight lines, which

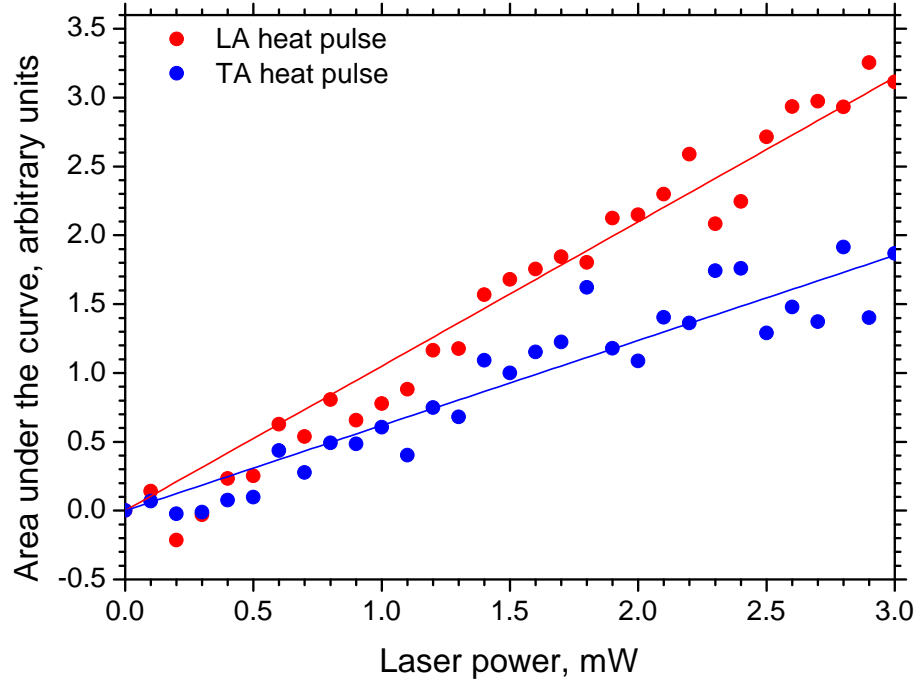


**Figure 5.24:** Laser power dependence of both the LA and TA heat pulses in the NU1727 signal. The thin Al film transducer was used and a bias of -0.14 V was applied. The sizes of both the LA and TA heat pulses have a roughly linear dependence on the laser power, as shown by the linear fits made to the experimental data with the form  $y = a_1x$ , where  $a_1$  is a constant and the line has been constrained to go through the origin to obtain a physical result.

are linear fits to the experimental data of the form  $y = a_1x$ , where  $a_1$  is a constant and the line has been constrained to go through the origin to obtain a physical result.

A detailed evaluation of the heat pulse dependence on laser power is quite complicated and it is necessary to accurately know the temperature of the Al film transducer to determine the Planck distribution. This is relatively simple for heat pulses generated with an electrical pulse [51], however in the optical method there are many factors to consider to determine how much of the incident laser light pulse is absorbed by the Al film. For this work a simple estimate will suffice.

The number of phonons at a given frequency  $N(f)$  is described by a

Planck distribution as

$$N(f)df \propto \frac{f^3}{(e^{hf/k_B T} - 1)}df \quad (5.13)$$

where  $f$  is the phonon frequency,  $h$  is Planck's constant,  $k_B$  is the Boltzmann constant and  $T$  is temperature. This can be simplified by making the assumption that the temperature of the Al film is high such that  $k_B T \gg hf$ . The heater temperature was estimated in section 5.5.2 to be 140 K, so for frequencies in the region of 500 GHz this approximation is valid. The exponential term can then be expanded as a Taylor series and equation 5.13 can be simplified to

$$N(f) \propto \frac{f^2 k_B T}{h} \quad (5.14)$$

Equation 5.14 shows that the number of phonons at a given frequency is proportional to the temperature of the Al film. Let us assume that the temperature the Al film reaches is proportional to the power dissipated in the film. As the femtosecond laser pulse is extremely short, it is reasonable to assume that the film reaches its peak temperature before the film has time to radiate and cool. If this assumption is valid, then the number of phonons at a given frequency is proportional to the incident laser power. This agrees with the trend observed in figure 5.24.

## 5.6 Conclusion

This chapter explored the electrical detection of acoustic wavepackets with a semiconductor superlattice structure after propagation of the phonons across the substrate of the sample. A range of different thickness Al film transducers were used to generate the acoustic wavepackets as this changes the frequency spectrum of the incident phonons. The transient voltage across the SL device was measured and recorded.

For a thin Al film transducer the response of the SL to the acoustic wavepacket comprised of several parts: a fast strain pulse, a peak with a width of 2 ns, a longitudinal acoustic heat pulse and a transverse acoustic heat pulse. It is suggested that the 2 ns width peak is caused by electrical detection of confined modes from the centre of the mini-Brillouin zone. The

2 ns width peak was only present when using the thin Al film transducer, which was the only film able to generate high enough frequencies to excite these long-lived high-frequency modes. This effect was also only observed using the 50 period SL, which has sufficient confinement of these modes. The 10 period SL sample with the same nominal growth parameters did not show this effect for any thickness of Al film transducer.

The effect of the position of the laser spot relative to the SL mesa was investigated, which showed that the 2 ns width peak was caused by coherent phonons and the following slow decay was an incoherent heat pulse. This provides evidence that the 2 ns width peak is due to coherent confined modes caused by the initial fast strain pulse as it travelled through the SL. The bias and laser power dependence of different parts of the signal were also investigated. A peak was observed in the bias dependence for both the coherent and incoherent parts of the signal. This peak is thought to be due to an increased sensitivity of the SL as a detector when the splitting of the energy levels is resonant with the confined phonons in the SL.

The data taken was not of a sufficient quality to determine if there was any increase in the width of the coherent peak for certain applied bias. This could lead to evidence of phonon amplification of the confined modes. This requires further experimental work to get both the required resolution and signal-to-noise ratio.

A comparison was made to work performed by Poyser *et al.* on a similar superlattice structure [53]. Poyser's SL had nominally the same layer thicknesses but a higher doping density. It is not clear why the doping alone should cause the large differences observed between the two SL samples. It is suggested that the NU1727 layers are thicker than expected, and the differences in the SL layer thicknesses can have a large effect on the transport through the device.

There are plenty of opportunities for further work to be carried out in the future. The discussions of some of the results presented in this chapter are speculative in nature, as there is currently no quantitative theory to confirm that the effects observed here are indeed due to the confinement of phonons within the SL. Along with the development of a working theory for the electrical detection of the confined modes, the striking difference

between the response of the two different SLs with almost the same growth parameters could be further investigated theoretically.

There are also several experimental details that need to be confirmed. The transient voltages measured across the SL were not consistent between Al transducers with the same nominal thickness; this could be repeated to ensure that the effect is reproducible. It would also be very interesting if experiments designed specifically to look for evidence of phonon amplification were performed, as this would support previous work on this subject.

# Chapter 6

## Conclusions and future work

This final chapter concludes this thesis by providing a summary of the experiments performed on ultrafast acoustoelectric effects in semiconductor devices, and by revisiting the main conclusions from the previous chapters. Work on this topic is by no means complete as the interactions of ultrafast acoustics and electronic devices is a promising field of research with great potential for practical applications. Some suggestions for possible directions of future research are outlined in this chapter.

### 6.1 Conclusions

Schottky diodes were investigated as a possible device for the electrical detection of ultrafast acoustic wavepackets. Previous work by Moss *et al.* indicated that the Schottky diode would be a suitable device as it had previously shown a fast transient current in response to incident picosecond strain pulses [47]. Specifically, the aim of this work was to perform heterodyne mixing of the detected acoustic frequencies with a microwave local oscillator.

Initially, devices grown and fabricated at the University of Nottingham were used in these experiments. A strain pulse was generated using a femtosecond pulsed laser focussed on an Al film thermally deposited on the opposite face of the substrate. These devices showed a strong electronic

response to the incident strain pulse after it had propagated across the sample, and in contrast to the previous work by Moss *et al.* the main detection region was the semiconductor-metal interface itself, as opposed to the edge of the depletion layer. However, these devices had a poor microwave response due to the necessity to couple the microwaves in via free space. Bow-tie antenna were fabricated directly onto the GaAs substrate and this was not an effective antenna structure due to the high dielectric constant of GaAs.

A waveguide-mounted Schottky diode provided by e2v for use in these experiments proved to be significantly more responsive to microwaves. Using this device, the first evidence of the heterodyne mixing of coherent acoustic phonons with microwaves was obtained. A Fabry-Perot cavity was used to form a train of optical pulses from a single femtosecond laser pulse. When the train of optical pulses was incident upon the GaAs substrate of the device it produced a quasi-monochromatic acoustic wavepacket with a tunable centre frequency set by the cavity spacing. The narrow frequency band acoustic wavepacket propagated across the substrate to the Schottky diode where it was mixed with the 94 GHz local oscillator signal. Mixing was performed with both the fundamental acoustic frequency generated in the sample and the second harmonic.

This set-up has the potential to act as a detector of high frequency acoustic waves that is capable of spectral resolution, as the acoustic frequencies are down-converted to a lower range that is more easily processed by currently available electronic instrumentation. Alternatively, an acoustic local oscillator could be used and this fixed acoustic frequency could be mixed with an incoming electromagnetic signal. An acoustic source could provide a simpler route to the generation of high frequencies for the local oscillator signal, without the need for a complicated chain of several multipliers. The SASER could be a suitable device for this purpose, which would provide a narrow bandwidth, high frequency acoustic signal that would be very stable over time and with a good phase noise [70].

Semiconductor superlattices were also investigated as a potential device to electrically detect acoustic wavepackets on the ultrafast time scale. Strain pulses were generated optically in an Al film transducer before propagating across the substrate of the sample to the superlattice device. A

transient voltage was produced across the superlattice in response to the incident acoustic pulse, and from the polarity of the detected voltage change it was determined that the presence of the phonons increased the electron transport through the superlattice.

The observed signal comprised of 4 different parts: a fast strain pulse, an unexpected peak with a width of approximately 2 ns, a longitudinal acoustic heat pulse and a transverse acoustic heat pulse. It is proposed that the 2 ns width peak was caused by the confinement of long-lived phonon modes from the centre of the mini-Brillouin zone. This peak was not present when the strain pulse was generated in thicker Al film transducers, as the acoustic wavepacket generated in the thicker films did not contain sufficient high frequency components to populate the confined modes. The extra peak was also not observed when using a superlattice with only 10 periods as there were insufficient layers to form strong confinement of these modes.

The work was compared to previous studies on similar superlattice structures. Poyser *et al.* used a superlattice device with the same nominal layer thicknesses to detect a high frequency train of strain pulses [53]. The transient voltage detected across Poyser's superlattice did not show any evidence of an electronic response to the confined phonon modes that would have been present in both SLs. Indeed, the response from the two superlattices were quite different, as the transient voltage generated by the incident acoustic wavepacket had a different polarity for the two different superlattice samples. In the experiments performed for this thesis the incident phonons caused an increase in the electron transport in the superlattice, while in the work by Poyser *et al.* the electron transport in that superlattice decreased in the presence of acoustic phonons. This suggests that there is something very different in the phonon induced electron transport in the two superlattice structures, despite their similar growth parameters.

Optical pump-probe measurements performed by Beardsley [50] and Poyser (C. L. Poyser, personal communication, August 2015) found that the confined modes occur at different frequencies in the two superlattices. As the dispersion relation is inherently linked to the thickness of the layers in the superlattice, this led to the suggestion that the layers in the superlattice used for the experiments described in this thesis could be up to 12% thicker

than expected, or the barriers could even be 35% thicker than expected if the calibration error was in the Al cell alone. Electron transport through the superlattice depends heavily on the coupling between adjacent quantum wells in the structure, so changing the thickness of the barriers will have an effect on the electron transport. For the two devices discussed this change seems to have had a particularly profound effect on the transport.

The heat pulses generated at the same time as the strain pulse also produced transient changes in the voltage across the superlattice, and this made it possible to compare this work to previous work by Cavill *et al.* on the same superlattice structure [51]. In the heat pulse experiments performed in the Cavill paper a longer duration excitation was used to create the phonon pulse that propagated across the substrate to the device. Confinement of phonon modes in the superlattice was not considered by Cavill *et al.* as there was no evidence for it in the temporal regime due to the lack of resolution caused by using a long excitation pulse.

## 6.2 Future work

This thesis has built upon existing work performed at the University of Nottingham on semiconductor devices that may be suitable for use in ultrafast acoustoelectric techniques. Some of the experiments performed in this thesis have generated new questions, and it would be interesting to see some of these addressed. Alongside that, there are several other possible options for combining ultrafast acoustics with electronic devices that have yet to be explored. In this section, some suggestions are given for possible areas of future work.

A very important topic has so far been neglected if picosecond acoustic techniques are going to be feasible without the use of an expensive laser system – the electrical generation of high frequency strain pulses. A possible method has been considered and early findings are shown in section 6.2.3.

### 6.2.1 Mixing acoustic phonons with microwaves

Part of the initial motivation for investigating the response of the superlattice structure to incident ultrafast strain was to determine if the superlattice was a possible mixer element for the mixing of coherent acoustic waves and microwaves. In this thesis it has been shown that the superlattice can produce a transient voltage in response to a short pulse of acoustic waves. Other studies have successfully used microwave sources to pump semiconductor superlattice structures for harmonic generation and parametric oscillators, showing that superlattices can respond to incident microwaves [131]. The current-voltage (I-V) characteristics of the superlattice devices are non-linear, making them a suitable candidate for a mixer element and previous work using superlattices as multipliers for electromagnetic signals suggests that they could be more effective in this role than Schottky diodes [132].

Some initial attempts were made to mix high frequency acoustic waves with microwaves using existing superlattice samples. However, there were difficulties based on the structure of the devices. As the substrate was thick ( $\sim 300 \mu\text{m}$ ) the experiments had to be performed at cryogenic temperatures to reduce the attenuation of the acoustic phonons as they travelled across the GaAs substrate to the superlattice. Coupling microwaves into devices in the cryostat through free space was problematic, as the initial attempts used bow-tie antennas that were proved ineffective in the case of the Schottky diode experiments.

There are several different options that could be implemented to improve the coupling of the microwaves into the superlattice device. It could be possible to fabricate new devices by a different process that includes back thinning of the wafer. The beam-lead Schottky diode provided by e2v had a substrate thickness of only  $11 \mu\text{m}$ , which was thin enough to perform the experiments at room temperature. With the device outside of the cryostat it is relatively straightforward to couple the microwaves to the device via waveguide, which provides a significant improvement in signal strength. However, it is likely that designing and producing such devices would be a lengthy process with some difficult device fabrication. Installing an appropriate waveguide structure along with the existing cryostat cabling is also

likely to be complicated and impractical.

A more appropriate solution to attempt initially would be to couple the microwave signal to the superlattice device via the existing cryostat cabling. The current cable in the cryostat is only rated to 20 GHz but it was tested on a vector network analyser and it was found that a large fraction of microwave power was transmitted through the cable at frequencies above 20 GHz. Indeed, up to 50% of the input power at frequencies up to 40 GHz was transmitted through the cable. If a different microwave source was used, with a frequency in the range of approximately 30 GHz, a reasonable microwave power could be coupled to the superlattice device in this manner.

Superlattices are capable of generating higher harmonics of an incident microwave source due to their non-linear I-V characteristics. A 30 GHz microwave source could be used as a local oscillator source for mixing experiments, and the higher harmonics could be mixed with an acoustic wavepacket with a centre frequency in the region of 100 GHz. The only remaining component required is a bias tee that allows the 30 GHz microwaves to be coupled to the cryostat cabling.

### **6.2.2 Electrical detection of ultrafast acoustic pulses using a superlattice**

The work on the electrical detection of ultrafast acoustic pulses using semiconductor superlattice devices has created several avenues of possible further work. The suggestion that the extra peak observed in the transient voltage was caused by long-lived phonon modes confined in the superlattice was based on the experimental observations. There have been no theoretical calculations performed to confirm or contradict this, and this is a potential area of future work for a theoretician. Also, as the shape of the detected signal varied with different Al film transducers of nominally the same thickness it would be prudent if these experiments were repeated to ensure that the observed effect is reproducible.

An attempt was made to determine if there was evidence of amplification of the long-lived phonon modes, but it was unsuccessful due to the poor signal-to-noise ratio. This superlattice structure has previously been

shown to exhibit phonon amplification [29], and any further evidence of this effect would compliment the existing results. If the signal-to-noise ratio could be improved through experimental techniques, clearer data could be obtained to perform the relevant analysis.

Another important area of possible future work arises from the striking difference in the transient voltages observed across this superlattice structure and a similar one used by Poyser *et al.* [53]. For one superlattice, the device resistance decreased in the presence of acoustic phonons, and for the other superlattice the resistance increased. This suggests that the phonon-induced electron transport is very different between the two superlattice structures.

Based on their nominal growth parameters it is unclear why the electron transport should be so different for the two samples, but it is suggested that the layers of the NU1727 superlattice were thicker than expected. The different electron transport regimes in semiconductor superlattices is still an ongoing field of research, and it would perhaps be interesting for a theoretician to investigate the difference in phonon-assisted electron transport between these two superlattices.

### 6.2.3 Electrical generation of ultrafast strain pulses

While the electrical detection of high frequency coherent acoustic phonons has the potential to be very useful in a range of applications, it is still limited as a technique if the phonons have to be generated using a femtosecond laser system that is both expensive and complicated. One particularly important area of future work then, is the generation of high frequency coherent strain pulses by an alternative method. In keeping with the rest of the work in this thesis an electrical method has been considered.

One possible device to consider is a step recovery diode. A step recovery diode (SRD) is a *p-i-n* diode with a graded band gap intrinsic region [133]. Under the application of forward bias, carriers are stored in the intrinsic region of the device. When the bias applied to the SRD is switched from positive to negative, the stored carriers are very quickly swept out of the junction. It is suggested that this fast movement of carriers could possibly

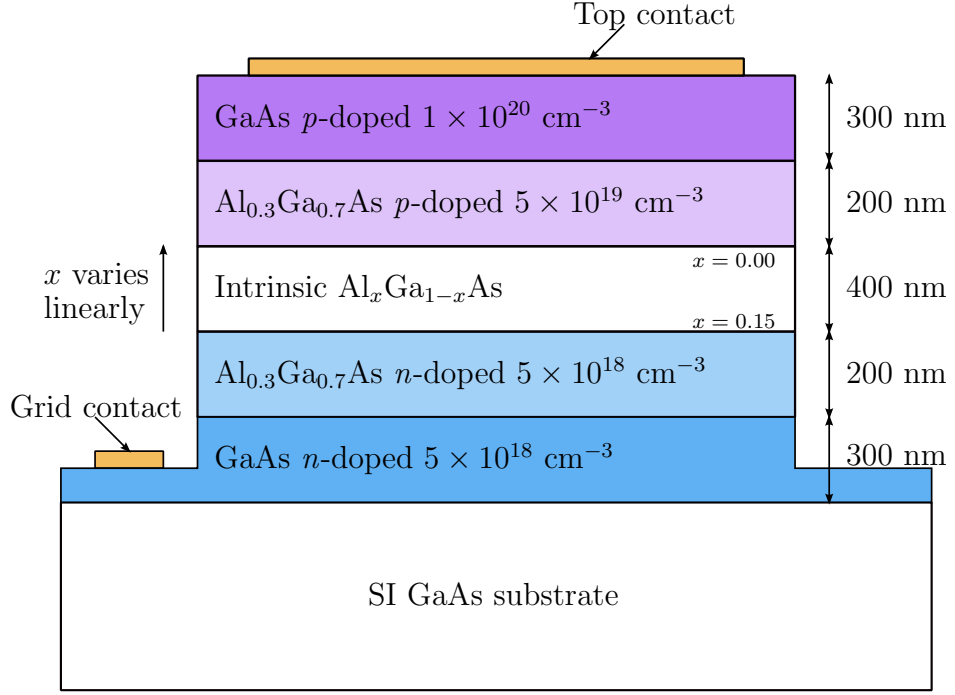


**Figure 6.1:** Schematic diagram of a step recovery diode fabricated from the Mn775 wafer. It is a  $p$ - $i$ - $n$  diode in which the intrinsic region has a variable band-gap as determined by the value of  $x$  in the  $\text{Al}_x\text{Ga}_{1-x}\text{As}$  layer.

generate a strain pulse due to the deformation potential.

Some preliminary work has been performed on this topic as part of work for this thesis. A wafer profile was designed based on the papers by Tan *et al.* [134] and Ao *et al.* [135] and the nominal growth specifications are shown in figure 6.1. A 300 nm  $n$ -doped GaAs layer ( $n = 5 \times 10^{18} \text{ cm}^{-3}$ ) was grown on a semi-insulating GaAs substrate to form the bottom contact layer. This was followed by a 200 nm  $n$ -doped  $\text{Al}_{0.3}\text{Ga}_{0.7}\text{As}$  layer ( $n = 5 \times 10^{18} \text{ cm}^{-3}$ ), which would help in confining carriers to the charge storage layer. The charge storage region is an intrinsic  $\text{Al}_x\text{Ga}_{1-x}\text{As}$  region in which  $x$  should ideally vary linearly from  $x = 0.15$  to  $x = 0.00$  in the direction of growth. This layer was followed by a 200 nm  $p$ -doped  $\text{Al}_{0.3}\text{Ga}_{0.7}\text{As}$  layer ( $p = 5 \times 10^{19} \text{ cm}^{-3}$ ), which was also intended to aid the confinement of carriers to the charge storage region, and finally a 300 nm  $p$ -doped GaAs ( $p = 1 \times 10^{20} \text{ cm}^{-3}$ ) top contact layer.

In reality, the layers grown for the Mn775 wafer were altered slightly from the suggested growth structure. The very high  $p$ -doping was not available with the carbon cell installed on the MBE machine. Instead, the

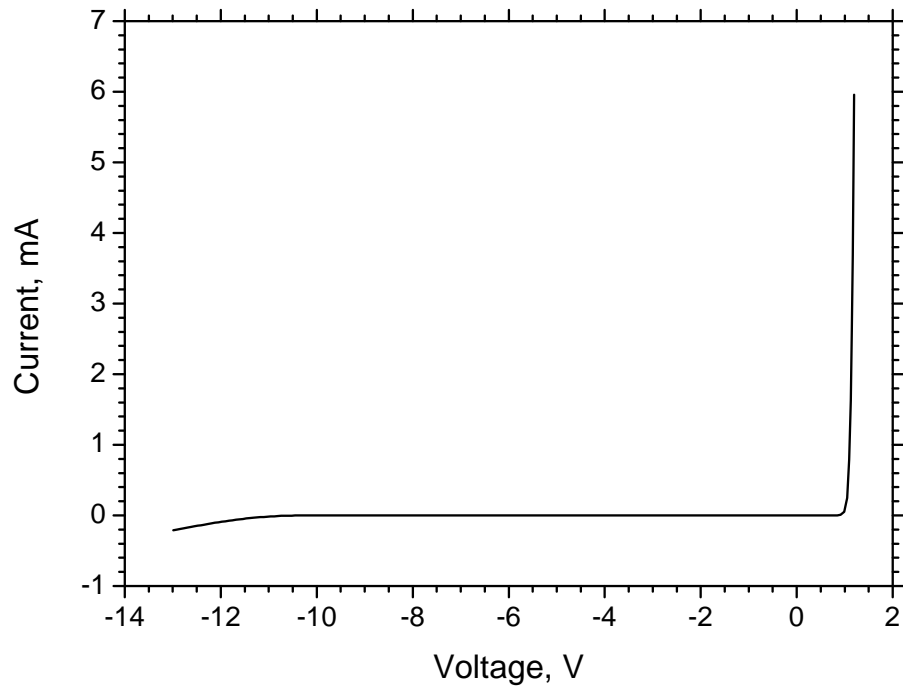


**Figure 6.2:** I-V characteristics of a 200  $\mu\text{m}$  diameter step recovery diode fabricated from wafer Mn775. The device has a typical diode-type characteristic with a turn on voltage of approximately 1 V and a reverse breakdown at a larger negative voltage than -11 V, although an appreciable reverse leakage current is present from -11 V.

$p$ -doping was made as high as possible with the existing carbon cell, and the ratio between the doping concentrations of the two layers was unchanged. Another deviation from the structure in figure 6.1 relates to the linear variation of  $x$  within the  $\text{Al}_x\text{Ga}_{1-x}\text{As}$  layer. To do so is not trivial and it was decided instead to ramp the temperature of the Al cell linearly, which leads to a logarithmic change in flux.

Devices were fabricated from the Mn775 step recovery diode wafer by etching to the bottom contact layer to create cylindrical mesas in a range of sizes. A  $p$ -type ohmic contact was formed to the top of each mesa and a large grid style  $n$ -type ohmic contact common to all devices was formed to the bottom contact layer. An existing photolithography mask set was used when processing the devices for these initial proof-of-principle type experiments. The mask set was the same one that was used to process the NU1727 superlattice sample, as shown in the microscope image in figure 5.5.

The I-V characteristics of the diodes fabricated from wafer Mn775 were investigated by the method described in section 3.2, in which a bias is applied to the device and a small-value resistor in series and the current is calculated from the voltage measured across the resistor. The I-V characteristics of a 200  $\mu\text{m}$  diameter device at room temperature are shown in figure 6.2. The device characteristics are fairly typical for a diode, with a sharp turn on at approximately 1 V. The diode has an appreciable reverse leakage current from about -11 V, and reverse breakdown occurs at a larger applied negative bias not shown in the figure.

Initial tests were performed to determine if the device behaved as a step recovery diode. A positive bias was applied to the device and then the applied bias was switched from positive to negative. The pulse sharpening effect is expected to occur on the falling edge as the negative bias removes the carriers from the charge storage region. An example of the results obtained from this test is shown in figure 6.3 for a 200  $\mu\text{m}$  diameter device. The output of the device shows the characteristic shape of a poor step recovery diode with the associated “slow tail” and “round off” portions, marked as “a” and “c”, respectively [133]. Part of the output curve has a steeper gradient compared to the input curve (part “b”), showing that the device is capable of the quick movement of carriers. Overall the output transition is no faster than the input transition due to the pronounced slow tail and round off effects.

There are several aspects of the device processing that could be improved to produce better SRDs. The process would greatly benefit from a purpose designed mask set for the photolithography stages. Previous studies have used two etches to form the mesas, with one etch to the bottom contact layer and another etch that stopped in the  $p$ -doped  $\text{Al}_{0.3}\text{Ga}_{0.7}\text{As}$  layer such that the top part of the mesa had a smaller diameter than the bottom part. This was done to reduce surface current flow to the charge storage region and so reduce the surface recombination current [134, 135]. It would also be beneficial to be able to use significantly smaller mesas to reduce the capacitance of the devices. The existing mask set is limited by the size of mesa that can be contacted by Al wire using a wedge bonder.

It is also likely that the step recovery effect would be more pronounced if a pulse generator with a faster rise time was used, as the input rise time

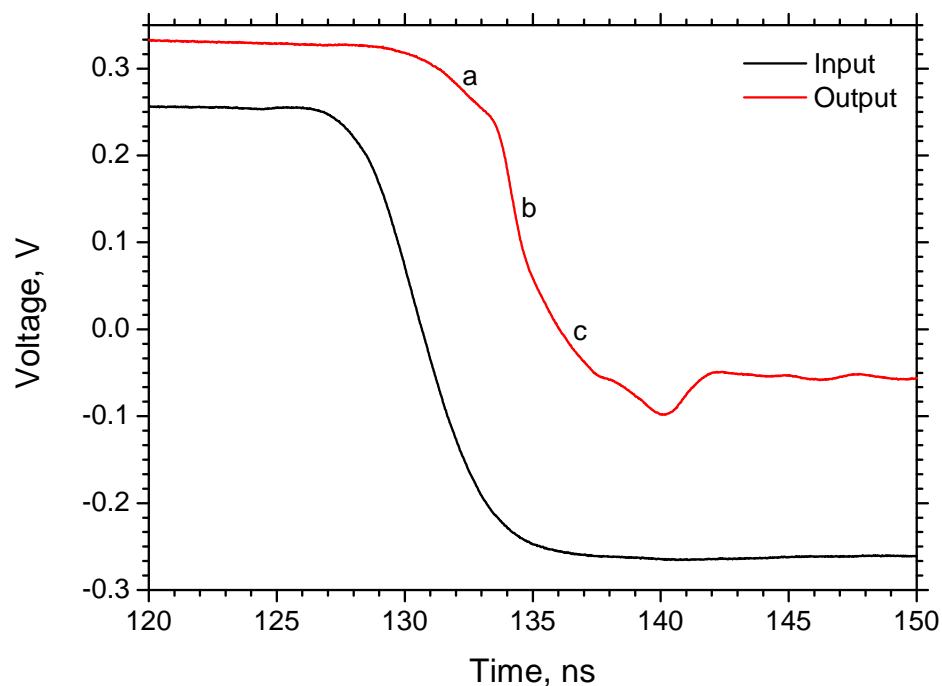


**Figure 6.3:** Test for pulse sharpening using a 200  $\mu\text{m}$  diameter step recovery diode fabricated from wafer Mn775. The output trace shows the characteristics of a poor step recovery diode with pronounced “slow tail” and “round off” features marked as “a” and “c”, respectively. The fast transition at “b” has a steeper gradient than the input pulse.

should ideally be less than the minority carrier lifetime in the intrinsic layer [134]. A signal generator that can produce voltage pulses with a rise time of  $<5$  ns should be used for these experiments.

As there is a fast transition present in the response of the diode it is possible that the internal workings of the diode are still sufficiently fast to generate a strain pulse. It is likely that it is just the overall transition time that is limited by the round off and slow tail portions of the signal.

Preliminary experiments were performed to see if the SRD could generate a strain pulse that would then propagate across the substrate of the sample. A superconducting Al bolometer fabricated directly opposite the SRD to be tested was used as the detector. The SRD was mounted inside a bath cryostat that had the temperature control required to hold the bolometer on its superconducting transition. A voltage pulse was applied

to the SRD, and the bolometer signal was observed at a time that would correspond to phonons emitted from the SRD during the falling edge of the voltage pulse reaching the bolometer on the other side of the substrate. However, the bolometer signal was saturated due to heating caused by the large voltage pulse needed to drive the SRD, and this made it impossible to determine if there was an increase in the bolometer signal at the expected time.

Instead, it should be possible to perform the experiment using a *p-i-n* detector with a quantum well in the intrinsic region. It was shown by Moss *et al.* that when probed with a suitable laser these devices produced a photocurrent that followed the transient ultrafast strain propagating through the *p-i-n* detector [43, 44]. For this experiment to be successful it is necessary to be able to phase-lock the voltage pulses driving the SRD with the laser pulses that form the photocurrent in the QW. A constant phase relationship between the two pulses is required when averaging the signal over multiple pulses to improve the signal-to-noise ratio.

### 6.3 Summary

In summary, the experiments performed in this thesis were successful in the electrical detection of ultrafast acoustic pulses using semiconductor devices. Heterodyne mixing of the acoustic frequency with that of a microwave source has been demonstrated using a Schottky diode as the mixer element, and semiconductor superlattice structures also look promising for this application.

There are several areas of research left open for future work, the most important perhaps being the electrical generation of ultrafast strain pulses to compliment the electrical detection techniques. The step recovery diode is a potential candidate for this role, and some preliminary experiments have been performed on these devices.

# Bibliography

- [1] C. Thomsen, H. T. Grahn, H. J. Maris, and J. Tauc. Surface generation and detection of phonons by picosecond light pulses. *Physical Review B*, 34:4129, 1986.
- [2] O. B. Wright. Ultrafast nonequilibrium stress generation in gold and silver. *Physical Review B*, 49:9985, 1994.
- [3] G. Tas and H. J. Maris. Electron diffusion in metals studied by picosecond ultrasonics. *Physical Review B*, 49:15046, 1994.
- [4] O. B. Wright and V. E. Gusev. Ultrafast generation of acoustic waves in copper. *IEEE Transactions on Ultrasonics, Ferroelectrics and Frequency Control*, 42:331, 1995.
- [5] T. Saito, O. Matsuda, and O. B. Wright. Picosecond acoustic phonon pulse generation in nickel and chromium. *Physical Review B*, 67:205421, 2003.
- [6] O. B. Wright, B. Perrin, O. Matsuda, and V. E. Gusev. Ultrafast carrier diffusion in gallium arsenide probed with picosecond acoustic pulses. *Physical Review B*, 64:081202, 2001.
- [7] P. Babilotte, P. Ruello, D. Mounier, T. Pezeril, G. Vaudel, M. Edely, J-M. Breteau, V. Gusev, and K. Blary. Femtosecond laser generation and detection of high-frequency acoustic phonons in GaAs semiconductors. *Physical Review B*, 81:245207, 2010.
- [8] E. S. K. Young, A. V. Akimov, R. P. Champion, and A. J. Kent. Picosecond strain pulses generated by a supersonically expanding electron-hole plasma in GaAs. *Physical Review B*, 86:155207, 2012.

- [9] H. -N. Lin, R. J. Stoner, H. J. Maris, and J. Tauc. Phonon attenuation and velocity measurements in transparent materials by picosecond acoustic interferometry. *Journal of Applied Physics*, 69:3816, 1991.
- [10] B. Perrin, C. Rossignol, B. Bonello, and J. -C. Jeannet. Interferometric detection in picosecond ultrasonics. *Physica B: Condensed Matter*, 263-264:571, 1999.
- [11] O. B. Wright. Thickness and sound velocity measurement in thin transparent films with laser picosecond acoustics. *Journal of Applied Physics*, 71:1617, 1992.
- [12] H. T. Grahn, H. J. Maris, and J. Tauc. Picosecond ultrasonics. *IEEE Journal of Quantum Electronics*, 25:2562, 1989.
- [13] W. Chen, H. J. Maris, Z. R. Wasilewski, and S. Tamura. Attenuation and velocity of 56 GHz longitudinal phonons in gallium arsenide from 50 to 300 K. *Philosophical Magazine B*, 70:687, 1994.
- [14] H. -Y. Hao and H. J. Maris. Study of phonon dispersion in silicon and germanium at long wavelengths using picosecond ultrasonics. *Physical Review Letters*, 84:5556, 2000.
- [15] H. -Y. Hao and H. J. Maris. Dispersion of the long-wavelength phonons in Ge, Si, GaAs, quartz, and sapphire. *Physical Review B*, 63:224301, 2001.
- [16] B. C. Daly, T. B. Norris, J. Chen, and J. B. Khurgin. Picosecond acoustic phonon pulse propagation in silicon. *Physical Review B*, 70:214307, 2004.
- [17] H. -Y. Hao and H. J. Maris. Experiments with acoustic solitons in crystalline solids. *Physical Review B*, 64:064302, 2001.
- [18] E. Péronne and B. Perrin. Generation and detection of acoustic solitons in crystalline slabs by laser ultrasonics. *Ultrasonics*, 44:e1203, 2006.
- [19] P. J. S. van Capel and J. I. Dijkhuis. Time-resolved interferometric detection of ultrashort strain solitons in sapphire. *Physical Review B*, 81:144106, 2010.

- [20] C. J. Morath and H. J. Maris. Phonon attenuation in amorphous solids studied by picosecond ultrasonics. *Physical Review B*, 54:203, 1996.
- [21] G. Tas and H. J. Maris. Picosecond ultrasonic study of phonon reflection from solid-liquid interfaces. *Physical Review B*, 55:1852, 1997.
- [22] C. Rossignol, N. Chigarev, M. Ducouso, B. Audoin, G. Forget, F. Guillemot, and M. C. Durrieu. *In Vitro* picosecond ultrasonics in a single cell. *Applied Physics Letters*, 93:123901, 2008.
- [23] A. Bartels, T. Dekorsy, H. Kurz, and K. Köhler. Coherent zone-folded longitudinal acoustic phonons in semiconductor superlattices: excitation and detection. *Physical Review Letters*, 82:1044, 1999.
- [24] D. M. Moss, A. V. Akimov, A. J. Kent, B. A. Glavin, M. J. Kappers, J. L. Hollander, M. A. Moram, and C. J. Humphreys. Coherent terahertz acoustic vibrations in polar and semipolar gallium nitride-based superlattices. *Applied Physics Letters*, 94:011909, 2009.
- [25] P. M. Walker, J. S. Sharp, A. V. Akimov, and A. J. Kent. Coherent elastic waves in a one-dimensional polymer hypersonic crystal. *Applied Physics Letters*, 97:073106, 2010.
- [26] A. V. Akimov, E. S. K. Young, J. S. Sharp, V. Gusev, and A. J. Kent. Coherent hypersonic closed-pipe organ like modes in supported polymer films. *Applied Physics Letters*, 99:021912, 2011.
- [27] D. J. Farmer, A. V. Akimov, J. S. Sharp, and A. J. Kent. Quantized phonon modes in loaded polymer films. *Journal of Applied Physics*, 113:033516, 2013.
- [28] A. V. Akimov, A. V. Scherbakov, D. R. Yakovlev, C. T. Foxon, and M. Bayer. Ultrafast band-gap shift induced by a strain pulse in semiconductor heterostructures. *Physical Review Letters*, 97:037401, 2006.
- [29] R. P. Beardsley, A. V. Akimov, M. Henini, and A. J. Kent. Coherent terahertz sound amplification and spectral line narrowing in a Stark ladder superlattice. *Physical Review Letters*, 104:085501, 2010.

- [30] G. Weinreich and H. G. White. Observation of the acoustoelectric effect. *Physical Review*, 106:1104, 1957.
- [31] G. Weinreich, T. M. Sanders, and H. G. White. Acoustoelectric effect in *n*-type germanium. *Physical Review*, 114:33, 1959.
- [32] I. L. Auerbach, J. Presper Eckert, R. F. Shaw, and C. Bradford Shepard. Mercury delay line memory using a pulse rate of several megacycles. *Proceedings of the IRE*, 37:855, 1949.
- [33] R. M. White and F. W. Voltmer. Direct piezoelectric coupling to surface elastic waves. *Applied Physics Letters*, 7:314, 1965.
- [34] O. Ikata, T. Miyashita, T. Matsuda, T. Nishihara, and Y. Satoh. Development of low-loss band-pass filters using SAW resonators for portable telephones. In *Ultrasonics Symposium, Proceedings, IEEE*, 1992.
- [35] F. Bénédic, M. B. Assouar, P. Kirsch, D. Monéger, O. Brinza, O. Elmazria, P. Alnot, and A. Gicquel. Very high frequency SAW devices based on nanocrystalline diamond and aluminium nitride layered structure achieved using e-beam lithography. *Diamond & Related Materials*, 17:804, 2008.
- [36] A. Mauder. SAW gas sensors: comparison between delay line and two port resonator. *Sensors and Actuators, B: Chemical*, 26-27:187, 1995.
- [37] A. T. Nimal, M. Singh, U. Mittal, and R. D. S Yadava. A comparative analysis of one-port Colpitt and two-port Pierce SAW oscillators for DMMP vapor sensing. *Sensors and Actuators, B: Chemical*, 114.1:316, 2006.
- [38] L. Reindl, G. Scholl, T. Ostertag, C. C. W. Ruppel, W. -E. Bulst, and F. Seifert. SAW devices as wireless passive sensors. In *Ultrasonics Symposium, Proceedings, IEEE*, 1996.
- [39] A. Pohl. A review of wireless SAW sensors. *IEEE Transactions on Ultrasonics, Ferroelectrics and Frequency Control*, 47:317, 2000.
- [40] V. I. Talyanskii, J. M. Shilton, M. Pepper, C. G. Smith, C. J. B. Ford, E. H. Linfield, D. A. Ritchie, and G. A. C. Jones. Single-

electron transport in a one-dimensional channel by high-frequency surface acoustic waves. *Physical Review B*, 56:15 180, 1997.

- [41] A. B. Hutchinson, V. I. Talyanskii, M. Pepper, G. Gumbs, G. R. Aizin, D. A. Ritchie, and E. H. Linfield. Nonlinear interaction between surface acoustic waves and electrons in GaAs resonant-tunneling structures. *Physical Review B*, 62:6948, 2000.
- [42] D. R. Fowler, A. V. Akimov, A. G. Balanov, M. T. Greenaway, M. Henini, T. M. Fromhold, and A. J. Kent. Semiconductor charge transport driven by a picosecond strain pulse. *Applied Physics Letters*, 92:232104, 2008.
- [43] D. Moss, A. V. Akimov, O. Makarovskiy, R. P. Champion, C. T. Foxon, L. Eaves, A. J. Kent, and B. A. Glavin. Ultrafast acoustical gating of the photocurrent in a  $p$ - $i$ - $n$  tunneling diode incorporating a quantum well. *Physical Review B*, 80:113306, 2009.
- [44] D. Moss, A. V. Akimov, R. P. Champion, M. Henini, C. T. Foxon, L. Eaves, A. J. Kent, and B. A. Glavin. Picosecond strain pulses probed by the photocurrent in semiconductor devices with quantum wells. *Physical Review B*, 83:245303, 2011.
- [45] D. Moss. *Ultrafast acoustic modulation of transport in semiconductor devices*. PhD thesis, The University of Nottingham, 2012.
- [46] D. M. Moss, A. V. Akimov, R. P. Champion, and A. J. Kent. Ultrafast strain-induced electronic transport in a GaAs  $p$ - $n$  junction diode. *Chinese Journal of Physics*, 49:499, 2011.
- [47] D. M. Moss, A. V. Akimov, B. A. Glavin, M. Henini, and A. J. Kent. Ultrafast strain-induced current in a GaAs Schottky diode. *Physical Review Letters*, 106:06602, 2011.
- [48] E. S. K. Young, A. V. Akimov, M. Henini, L. Eaves, and A. J. Kent. Subterahertz acoustical pumping of electronic charge in a resonant tunneling device. *Physical Review Letters*, 108:226601, 2012.
- [49] A. Huynh, B. Perrin, N. D. Lanzillotti-Kimura, B. Jusserand, A. Fainstein, and A. Lemaître. Subterahertz monochromatic acoustic wave propagation using semiconductor superlattices as transducers. *Physical Review B*, 78:233302, 2008.

- [50] R. Beardsley, A. V. Akimov, B. A. Glavin, W. Maryam, M. Henini, and A. J. Kent. Optical detection of folded mini-zone-edge coherent acoustic modes in a doped GaAs/AlAs superlattice. *Physical Review B*, 82:041302, 2010.
- [51] S. A. Cavill, L. J. Challis, A. J. Kent, F. F. Ouali, A. V. Akimov, and M. Henini. Acoustic phonon-assisted tunneling in GaAs/AlAs superlattices. *Physical Review B*, 66:235320, 2002.
- [52] R. N. Kini, A. J. Kent, N. M. Stanton, and M. Henini. Angle dependence of acoustic phonon-assisted tunneling in a weakly coupled superlattice: evidence for terahertz phonon amplification. *Journal of Applied Physics*, 98:033514, 2005.
- [53] C. L. Poyser, A. V. Akimov, A. G. Balanov, R. P. Champion, and A. J. Kent. A weakly coupled semiconductor superlattice as a harmonic hypersonic-electrical transducer. *New Journal of Physics*, 17:083064, 2015.
- [54] A. Yamamoto, T. Mishina, Y. Masumoto, and M. Nakayama. Coherent oscillation of zone-folded phonon modes in GaAs-AlAs superlattices. *Physical Review Letters*, 73:740, 1994.
- [55] K. Mizoguchi, M. Hase, S. Nakashima, and M. Nakayama. Observation of coherent folded acoustic phonons propagating in a GaAs/AlAs superlattice by two-color pump-probe spectroscopy. *Physical Review B*, 60:8262, 1999.
- [56] P. Hawker, A. J. Kent, L. J. Challis, A. Bartels, T. Dekorsy, H. Kurz, and K. Köhler. Observation of coherent zone-folded acoustic phonons generated by Raman scattering in a superlattice. *Applied Physics Letters*, 77:3209, 2000.
- [57] R. J. von Gutfeld and A. H. Nethercot Jr. Heat pulses in quartz and sapphire at low temperatures. *Physical Review Letters*, 12:641, 1964.
- [58] B. Taylor, H. J. Maris, and C. Elbaum. Phonon focusing in solids. *Physical Review Letters*, 23:416, 1969.
- [59] S. Tamura, D. C. Hurley, and J. P. Wolfe. Acoustic-phonon propagation in superlattices. *Physical Review B*, 38:1427, 1988.

- [60] D. Lehmann, A. J. Kent, Cz. Jasiukiewicz, A. J. Cross, P. Hawker, and M. Henini. Effects of acoustic anisotropy and screening on the energy relaxation of hot electrons in heterojunctions and quantum wells. *Physical Review B*, 65:085320, 2002.
- [61] R. J. von Gutfeld. *Physical acoustics: principles and methods*, volume V. Academic Press, 1968.
- [62] J. P. Wolfe. *Imaging phonons: acoustic wave propagation in solids*. Cambridge University Press, 1998.
- [63] B. Perrin, E. Péronne, and L. Belliard. Generation and detection of incoherent phonons in picosecond ultrasonics. *Ultrasonics*, 44:e1277, 2006.
- [64] N. M. Stanton and A. J. Kent. Propagation of high amplitude strain pulses in sapphire. *Physical Review B*, 73:220301, 2006.
- [65] H. J. Maris. *Physical acoustics: principles and methods*, volume VIII. Academic Press, 1971.
- [66] J. L. T. Waugh and G. Dolling. Crystal dynamics of gallium arsenide. *Physical Review*, 132:2410, 1963.
- [67] J. S. Blakemore. Semiconducting and other major properties of gallium arsenide. *Journal of Applied Physics*, 53:R123, 1982.
- [68] A. J. Kent and N. M. Stanton. Bolometric detection of picosecond acoustic pulses in silicon and gallium arsenide. *Journal of Physics: Conference series*, 92:012004, 2007.
- [69] R. P. Beardsley, R. P. Champion, B. A. Glavin, and A. J. Kent. A GaAs/AlAs superlattice as an electrically pumped THz acoustic phonon amplifier. *New Journal of Physics*, 13:073007, 2011.
- [70] W. Maryam, A. V. Akimov, R. P. Champion, and A. J. Kent. Dynamics of a vertical cavity quantum cascade phonon laser structure. *Nature Communications*, 4(2184), 2013.
- [71] J. Bardeen and W. Shockley. Deformation potentials and mobilities in non-polar crystals. *Physical Review*, 80:72, 1950.

- [72] D. J. Robbins. *Properties of gallium arsenide*. Institution of Engineering and Technology, 1996.
- [73] S. I. Pekar. Electron-phonon interaction proportional to the external applied field and sound amplification in semiconductors. *Soviet Physics JETP*, 22:431, 1966.
- [74] B. A. Glavin, V. A. Kochelap, T. L. Linnik, and K. W. Kim. Electron-phonon interaction via the pekar mechanism in nanostructures. *Physical Review B*, 71:081305, 2005.
- [75] P. A. Knipp and T. L. Reinecke. Coupling between electrons and acoustic phonons in semiconductor nanostructures. *Physical Review B*, 52:5923, 1995.
- [76] S. Zollner and M. Cardona. *Properties of gallium arsenide*. Institution of Engineering and Technology, 1996.
- [77] D. D. Nolte, W. Walukiewicz, and E. E. Haller. Band-edge hydrostatic deformation potentials in III-V semiconductors. *Physical Review Letters*, 59:501, 1987.
- [78] C. G. Van de Walle. Band lineups and deformation potentials in the model-solid theory. *Physical Review B*, 39:1871, 1989.
- [79] I. Vurgaftman, J. R. Meyer, and L. R. Ram-Mohan. Band parameters for III-V compound semiconductors and their alloys. *Journal of Applied Physics*, 89:5815, 2001.
- [80] S. Adachi. GaAs, AlAs, and  $\text{Al}_x\text{Ga}_{1-x}\text{As}$ : material parameters for use in research and device applications. *Journal of Applied Physics*, 58:R1, 1985.
- [81] G. Arlt and P. Quadflieg. Piezoelectricity in III-V compounds with a phenomenological analysis of the piezoelectric effect. *Physica Status Solidi B: Basic Solid State Physics*, 25:323, 1968.
- [82] E. S. K. Young. *Ultrafast acoustic strain generation and effects in semiconductor nanostructures*. PhD thesis, The University of Nottingham, 2014.
- [83] M. Herzog, A. Bojahr, J. Goldshteyn, W. Leitenberger, I. Vrejoiu, D. Khakhulin, M. Wulff, R. Shayduk, P. Gaal, and M. Bargheer.

- Detecting optically synthesized quasi-monochromatic sub-terahertz phonon wavepackets by ultrafast x-ray diffraction. *Applied Physics Letters*, 100:094101, 2012.
- [84] J. D. Choi, T. Feurer, M. Yamaguchi, B. Paxson, and K. A. Nelson. Generation of ultrahigh-frequency tunable acoustic waves. *Applied Physics Letters*, 87:081907, 2005.
- [85] S. Lucyszyn, J. Luck, G. Green, and I. D. Robertson. Enhanced modelling of interdigitated planar Schottky varactor diodes. *Microwave Conference APMC Asia-Pacific*, 1:273, 1992.
- [86] I. A. Glover, S. R. Pennock, and P. R. Shepherd, editors. *Microwave devices, circuits and subsystems for communications engineering*. John Wiley & Sons Ltd, 2005.
- [87] E. N. Grossman, L. R. Vale, D. A. Rudman, K. M. Evenson, and L. R. Zink. 30 THz mixing experiments on high temperature superconducting Josephson junctions. *IEEE Transactions on Applied Superconductivity*, 5:3061, 1995.
- [88] P. H. Seigel. Terahertz technology. *IEEE Transactions on Microwave Theory and Techniques*, 50:910, 2002.
- [89] James J. Brophy. *Basic electronics for scientists*. McGraw-Hill, 5th edition, 1990.
- [90] A. Maestrini, B. Thomas, H. Wang, C. Jung, J. Treuttel, Y. Jin, G. Chattopadhyay, I. Mehdi, and G. Beaudin. Schottky diode-based terahertz frequency multipliers and mixers. *Comptes Rendus Physique*, 11:480, 2010.
- [91] S. Marcus and J. W. Caunt. Compact CO<sub>2</sub> laser for infrared heterodyne radar. *Review of Scientific Instruments*, 49:1410, 1978.
- [92] D. T. Petkie, C. Benton, and E. Bryan. Millimeter wave radar for remote measurement of vital signs. *Radar Conference, 2009, IEEE*, 2009.
- [93] S. M. Sze and K. K. Ng. *Physics of semiconductor devices*. Wiley, 3rd edition, 1981.

- [94] B. G. Streetman. *Solid state electronic devices*. Prentice-Hall, Inc, 4th edition, 1995.
- [95] A. G. Baca and C. I. H. Ashby. *Fabrication of GaAs devices*. The Institution of Engineering and Technology, 2009.
- [96] L. Donetti, F. Gámiz, J. B. Roldán, and A. Godoy. Acoustic phonon confinement in silicon nanolayers: Effect on electron mobility. *Journal of Applied Physics*, 100:013701, 2006.
- [97] K. G. Hambleton, C. Hilsum, and B. R. Holeman. Determination of the effective ionic charge of gallium arsenide from direct measurements of the dielectric constant. *Proceedings of the Physical Society*, 77:1147, 1961.
- [98] S. Ramo, J. R. Whinnery, and T. Van Duzer. *Fields and waves in communication electronics*. John Wiley & Sons, third edition, 1994.
- [99] W. He, R. Jin, and J. Geng. E-shape patch with wideband and circular polarization of millimeter-wave communication. *IEEE Transactions on Antennas and Propagation*, 56:893, 2008.
- [100] Q. Wu, R. Jin, and J. Geng. A single-layer ultrawideband microstrip antenna. *IEEE Transactions on Antennas and Propagation*, 58:211, 2010.
- [101] G. P. Gauthier, J. P. Raskin, L. P. B. Katechi, and G. M. Rebeiz. A 94-GHz aperture-coupled micromachined microstrip antenna. *IEEE Transactions on Antennas and Propagation*, 47:1761, 1999.
- [102] C. R. Trent and T. M. Weller. Design and tolerance analysis of a 21 GHz CPW-fed, slot-coupled, microstrip antenna on etched silicon. In *Antennas and Propagation Society International Symposium, Proceedings, IEEE*, volume 1, page 402, 2002.
- [103] H. C. Casey, D. D. Sell, and K. W. Wecht. Concentration dependence of the absorption coefficient for  $n$ - and  $p$ - type GaAs between 1.3 and 1.6 eV. *Journal of Applied Physics*, 46:205, 1975.
- [104] R. Marty, A. Arbouet, C. Girard, A. Mlayah, V. Paillard, V. K. Lin, S. L. Teo, and S. Tripathy. Damping of the acoustic vibrations of individual gold nanoparticles. *Nano Letters*, 11:3301, 2011.

- [105] O. Matsuda, T. Tachizaki, T. Fukui, J. J. Baumberg, and O. B. Wright. Acoustic phonon generation and detection in GaAs/Al<sub>0.3</sub>Ga<sub>0.7</sub>As quantum wells with picosecond laser pulses. *Physical Review B*, 71:115330, 2005.
- [106] R. Poore. Overview on phase noise and jitter. *Agilent EEsof EDA*, 2001.
- [107] K. F. Riley, M. P. Hobson, and S. J. Bence. *Mathematical methods for physics and engineering*. Cambridge University Press, 3rd edition, 2006.
- [108] H. T. Grahn, editor. *Semiconductor superlattices: growth and electronic properties*. World Scientific, 1995.
- [109] L. Esaki and R. Tsu. Superlattice and negative differential conductivity in semiconductors. *IBM Journal of Research and Development*, 14:61, 1970.
- [110] L. Esaki and L. L. Chang. New transport phenomenon in a semiconductor “superlattice”. *Physical Review Letters*, 33:495, 1974.
- [111] R. Tsu and G. Döhler. Hopping conduction in a “superlattice”. *Physical Review B*, 12:680, 1975.
- [112] A. Wacker and A. P. Jauho. Quantum transport: the link between standard approaches in superlattices. *Physical Review Letters*, 80:369, 1998.
- [113] A. Wacker. Semiconductor superlattices: a model system for nonlinear transport. *Physics Reports*, 357:1, 2002.
- [114] L. L. Bonilla and H. T. Grahn. Non-linear dynamics of semiconductor superlattices. *Reports on Progress of Physics*, 68:577, 2005.
- [115] V. Narayanamurti, H. L. Störmer, M. A. Chin, A. C. Gossard, and W. Wiegmann. Selective transmission of high-frequency phonons by a superlattice: the “dielectric” phonon filter. *Physical Review Letters*, 43:2012, 1979.
- [116] C. Colvard, T. A. Gant, M. V. Klein, R. Merlin, R. Fischer, H. Morkoc, and A. C. Gossard. Folded acoustic and quantized op-

- tic phonons in (GaAl)As superlattices. *Physical Review B*, 31:2080, 1985.
- [117] M. Trigo, A. Bruchhausen, A. Fainstein, B. Jusserand, and V. Thierry-Mieg. Confinement of acoustical vibrations in a semiconductor planar phonon cavity. *Physical Review Letters*, 89:227402, 2002.
- [118] A. J. Kent, R. N. Kini, N. M. Stanton, M. Henini, B. A. Glavin, V. A. Kochelap, and T. L. Linnik. Acoustic phonon emission from a weakly coupled superlattice under vertical electron transport: observation of phonon resonance. *Physical Review Letters*, 96:215504, 2006.
- [119] R. Beardsley. *Coherent phonon processes in semiconductor superlattices*. PhD thesis, The University of Nottingham, 2011.
- [120] W. M. W. A. Kamil. *The study of THz vertical cavity SASER devices*. PhD thesis, The University of Nottingham, 2013.
- [121] E. Schomburg, K. Hofbeck, J. Grenzer, T. Blomeier, A. A. Ignatov, K. F. Renk, D. G. Pavel'ev, Yu. Koschurinov, V. Ustinov, A. Zhukov, S. Ivanov, and P. S. Kop'ev. Millimeter wave oscillator based on a quasiplanar superlattice electronic device. *Applied Physics Letters*, 71:401, 1997.
- [122] S. Winnerl, E. Schomburg, S. Brandl, O. Kus, K. F. Renk, M. C. Wanke, S. J. Allen, A. A. Ignatov, V. Ustinov, A. Zhukov, and P. S. Kop'ev. Frequency doubling and tripling of terahertz radiation in a GaAs/AlAs superlattice due to frequency modulation of Bloch oscillations. *Applied Physics Letters*, 77:1259, 2000.
- [123] F. Klappenberger, A. A. Ignatov, S. Winnerl, E. Schomburg, W. Wegscheider, K. F. Renk, and M. Bichler. Broadband semiconductor superlattice detector for THz radiation. *Applied Physics Letters*, 78:1673, 2001.
- [124] S. M. Rytov. Acoustical properties of a thinly laminated medium. *Soviet Physics Acoustics*, 2:68, 1956.
- [125] J. I. Climente, A. Bertoni, G. Goldoni, and E. Molinari. Phonon-induced electron relaxation in weakly confined single and coupled quantum dots. *Physical Review B*, 74:035313, 2006.

- [126] C. Kittel. *Introduction to solid state physics*. John Wiley & Sons, 6th edition, 1986.
- [127] Vadim Siklitsky, 2001. <http://www.ioffe.ru/SVA/NSM/Semicond/> (Accessed: 18 September 2015).
- [128] J. Batey and S. L. Wright. Energy band alignment in GaAs:(Al,Ga)As heterostructures: the dependence on alloy composition. *Journal of Applied Physics*, 59:200, 1986.
- [129] B. A. Glavin, V. A. Kochelap, and T. L. Linnik. Current response of a superlattice irradiated with nonequilibrium phonons. *JETP Letters*, 71:191, 2000.
- [130] A. J. Kent and J. K. Wigmore. *Electron-phonon interactions in low-dimensional structures*. Oxford University Press, 2003.
- [131] K. F. Renk, B. I. Stahl, A. Rogl, T. Janzen, D. G. Pavel'ev, Yu. I. Koshurinov, V. Ustinov, and A. Zhukov. Subterahertz superlattice parametric oscillator. *Physical Review Letters*, 95:126801, 2005.
- [132] C. P. Endres, F. Lewen, T. F. Giesen, S. Schlemmer, D. G. Paveliev, Y. I. Koschurinov, V. M. Ustinov, and A. E. Zhucov. Application of superlattice multipliers for high-resolution terahertz spectroscopy. *Review of Scientific Instruments*, 78:043106, 2007.
- [133] J. L. Moll and S. A Hamilton. Physical modeling of the step recovery diode for pulse and harmonic generation circuits. *Proceedings of the IEEE*, 57:1250, 1969.
- [134] M. R. T. Tan, S. T. Wang, D. E. Mars, and J. L. Moll. A 12 psec GaAs double heterostructure step recovery diode. *Electronics Letters*, 28:673, 1992.
- [135] F. Ao, A. Hovinen, M. Taskinen, J. Zhang, P. Kuivalainen, and A. Räisänen. GaAs double heterostructure step recovery diode. *Physica Scripta*, T79:334, 1999.

# Appendix A

## Processing instructions

Several different semiconductor devices were fabricated in the clean room within the School of Physics at the University of Nottingham for use in the experiments described in this thesis. The processing steps for these devices are outlined in this appendix. Four different processes will be described: two Schottky diode structures, one set of superlattice devices and the step recovery diodes. All four processes used different photolithography mask sets.

### A.1 Common processing steps

Many of the processing steps are common to all of the devices fabricated within the university clean room. These will be outlined in this section, and then simply referred to in the following sections where the process flows for specific devices are outlined.

**Four solvent clean:** The sample was immersed in four different solvents for 10 minutes each in the following order: ethyl lactate, acetone, methanol and isopropyl alcohol. This was done at room temperature, and the beaker was typically placed on a stirring plate for gentle agitation. After the sample was removed from a solvent it was then rinsed with the appropriate solvent and dried with pressurised nitrogen. The exception to this was after removing the sample from the

acetone. Drying the sample after the acetone step can lead to leaving deposited material on the sample, so the sample was transferred from acetone to methanol without being dried.

**Three solvent clean:** After the initial clean, only the latter three solvents were required for subsequent cleaning steps: acetone, methanol and isopropyl alcohol. The same general method was followed as for the four solvent clean, except that the first solvent used was acetone.

**Dehydration:** The sample was dehydrated after cleaning if the following step was to involve resist work. Dehydration of the sample was performed to drive off excess solvents and ensure good adhesion of the resist. This was done at a temperature higher than the temperature used to bake the resist. If the resist was to be baked in the oven, the sample was dehydrated in the oven at 150°C for 10 minutes. If the resist was to be baked on the hotplate, the sample was dehydrated on the hotplate at 120°C for 10 minutes.

**Spinning resist:** The same positive resist, BPRS 150, was used for all devices. This was applied using a pipette, ensuring that there were no bubbles present in the resist. It was then spun at 4000 rpm for 30 s. This typically led to a resist thickness of 1.4-1.6  $\mu\text{m}$ . Spinning resist onto small rectangular samples leads to a large amount of edge-bead building up in the resist, especially at the corners. A clean room appropriate cotton bud can be used to remove the worst of the edge-bead from the corners of the sample. If not removed, this edge-bead can stick to the photolithography mask, making alignment tricky, or it can prevent the mask from making good contact with the resist and lead to a poorly defined pattern.

**Baking resist:** The BPRS 150 resist could either be baked in the oven at 110°C for 30 minutes or on the hotplate at 90°C for 2 minutes. Initially the resist was always baked in the oven, as it was suggested that this method made the lift-off stage easier. In later processes the hotplate was used, as it was found that it didn't have a noticeable detrimental effect during lift-off and it reduced the time of the resist steps considerably.

**Patterning the sample:** After the resist was baked, it was patterned using photolithography. The mask was aligned to any pre-existing

pattern on the sample using a Karl Suss MJB3 mask aligner. The sample was given a 6 s exposure of the UV light on the constant intensity setting with an intensity of  $10 \text{ mW cm}^{-2}$ .

**Developing the pattern:** After patterning the sample using the mask aligner, the pattern had to be developed. As the same resist was used for all patterning steps, the same developing solution was also used. The developer used was AZ400K diluted 1:8 with deionised water. The sample was held in the developer using tweezers, and moved forward and backward gently. The sample was removed from the developer after a given time, rinsed with deionised water and then dried with pressurised nitrogen. A typical development time was between 30 s and 120 s. The pattern was checked under an optical microscope after an initial 30 s, and if it looked under-developed it was put back in the developing solution and checked again until it appeared well-developed.

**Etching to remove material:** Before starting the etch process, the thickness of the resist pattern was measured using a height profiler. This was important to later determine how much material had been removed. The etch solution was made fresh each time. The sample was then held in the etch solution using tweezers and gently moved forward and backward. After a given time the sample was removed from the etch solution and placed in a beaker of deionised water, before being rinsed with fresh deionised water and dried with pressurised nitrogen. The etch depth was measured on a height profiler. Subtracting the resist thickness from the total step change measured allowed the etch depth to be determined. An approximate etch rate was calculated and the previous steps were repeated until the required etch depth was reached.

The etch solution used was 1:1:100 hydrogen peroxide ( $\text{H}_2\text{O}_2$ ), ammonia ( $\text{NH}_3$ ) and deionised water. This was used in previous work by Ryan Beardsley and gave an average etch rate of  $4 \text{ nm s}^{-1}$ .

**Resist removal:** The BPRS 150 resist could be easily removed in acetone. The sample was soaked in acetone at room temperature. This was typically followed by a three solvent clean to remove any resist residues.

**Oxide etch:** To ensure the formation of good electrical contacts, an oxide etch was performed on the sample before it was loaded into the thermal evaporator. The etch solution was made up of 1:1 hydrochloric acid (HCl) to water. The sample was held in the oxide etch using tweezers and gently agitated for 1 minute. It was then rinsed with deionised water and dried with pressurised nitrogen before being loaded into the evaporator.

**Metal deposition:** The metals that were to be deposited onto the sample needed to be cleaned prior to loading them into the evaporator. This was done using the three solvent clean process, but the beaker was placed in an ultrasonic bath to aid the cleaning process. Once loaded, the evaporator was left to pump down to a suitable pressure. Ideally, the lower the pressure the better, as there are less contaminants remaining within the bell jar. This was typically in the low  $10^{-6}$  mbar to high  $10^{-7}$  mbar range.

For *n*-type metal contacts, a layer of In/Ge 50:50 by mass and a layer of Au were commonly deposited, following on from previous processes performed by Ryan Beardsley. These metals were initially chosen as the metals are thought to diffuse less far into the material compared to the Ge Au Ni Au contact typically used within the School's clean room. This can be important for vertical transport devices, as you do not want the contact metals to diffuse beyond the top contact layer. For the NU1778 superlattice sample, the In/Ge evaporation was not available as the evaporator used for this process had been removed from the clean room. As In evaporations are considered a "dirty" process, In was no longer used in any of the School evaporators.

For the *p*-type ohmic contact required in the Mn775 step recovery diode process, Mg and Au were used to form the contact. This type of contact had frequently been successfully used within the School.

**Lift-off:** The sample was soaked in a beaker of acetone to remove the resist and the material deposited on top of the resist. This was typically followed by a three solvent clean to remove any resist residues.

## A.2 Mn659 Schottky diodes

The Mn659 wafer had an  $n$ -doped GaAs layer grown on one side, as shown in figure 4.3. This is the side that was used to create Schottky diodes. The back face of the sample had a superlattice structure grown on it that needed to be protected from being etched.

The mask set used for these devices was a printed acetate mask. It has not been stored in the clean room, and would probably need replacing to recreate these devices.

1. Scribe and cleave the sample into chips approximately 5 mm  $\times$  5 mm.
2. Four solvent clean and dehydrate.
3. Stick to a glass cover slip to protect the superlattice on the back face during wet etching. Use BPRS 150 resist and a pipette tip to place a small dot of resist on the glass cover slip. Place the sample on top of the resist and bake on the hot plate at 90°C for 1 minute. Check that there are no bubbles, especially near the edges of the sample.
4. Spin on resist and bake.
5. Pattern with the etch mask pattern and develop. This pattern creates two mesas per device, so there were two triangles of resist left per device after the developing stage. We only wanted one mesa per device, so a second exposure was used. To do this, we covered the row of resist triangles that we wanted to keep and exposed the ones we didn't. The sample was developed a second time.
6. Etch the mesas. Need to remove 500 nm.
7. Resist removal, followed by a three solvent clean and then dehydrate the sample. Soaking the sample in acetone to remove the resist will also free the sample from the glass cover slip.
8. Spin on resist and bake.
9. Pattern with the ohmic contact mask and develop. This mask creates two slightly smaller triangles than the etch mask where the ohmic contacts should be formed. As we only had one mesa per device, one

contact was the ohmic contact on top of the mesa and the other was formed on the semi-insulating substrate. This second triangle will later be connected to the Schottky contact to act as half of the bow-tie antenna, but also to act as a large bonding pad for the Schottky contact.

10. Oxide etch before loading the sample into the evaporator.
11. Thermally evaporate 40 nm of In/Ge 50:50 by mass followed by 110 nm of Au.
12. Lift-off and three solvent clean.
13. Anneal ohmic contact at 370°C for 30 s.
14. Three solvent clean and dehydrate.
15. Spin on resist and bake.
16. Pattern with the Schottky contact mask. This is a row of strips of different width to connect the top of the mesa to the triangular contact formed onto the substrate.
17. Oxide etch before loading the sample into the evaporator.
18. Thermally evaporate 20 nm of Ti followed by 120 nm of Au.
19. Lift-off and three solvent clean.

### **A.3 Mn744 Schottky diodes**

The Mn744 structure comprised of two layers of *n*-doped GaAs on a semi-insulating substrate as shown in figure 4.5. A photolithography mask set was designed specifically for these devices.

1. Cleave samples into chips approximately 8mm × 8mm. The chips for these devices have to be larger than for some of the others as the device size is very large, on the millimetre scale. If the chip is too small you do not get many devices per chip. It is important to mark which surface is the front as they appear identical to the eye.

2. Four solvent clean and dehydrate.
3. Spin on resist and bake.
4. Pattern with mask 1 and develop. This mask allows the mesas to be formed.
5. Etch the mesas. Need to remove 700 nm.
6. Resist removal, followed by a three solvent clean and then dehydrate the sample.
7. Spin on resist and bake.
8. Pattern with mask 2 and develop. This mask allows most of the top  $n$ -doped layer to be removed from each mesa.
9. Etch to remove top layer. Need to remove 100 nm.
10. Resist removal, followed by a three solvent clean and then dehydrate the sample.
11. Spin on resist and bake.
12. Pattern with mask 3 and develop. This mask allows the ohmic contact to be formed.
13. Oxide etch before loading the sample into the evaporator.
14. Thermally evaporate 40 nm of In/Ge 50:50 by mass followed by 110 nm of Au.
15. Lift-off and three solvent clean.
16. Anneal ohmic contact at 370°C for 30 s.
17. Three solvent clean and dehydrate.
18. Spin on resist and bake.
19. Pattern with mask 4 and develop. This mask allows the deposition of an oxide layer to protect the edge of the mesa.
20. Oxide etch before loading the sample into the evaporator. It is important that the sample surface is well prepared for this evaporation as the  $\text{SiO}_x$  layer is prone to peeling.

21. Thermally evaporate  $\text{SiO}_x$ . The film thickness monitor was not well calibrated in this evaporator. The film thickness monitor gave a reading of 160 nm, but height profiler measurements showed that the deposited layer was closer to 300 nm.
22. Lift-off, three solvent clean and dehydrate. It is important to treat the sample very gently after the  $\text{SiO}_x$  has been deposited as it is prone to peeling.
23. Spin on resist and bake.
24. Pattern with mask 5 and develop. This mask allows the deposition of the Schottky diode and the associated contact pad.
25. Oxide etch before loading the sample into the evaporator.
26. Thermally evaporate 20 nm of Ti followed by 500 nm of Au. This Au layer needs to be thicker than the  $\text{SiO}_x$  layer to ensure a good electrical connection between the Schottky contact and the associated triangular contact pad.
27. Lift-off and three solvent clean.

## A.4 NU1778 superlattice devices

The NU1778 structure is shown in figure 5.4. These devices comprised of an etched mesa with top and bottom contacts. The two layers that the ohmic contacts were formed to were both  $n$ -type GaAs, so the same metal deposition could be used for both contacts. The mask set used for this was the one known as the “Robin Hood” mask, which has one etch mask and one metallisation mask.

1. Scribe and cleave the sample into chips approximately  $5 \text{ mm} \times 5 \text{ mm}$ .
2. Four solvent clean and dehydrate.
3. Spin on resist and bake.
4. Pattern with the Robin Hood etch mask and develop.

5. Etch the mesas. Need to remove 890 nm.
6. Resist removal, followed by a three solvent clean and then dehydrate the sample.
7. Spin on resist and bake.
8. Pattern with the Robin Hood contact mask and develop.
9. Oxide etch before loading the sample into the evaporator.
10. Thermally evaporate 40 nm Ge, 60 nm Au, 30 nm Ni and 100 nm Au, in that order.
11. Lift-off and three solvent clean.
12. Anneal at 360°C for 30 seconds.

## A.5 Mn775 step recovery diodes

The Mn775 structure was a *p-i-n* structure in which the intrinsic region had a graded band gap, as shown in figure 6.1. These devices comprised of an etched mesa, with a top contact and a ground contact that were formed from different metals. For this, the mask set known as the “Sheffield” mask was used. This mask set provides optical access to the top of the mesas, which was not required, but more importantly it allows the two metallisations to be different.

1. Scribe and cleave the sample into chips approximately 5 mm × 5 mm. It is important to mark the active side of the device as they both look the same.
2. Four solvent clean and dehydrate.
3. Spin on resist and bake.
4. Pattern with the Sheffield etch mask and develop.
5. Etch the mesas. Need to remove 1200 nm.

6. Resist removal, followed by a three solvent clean and then dehydrate the sample.
7. Spin on resist and bake.
8. Pattern with the Sheffield top contact mask and develop.
9. Oxide etch before loading the sample into the evaporator.
10. Thermally evaporate 20 nm Mg followed by 100 nm Au.
11. Lift-off and three solvent clean.
12. Anneal at 420°C for 30 seconds.
13. Three solvent clean and dehydrate.
14. Spin on resist and bake.
15. Pattern with the Sheffield grid contact mask and develop.
16. Oxide etch before loading the sample into the evaporator.
17. Thermally evaporate 40 nm In/Ge 50:50 by mass followed by 110 nm Au.
18. Lift-off and three solvent clean.
19. Anneal at 370°C for 30 seconds.